Microfabricated Solid Oxide Fuel Cells

THÈSE N^{O} 4175 (2008)

PRÉSENTÉE LE 26 SEPTEMBRE 2008
À LA FACULTE SCIENCES ET TECHNIQUES DE L'INGÉNIEUR
LABORATOIRE DE CÉRAMIQUE
PROGRAMME DOCTORAL EN SCIENCE ET GÉNIE DES MATÉRIAUX

ÉCOLE POLYTECHNIQUE FÉDÉRALE DE LAUSANNE

POUR L'OBTENTION DU GRADE DE DOCTEUR ÈS SCIENCES

PAR

Samuel REY-MERMET

ingénieur en science des matériaux diplômé EPF
de nationalité suisse et originaire de Val-d'Illiez (VS)

acceptée sur proposition du jury:

Dr N. Baluc, présidente du jury
Prof. P. Muralt, directeur de thèse
Prof. L. Gauckler, rapporteur
Dr P. Hoffmann, rapporteur
Dr H.-P. Loebl, rapporteur

EPFL
ÉCOLE POLYTECHNIQUE
FÉDÉRALE DE LAUSANNE

Suisse
2008

Abstract

Micro-fabricated solid oxide fuel cells (μSOFCs) are finding an increasing interest as potential power sources for portable devices such as MP3 players or laptops. The aim of this work was to fabricate a μSOFC demonstrator that works at 500°C and is fuelled by hydrogen. This thesis was divided into two parts. The first one was devoted to the development of an electrolyte and electrodes in form of sputtered thin films with electrical and mechanical properties suitable for the implementation in a real cell. YSZ and CGO electrolyte have been reactively sputtered from metallic targets. Both films are dense and have a columnar microstructure. The ionic conductivity of these films was of 0.5 S/m at 550°C for the CGO and of 5.5 x 10^{-3} S/m at 500°C for the yttria stabilized zirconia (YSZ) . Albeit the ceria doped gadolinia (CGO) was a better ionic conductor at low temperature, it was not possible to obtain an open circuit voltage (OCV) with a CGO electrolyte film. Most likely, the reduction of the Ce^{+4} ion into Ce^{+3} in a hydrogen atmosphere creates an electrical leakage. Better results were obtained with YSZ layers. Single, (111) textured columnar films showed OCV's of 200 mV. Best results were obtained with a double layer of two different microstructures. The first one exhibited a dense, columnar microstructure with (111) texture. The second layer was porous with nanocrystalline grains and preferential (200) orientation. The improved properties are ascribed to the absence of film crossing grain boundaries. Of special interest is the mechanical stress behaviour upon heating to the operation temperature. The stress was investigated as a function of temperature up to 700°C. An anomalous, hysteretic behaviour was found during the first heating cycle in YSZ as well as CGO thin films. This phenomenon could be modelled as an oxygen uptake to fill up excess oxygen vacancies created during the sputtering process. The model allowed to derive a diffusion activation energy of 0.6 eV for these excess vacancies in YSZ. Annealing in air at 700 °C permits to reduce stress and to stabilize the YSZ membrane. As electrode materials, sputter deposited, porous platinum, porous Ni-CGO composites and dense $La_xSr_{1-x}CoO_{3-y}$ (LSCO) thin films were developed and characterized. The PEN (Positive electrode-Electrolyte-Negative electrode) layer processes were combined with Micro Electro Mechanical System (MEMS) process technology to fabricate μSOFC test devices. The PEN membranes were liberated by deep silicon dry etching. The cell diameter was varied between 0.5 and 5 mm, the electrolyte thickness between 500 and 700 nm. A nickel grid grown by electroplating was used to support the electrolyte layer and to serves as current collector for the anode. The cell with a 5 mm diameter shows a very good mechanical stability up to 600°C in SOFC operating conditions and for several heating cycles. The functionality of the fuel cell with two 20 nm thick porous platinum electrodes and a YSZ bilayer electrolyte (500 nm) has been demonstrated. An OCV of 850 mV was measured at 500°C with hydrogen fuel. . Unfortunately, a too high cathode contact resistance reduced the current to very low values. The achieved maximal power density was only 19 μW/cm^2. A simple design change should remedy the problem.

Keywords: solid oxide fuel cells, thin films, YSZ, microfabrication, reactive magnetron sputtering

Résumé

Les piles à combustibles à oxyde solide rencontrent un intérêt croissant comme sources d'énergie potentielle pour les appareils électroniques portables tels que les laptops et les lecteurs MP3. Le but de ce travail fut de fabriquer un démonstrateur d'une pile à combustible à oxyde solide fonctionnant à 500°C et alimenté par de l'hydrogène. Cette thèse fut divisée en deux parties. La première fut consacrée au développement d'un électrolyte et d'électrodes sous forme de films minces pulvérisés ayant des propriétés électriques et mécaniques satisfaisantes pour être implémentées dans une vraie pile. Des électrolytes d'oxyde de zircone dopé à l'yttrium (YSZ) et d'oxyde de cérium dopé au gadolinium (CGO) ont été déposés à partir de cibles métalliques. Les deux films sont denses et présentent une microstructure colonnaire. La conduction ionique de ces films était de 0.5 S/m à 550°C pour le CGO et de 5.5 x 10^{-3} S/m à 500°C pour le YSZ. Bien que le CGO fusse un meilleur conducteur à basse température, il n'a pas permis d'obtenir de voltage à circuit ouvert. La cause la plus probable de ce dysfonctionnement est la réduction des ions Ce^{+4} en Ce^{+3} sous hydrogène qui crée un court circuit électronique. De meilleurs résultats ont été obtenus avec le YSZ. Des films simples, texturés selon la direction (111), ont permis d'atteindre un voltage de 200 mV. Les meilleurs résultats ont été obtenus grâce à des films de YSZ consistant en deux couches de morphologies différentes. La première présentait une microstructure colonnaire et était texturée selon l'orientation (111). La seconde était poreuse avec des grains nanométriques orientés préférentiellement selon (200). L'amélioration des performances de la pile est due à l'absence de joints de grains traversant l'électrolyte. Un intérêt tout particulier s'est porté sur l'évolution des contraintes mécaniques lors du chauffage jusqu'à la température de fonctionnement de la pile. Les contraintes furent mesurées en fonction de la température jusqu'à 700°C. Un comportement hystérétique anormal fut découvert lors du premier cycle de chauffe des films minces de YSZ et de CGO. Ce phénomène a pu être modélisé par une absorption d'oxygène compensant l'excès de lacunes du matériau crée lors de la déposition. Le modèle a permis de dériver une énergie d'activation de 0.6 eV pour les lacunes excédentaires d'oxygène dans le YSZ. Un recuit dans l'air à 700°C a permis de réduire les contraintes et de stabiliser la membrane de YSZ. Des films de platine poreux, d'un composite poreux de nickel et de CGO ainsi que des films denses d'oxyde de lanthane dopé au strontium et au cobalt (LSC) ont aussi été développés et caractérisés pour servir d'électrodes. Le procédé de fabrication des couches de la PEN (Positive électrode-Electrolyte-Négative électrode) a été combiné avec les technologies de microfabrication du silicium pour créer de micro-piles à combustible. Les membranes formant la PEN ont été libérées par gravure sèche profonde du silicium. Le diamètre de la membrane fut compris entre

0.5 mm et 5 mm, et son épaisseur entre 500 et 700 nm. Une grille en nickel formée par électrodéposition a été utilisée pour renforcer la membrane et a aussi servi de collecteur de courant pour l'anode. La pile ayant une membrane de 5 mm de diamètre a démontré une grande stabilité mécanique dans les conditions d'utilisation à 600°C et ce durant de nombreux cycles thermiques. La fonctionnalité d'une micro-pile comprenant deux électrodes de platine poreux de 20 nm d'épaisseur ainsi qu'un électrolyte compose d'une bicouche de YSZ de 500 nm d'épaisseur a été démontrée. Un volage à circuit ouvert de 850 mV a été mesuré à 500°C avec de l'hydrogène comme combustible. Malheureusement, une trop grande résistance interne des contacts a réduit le courant obtenu. Ainsi la densité maximale de puissance atteinte ne fut que de 19 μW/cm^2. Un simple changement de design pourra résoudre ce problème.

Mots clés: piles à combustible à oxyde solide, films minces, YSZ, microfabrication, pulvérisation réactive par magnétron

List of abbreviations

AFC	Alkaline Fuel Cell
ASR	Area Specific Resistivity [Ω/cm^2]
BSFC	$Ba_{0.5}Sr_{0.5}Co_{0.8}Fe_{0.2}O_{3-x}$
CGO	Ceria Doped Gadolinia
CVD	Chemical Vapour Deposition
DC	Direct Current
DFAFC	Direct Formic Acid Fuel Cell
DMFC	Direct Methanol Fuel Cell
EDAX	Energy Dispersive X-Ray Spectroscopy
GToe	Giga Ton of Oil Equivalent
FIB	Focus Ion Beam
IEA	International Energy Agency
Li-ion	Lithium Ion Battery
LSCO	$La_xSr_{1-x}CoO_{3-y}$
MCFC	Molten Carbonate Fuel Cell
MEMS	Micro Electro Mechanical System
NiMH	Nickel Metal Hydrides Battery
OCV	Open Circuit Voltage
PAFC	Phosphoric Acid Fuel Cell
PDMS	Polydimethylsiloxane
PEMFC or PEM	Polymer Electrolyte Membrane Fuel Cell
PEN	Positive electrode-Electrolyte-Negative electrode
PLD	Pulsed Laser Depostion
PMMA	Polymethyl Methacrylate
PVDF	Polyvinylidene Fluoride
RF	Radio Frequency (13.56 MHz)
RT	Room Temperature (25°C)
SC-SOFC	Single Chamber Solid Oxide Fuel Cell
ScSZ	Scandia Stabilized Zirconia
SDC	Samaria Doped Ceria
SEDA	Secondary Electron Diffraction Analysis
SEM	Scanning Electron Microscopy

SOFC	Solid Oxide Fuel Cell
μSOFC	Micro-fabricated Solid Oxide Fuel Cell
TEM	Transmission Electron Microscopy
TPB	Triple Phase Boundary
VRLA	Valve Regulated Lead Acid Batteries
XRD	X-Rays Diffraction
YSZ	Yttria Stabilized Zirconia
8YSZ	Yttria Stabilized Zirconia containing 8 %mol. of yttria

List of symbols

a	Lattice constant [Å]
α_x	Thermal expansion coefficient of x [ppm/K]
β	Lattice volume expansion [%]
C	Capacity [F]
c_x	Concentration of the specie x [%]
d_x	Diameter of x [m]
D	Diffusion coefficient [m^2/s]
D_0	Diffusion constant [m^2/s]
da	Lattice constant displacement [Å]
d_{gb}	Density of grain boundaries [m/m^2]
E_a	Activation energy [eV]
E_x	Electrical potential of x [V]
ε_{mem}	Emissivity of the membrane
F	Faraday constant 96485 C/mol
G	Gibbs energy [J/mol]
h_x or H_x	Heigth of element x [m]
ι	Current density [A/m^2]
η_x	Polarization due to x [Ω]
j	$j^2 = -1$
$\left\| j_x \right\|$	Flux of species x [mol/s m^2]
k	Boltzmann constant 1.38 10^{-23} J/K
K	Reaction constant
L	Length [m]
N_A	Avogadro's number 6.022 mol^{-1}
ν	Poisson ratio of x [-]
P_x	Pressure of gas x [mT] or [atm]
Q_a	Heat loss into the air by convection
Q_e	Heat loss due to radiation
Q_h	Heat loss by conduction
Q_r	Reactive gas flow
r_x	Radius of curvature of x [m]

r_1	Radius of curvature before film deposition [m]
r_2	Radius of curvature after film deposition [m]
R	Molar gas constant 8.3144 J/molK
R_4	Four points resistance [Ω]
R_p	Parallel resistance [Ω]
R_s	Serial resistance [Ω]
ρ_0	Density [kg/m^3]
S_x	Stress of the element x [MPa]
σ	Ionic conductivity [S/m]
σ_b	Stephan Boltzmann constant 5.67x10-8 W/m2K4
T	Temperature [K]
T_0	Temperature in the center of the membrane [°C] or [K]
T_b	Temperature at the border of the membrane [°C] or [K]
T_{final}	Final temperature [°C] or [K]
$T_{initial}$	Initial temperature [°C] or [K]
ΔT	Temperature change [°C] or [K]
ΔT_{crit}	Critical temperature change for buckling or cracking [°C] or [K]
t_x	Thickness of x [m]
τ_x	Rate of deposition of film x [nm/min]
$tan\delta$	Capacitive losses [%]
V	Voltage [V]
w	Width [m]
ω	Pulsation [Hz]
ω_{rot}	Rotation speed [Hz]
Y	Complex admittance [S]
Y_x	Young modulus of x [MPa]
Z	Complex impedance [Ω]
z	Number of charges

Special notations:

$\overline{X}$	Mean value of variable X
ΔX	Variation of variable X
$Y(X)$	Y is function of variable X

Table of contents

2. STATE OF THE ART OF μSOFCS 35

3. THIN FILM DEPOSITION AND CHARACTERIZATION 51

4. μSOFC FABRICATION AND CHARACTERIZATION 105

Introduction

1.1. Motivation for this thesis

1.2. Generalities on fuel cells

1.3. Solid Oxide Fuel Cells

1.3.1. Principle of work

1.3.2. SOFC components

1.3.3. SOFC designs

1.4. Materials requirements for SOFCs

1.4.1. The electrolyte

1.4.2. The cathode

1.4.3. The anode

1.4.4. Polarization

1.5. Batteries for portable applications

1.5.1. Important parameters for the description of batteries and fuel cells

1.5.2. Li-ion batteries

1.5.3. Zinc-air batteries

1.5.4. Nickel cadmium batteries

1.5.5. Nickel-metal hydride batteries

1.5.6. Zinc-carbon batteries

1.5.7. Lead acid batteries

1.5.8. Alkaline-manganese dioxide batteries

1.6. Micro fuel cells (µSOFCs)

1.6.1. From fuel cells to micro solid oxide fuel cells

1.6.2. Existing micro fuel cells
1.6.2.1. Micro polymer electrolyte membrane fuel cells
1.6.2.2. Micro direct methanol fuel cells
1.6.2.3. Micro direct formic acid fuel cells
1.6.2.4. Micro solid oxide fuel cells

1.7. Aim of this work

1.8. Outline

1.9. References

1.1. Motivation for this thesis

In 2004, the primary worldwide energy consumption was about 11.7 Gtoe (gigaton of oil equivalent) [1]. Eigthy-two percent of this energy has produced CO_2 emissions by means of fossil fuel combustion. This is the equivalent of 7 GTon of carbon. Keeping the emissions at this level for the next 50 years will permit to stabilize the CO_2 concentration at 500 ppm, less than the double of the pre-industrial concentration (280 ppm), but more than its actual value (375 ppm). Such an effort is extremely important to keep the earth's living conditions acceptable [2].

Since 1985, the balance between the annual world reserves additions of petroleum and the annual consumption becomes negative [3] (Figure 1). This means that since then we are discovering less petroleum than we are consuming, and this difference increases year after year.

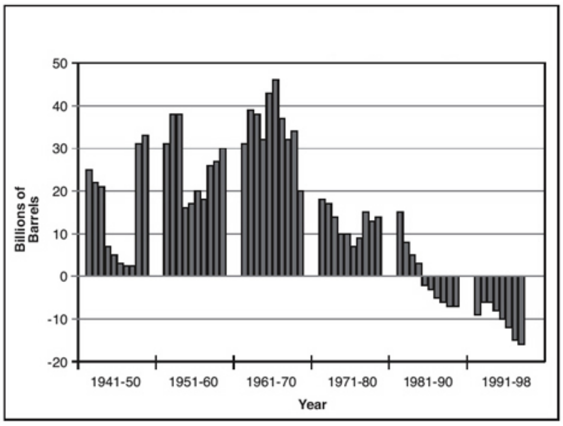

Figure 1: Balance of the petroleum annual world reserves additions minus the consumption over the years, from [3].

This still growing consumption of petroleum has two major impacts: the price of oil and the amount of greenhouse gases released in the atmosphere increase continuously. The price of oil could be a more critical parameter for the end of the oil era than the depletion of the actual petroleum reserves. New green technologies such as solar cells and windmills could substitute petroleum in electrical power production.

The problem of substituting petroleum in mobile applications remains. One simple way to reduce energy consumption is not to waste it. The fuel cells have better efficiency than engines and generators (Figure 2). Moreover, there are viable scenarios for a society with hydrogen as portable energy produced by renewable sources, such as hydroelectric, geothermal, solar, wind and biomass or even nuclear power plants [4]. The abundance of oil lead to a negligence of the research on alternative energy topics during the 20th century. Solid oxide fuel cell (SOFC) technologies exist as prototypes, but predictions show that fuel cells will dominate the transportation market only after 2030-2040 [5]. The reasons for this delay are difficulties related to the storage and distribution of hydrogen [6], the high costs and the technological immaturity of fuel cells [7]. Nevertheless, it is urgent to implement fuel cells and hydrogen as vector for energy. Engines fuelled by hydrogen have the advantage of being non pollutant as they mostly reject water vapour [8]. Cars using this technology already exist and show sufficient performances [9]. Fuel cells can also be used for co-generation of heat and electricity to supply buildings or industries [10] or even in portable applications [11]. This thesis has been motivated by the question whether SOFCs can be scaled down for use in portable devices and fabricated in MEMS technology. The high energy density and large autonomy of miniature or micro SOFC cells makes these portable power sources ideal for hand held equipment such as digital cameras. Micro SOFCs (μSOFC) would require an easy to handle and secure fuel. Currently we can consider lighters based on butane as an already existing product based on small volume fuel reservoirs. This means that micro-SOFCs would not suffer from a fuel distribution problem. If in later years hydrogen society became reality, hydrogen would of course be an even more environmentally fuel.

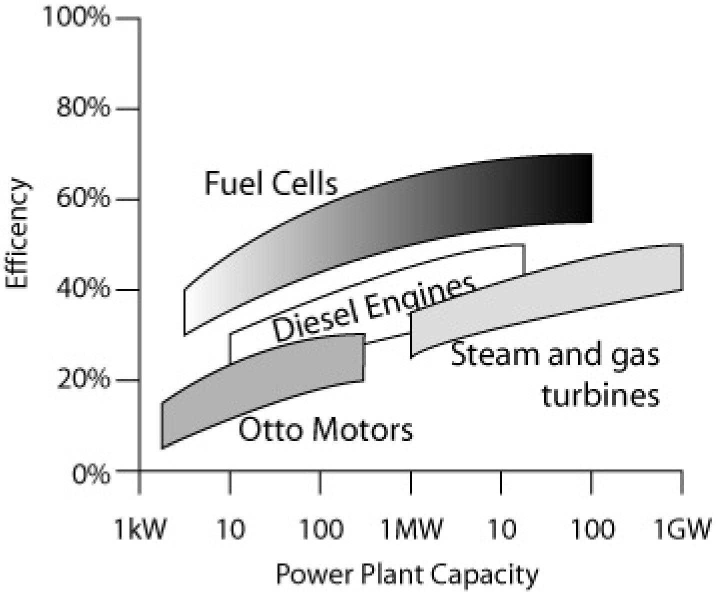

Figure 2: Efficiency and capacity of different types of electrical power plant, from [8]

1.2. Generalities on fuel cells

This introduction will give an overview on fuel cells, presents their working principles and compares with alternative portable power sources. At the end of the chapter, the goals of this thesis will be formulated.

A fuel cell is a device that converts chemical energy directly into electrical energy. Since the discovery of the principle of the fuel cell by W. Groove in 1829 [12], this power source didn't get the enthusiasm it was supposed to. This is mainly due to the discovery of electromagnetic induction (i.e. basic principle of electrical power generators transforming mechanical power) in 1839 by M. Faraday

[13] and to development of combustion motors (Otto and Diesel). Although engines are less efficient [14] (Figure 2) and more pollutant than fuel cells, they were advantaged by a lower cost and a simpler technology. Fuel cells were only developed for some specific applications requiring high efficiency such as space modules [13]. Today, with the still increasing interest on the environmental aspects, fuel cells are probably the best solution for clean power generators as Ostwald pointed it out already in 1894 [15].
The chemical reaction that drives fuel cells is divided into two parts:

- At the anode, the oxidation of a fuel such as hydrogen, carbon monoxide or even hydrocarbons.
- At the cathode, the reduction of oxygen or carbon dioxide.

As well as two electrodes, the fuel cell also consists of an electrolyte that is permeable to a given type of ions (H^+, O^{2-}, CO_3^{2-} or OH^-). Ions are chemically formed at one electrode and then diffuse to the other through the electrolyte. This internal ionic flux is balanced by an external electrical current in the load. The nature of the electrolyte and the diffusion of ions through it are a critical aspect of these devices. The choice of electrolyte influences the power, the materials requirements, the temperature of operation, the fuel and even the geometry of the cell. Fuel cells are classified by their type of electrolyte. It can be a liquid, a polymer or even a ceramic. Low temperature fuel cells have the advantage of smaller requirements on materials properties such as resistance to corrosion and thermal dilatation. Within fuel cells operating over 600°C, internal gas reforming is possible. It permits the use of hydrocarbon fuels like methane or propane that is transformed (reformed) into hydrogen within the cell. High temperature cells also take the advantage of transforming the exhausted heat into energy and thus reach a better overall efficiency.

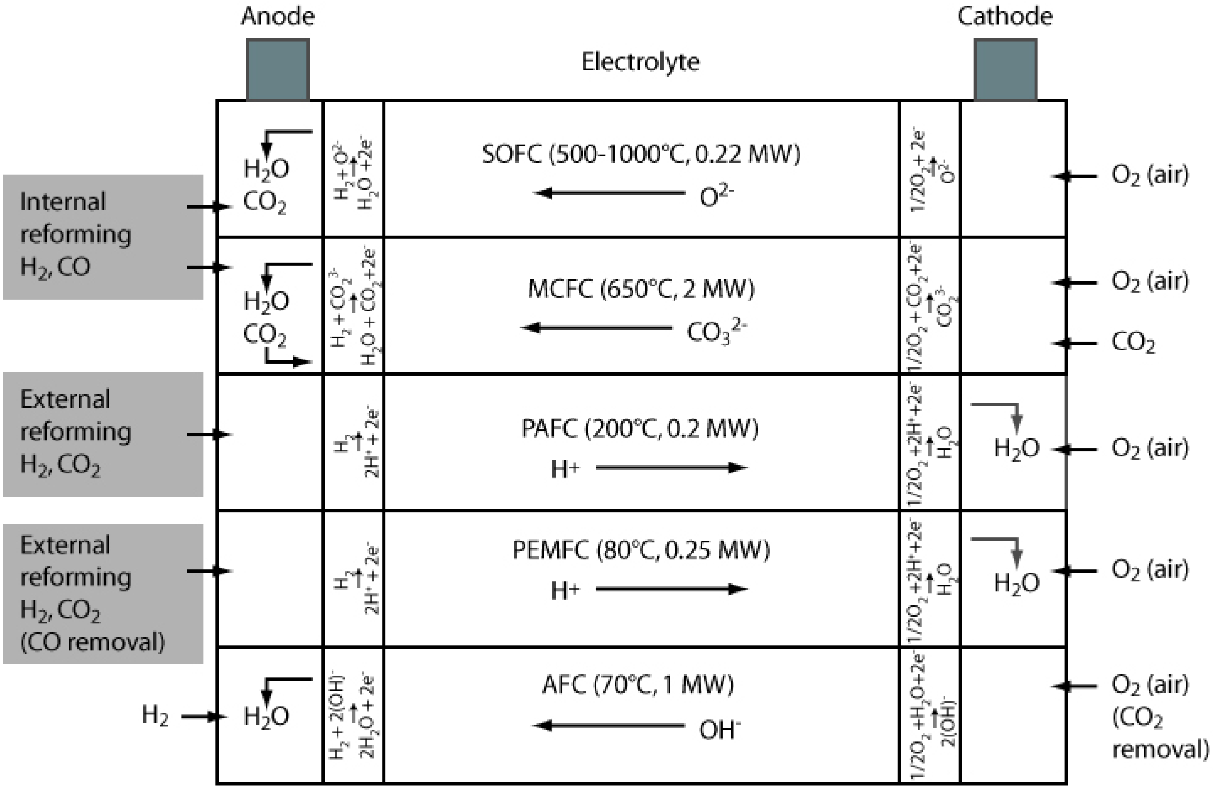

Figure 3: Different types of fuel cell with typical reactions and operation parameters, from [16].

Different types of fuel cells have been developed (Figure 3). Alkaline fuel cells (AFCs) were used in the Apollo missions and have a low temperature of operation (70°C). The electrolyte is a concentrated solution of potassium hydroxide. The major disadvantage of AFCs is that the alkaline solution doesn’t reject carbon dioxide and thus they are limited to pure O_2 (air with CO_2 removal) and H_2. Polymer electrolyte membrane fuel cells (PEMFCs) use a polymer membrane such as fluorinated sulfonic acid polymer as electrolyte. They conduct protons and work at temperatures below 100°C. The only liquid in the cell is water, thus corrosion problems and materials requirements are limited. Water management in the membrane is critical for efficiency. The water should not evaporate faster than it is produced by the cell in order to keep the membrane hydrated. The low operating temperature limits the fuel range to pure hydrogen and internal reforming is not possible. In Phosphoric Acid Fuel Cells (PAFCs), protons diffuse in a concentrated phosphoric acid solution constrained in a polymer [17]. PAFCs have the same requirements on fuel purity as PEMFCs. The temperature of operation of PAFCs is comprised between 160°C and 220°C. This higher temperature makes the waste heat more valuable. PAFCs can use external reforming and are still the most used type of fuel cells for commercial applications with a power of 200 kW. In Molten Carbonate Fuel Cells (MCFCs) CO_3^{2-} ions diffuse in a liquid Li/Na/KCO_3 electrolyte. MCFCs operate at 650°C thus they can use a wider range of fuels thanks to internal reforming. Furthermore they reach a higher efficiency by using of the waste heat and can deliver 2 MW of power. On the other hand, the high temperature imposes severe constraints on the choices of materials. Solid Oxide Fuel Cells (SOFCs) utilize a true solid electrolyte made of ceramic (mostly yttria stabilized zirconia YSZ). As the diffusion of O^{2-} ions in solids is slower, SOFCs operate only at high temperature (1000°C). A great scientific effort is ongoing to lower the temperature of SOFC to around 500°C [18]. Micro SOFCs (µSOFCs) can even operate at 400°C with hydrogen as fuel [19]. SOFCs operating at high temperatures can use either CO or H_2 and internal reforming is feasible. The thermal strain is a great disadvantage for SOFCs and can even break stacks. The deposition of carbon on the nickel anode can also lower the efficiency of the SOFCs.

1.3. Solid Oxide Fuel Cells

1.3.1. Principle of work

As schematically shown in Figure 4, a SOFC is composed of three active layers: a cathode, an electrolyte and an anode. This stack is often referred as PEN for “Positive electrode-Electrolyte-Negative electrode”. The fuel can be hydrogen or carbon monoxide. The high temperature of operation also permits to reform hydrocarbon gas within the cell.

The PEN is basically a membrane separating two different gas atmospheres, in the specific case two different oxygen partial pressures. At the cathode side exposed to air, electrons dissociate and reduce adsorbed oxygen, thus forming oxygen anions. These ions diffuse through the electrolyte and oxidize the fuel (hydrogen or carbon monoxide) at the anode side to form steam or carbon dioxide and electrons. The electrons are released at a negative, thus higher electronic potential, into the external circuit. This provides the electro-motoric force for driving an external user device. The continuous oxidation of the fuel maintains a very low oxygen partial pressure at the anode, and thus maintains the difference in electrochemical potential also during current flow.

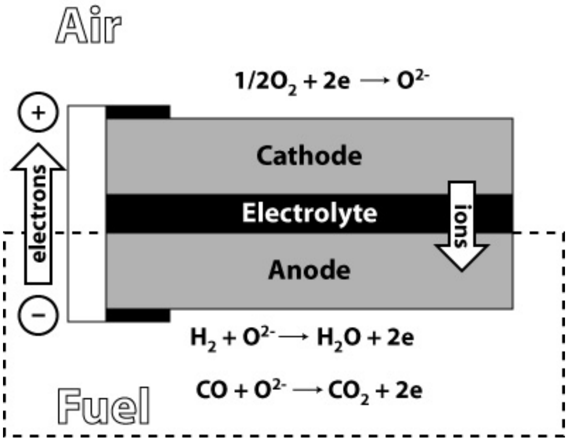

Figure 4: Schematic view and principle of operation of a SOFC

The summary chemical reactions involved in a SOFC are the following:

- At the cathode, the formation of oxygen anion by reduction of the oxygen gas:

$$\frac{1}{2} O_2 + 2e^- \rightarrow O^{2-} \tag{1.1}$$

- At the anode, the oxidation of the fuel:

$$H_2 + O^{2-} \rightarrow H_2O + 2e^- \tag{1.2}$$

$$CO + O^{2-} \rightarrow CO_2 + 2e^- \tag{1.3}$$

The complete cell reactions are:

$$\frac{1}{2} O_2 + H_2 \rightarrow H_2O \tag{1.4}$$

$$\frac{1}{2} O_2 + CO \rightarrow CO_2 \tag{1.5}$$

The Gibbs free energy change ΔG per mole of reactions (1.4) and (1.5) can be directly transformed into electric energy by the SOFC.

$$\Delta G = zF \cdot E \tag{1.6}$$

where F (96485 C) is the Faraday constant, E the cell voltage and z the number of charges involved in the reaction.

The open circuit voltage (OCV) of a cell can be related to the constant of reaction K and thus to the oxygen pressure at the cathode $p_c(O_2)$ and at the anode $p_a(O_2)$.

$$E_{OCV} = \frac{RT}{nF} \ln \frac{p_c(O_2)}{p_a(O_2)} \tag{1.7}$$

where R is the gas constant.

OCV is due to the oxygen pressure difference between the cathode and the anode, whereby thermodynamic equilibrium is assumed on the anode side.

1.3.2. SOFC components

The SOFC is not only composed of the PEN but also of several other parts [8] as shown in Fig. 5. The purpose of the different cell’s parts and the interactions between them are described hereafter.

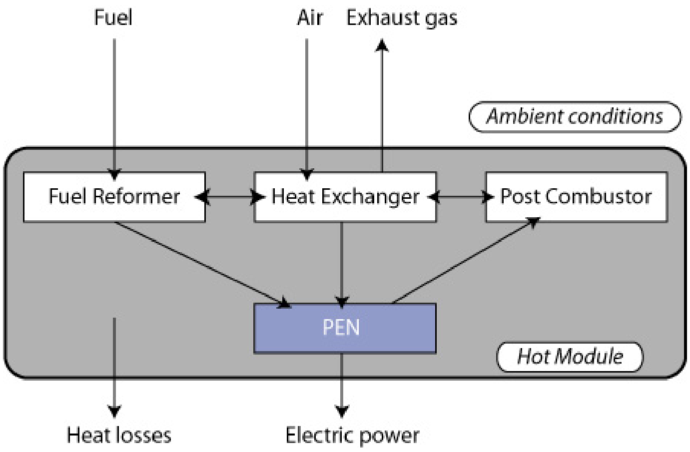

Figure 5: Summary of the different component of an SOFC power plant

As the SOFC operates at high temperatures (500-1000°C) it should be thermally isolated from the environement. For security and efficiency reasons, it is important to minimize thermal losses into the environment. Very helpful are heat exchangers that heat up incoming gases by means of the hot oxidized gases leaving the SOFC. A large part of the output gas consists of hot steam. In very well designed generators, part of the output heat can even be converted into electrical energy. This phenomenon is called co-generation and can improve the efficiency of the cell by some percents. The fuel is stored in a tank at room temperature i.e. outside of the hot module. The air is provided directly from the atmosphere, and is thus cold too. If the needed hydrocarbon fuels are treated with hot steam in the reformer to form CO and H_2 as:

$$CH_4 + H_2O \rightarrow CO + 3H_2 \tag{1.8}$$

the thermal energy of the hot steam is used to drive at least partially this endothermic reaction (-49 kcal/mol) [20]. The maximal forming efficiency is obtained at 550°C. A further improvement of the overall energy efficiency is obtained when the exhaust heat is used for heating purposes, usually by heating water in a heat exchanger. This thermal energy output can be used to heat a building for example, and increases the efficiency of the SOFC up to 80%. A further heat source is due to non-reacted fuel gases. These are burned in a post combustor. This one must also be included into the energy recuperation scheme, and is especially suited to deliver the initial heat to ramp up temperature to the operation level. Finally, also a rather intelligent regulation circuit is necessary to adjust heat and fuel flow to the electrical power consumption by the external users. Since this adjustment is not very fast, buffer batteries are needed to store and deliver electrical energy on short terms.

1.3.3. SOFC designs

The design of a single cell is closely related to the design of the whole stack. Because a single cell only delivers 1V, several cells are often connected in series to reach higher voltage [20]. The most common stacks have tubular, planar or single chamber designs [21].

Experimental SOFCs with tubular design were invented in the 1960s to facilitate gas sealing that was complicated by thermal expansion mismatch between the different parts of the cell. Figure 6 shows the tubular design was mainly developed and improved by Siemens-Westinghouse over the last 20 years [22]. The air flows in the center of the cell within the cathode pipe. The fuel flows in the same direction outside of the tube along the anode. The electrolyte is sandwiched between the inner cathode pipe and the outer anode pipe.

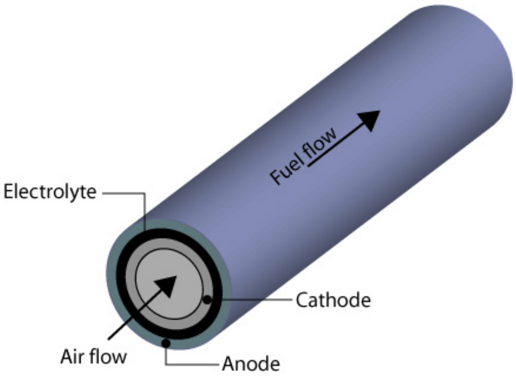

Figure 6: Siemens-Westinghouse tubular design for SOFC

At the end of the tubes, the remaining gases recombine to produce heat. The drawback is that the electrical current is collected along the tube at the anode and at the cathode. It increases the length of the conducting path and the ohmic resistance. Existing tubular cells have relatively low power density (100 to 200 mV/cm^2 [21]), compared to other systems.

Planar SOFCs are composed of plates with distinctive functions (anode, electrolyte, cathode and interconnect) that are piled up. The gas feeding system is included within the interconnectors. The whole stack can be supported either by the anode or by the electrolyte. Anode supported systems can reach a power density of almost 2 W/cm^2, while electrolyte supported systems are limited by the high resistance of the 100-200 μm thick YSZ ceramic plate. Their surface is also limited to an area of 10x10 cm^2 [21]. One of the best known electrolyte supported planar SOFC is the Sulzer Hexis system (Figure 7) that provides 1.1 kW at 950°C and composed of 70 cells stacked together [23].

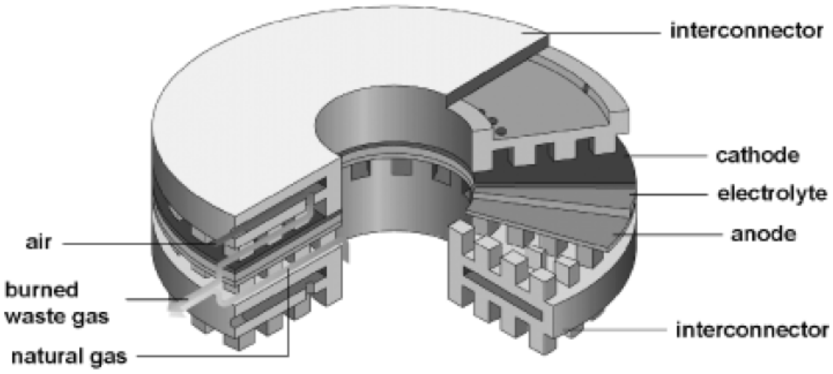

Figure 7: Sulzer-Hexis planar design for SOFC

To thin the electrolyte and to support it by the anode is a good method to reduce the operating temperature of the cell. Some special alloys of chromium and ferrite can support corrosion at 850°C and can be used as interconnectors. Their good thermal conductivity reduces the temperature gradient across the stack and allows increasing its size.

Another design option is single chamber SOFCs (SC-SOFCs) [24]. Both anode and cathode are placed in the same gas mixture of oxidant and reducing species. The electrodes can be deposited on the same side of the electrolyte with an interdigited pattern or on both side of it (Figure 8) and some SC-SOFCs are also anode supported. No complex gas flow structures are needed and the sealing is simplified. The reaction requires high selectivity of the electrode according to the different gases and this phenomena isn't well understood for the moment. Hibino and co-wokers have been working on SC-SOFCs for more than ten years. In 2000, they reached a power density of 350 mW/cm^2 at 700°C with $La_{0.9}Sr_{0.1}Ga_{0.8}Mg_{0.2}O_3$ as electrolyte [25].

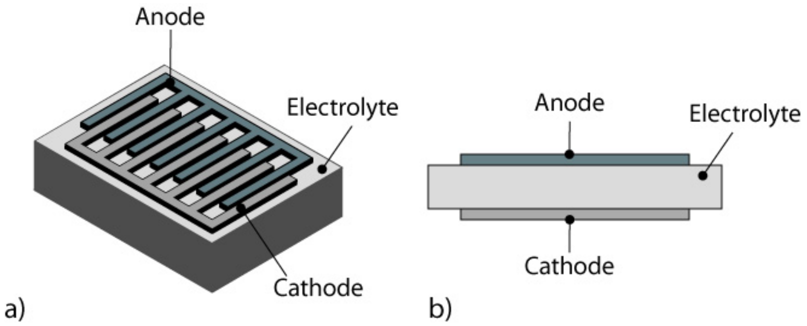

Figure 8: Single chamber SOFCs with interdigited electrodes on the same side of the electrolyte or with electrolyte sandwiched between anode and cathode.

When both electrodes are mounted on the same side of the electrolyte substrate, SC-SOFCs have the advantage of being very robust since they are not freestanding. The critical length for this type of SC-SOFCs is the gap between the anode and the cathode. It can be narrowed to 100 μm by use direct writing through micro-nozzles [26] and even to 10 μm by of screen printing [27] for a maximal power density of 17 mW/cm^2.

1.4. Materials requirements for SOFCs

1.4.1. The electrolyte

Electrolytes should conduct oxygen ions and be insulating to electrons. Figure 9 summarizes the different choices for the electrolyte materials, by taking a typical value 0.15 Ω/cm^2 [16] for the maximal area specific resistivity (ASR).

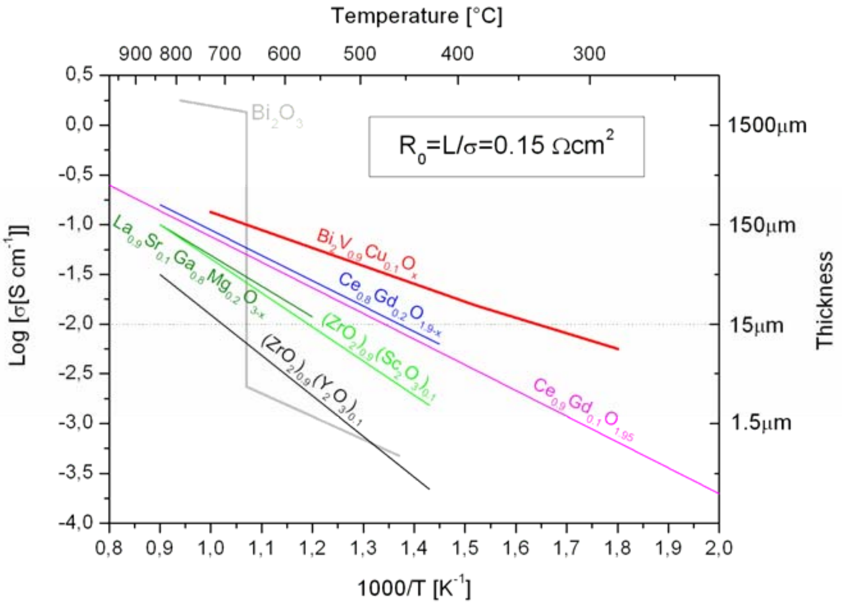

Figure 9: Conductivity of different electrolyte materials with temperature from [16] and [20]

When using weak ionic conductors and at low temperatures, electrolytes should be thinned down to keep the ASR below this critical value. Electrolytes that are thinner than 150 μm are subject to cracking if they are not supported [28], for example by a thick and porous anode [29]. Thicker electrolytes can be self-supported but often require higher temperature.

Electrolytes should be dense and gas tight to prevent gas mixing across the PEN. They should be stable with temperature and chemically inert towards the anode and the cathode. Thin and columnar microstructures can be a problem if grain boundaries or pinholes are electronically conductive.

Electrolytes are made of ionic conductor with a fluorite type structure, such as yttria stabilized zirconia (YSZ) or gadolinia doped ceria (CGO). In theses materials oxygen vacancies are created by the substitution in the lattice of ions of lower valency than the predominant cations. Here are shown the defects reactions of YSZ and CGO:

$$Y_2O_3 \xrightarrow{ZrO_2} Y_{Zr}^{'} + \tfrac{1}{2}V_O^{\cdot\cdot} + Zr_{Zr} \quad (1.9)$$

$$Gd_2O_3 \xrightarrow{CeO_2} Gd_{Ce}^{'} + \tfrac{1}{2}V_O^{\cdot\cdot} + Ce_{Ce} \quad (1.10)$$

CGO shows a better ionic conduction than YSZ but is electronically conductive at low oxygen pressure [30]. Some other candidates for electrolytes are bismuth oxides [31] and lanthanum strontium gallium manganite [32].

1.4.2. The cathode

The electrodes should conduct electrons and ions, be permeable to gases, favor the adsorption of oxygen atoms, be chemically stable to the electrolyte and be thermally compatible with it. Porous ceramics and cermets are good candidates for electrodes.

At the cathode, the presence of oxygen restricts the use of metals even in the form of cermets. The triple phase boundary (TPB) is the line between the gas, the ionic conductor and the electronic conductor. At TPB, all the species required in the chemical reaction are available. It has been shown by finite element modeling, that the width of the TPB (or the zone where the reaction is possible) affects the ASR and thus the cell power [33].

With a pure electronic conductor as cathode, the reaction can only occur at TPB, because metals don't conduct ions nor do electrolytes conduct electrons. In this case, porosity should be sufficient through the cathode to bring oxygen molecules in contact with the electrolyte. The quite low activity of metal cathodes and their low resistance to oxidation make them bad cathodes for high temperatures (800-1000°C). But pure and noble metals like platinum [34], silver and gold [35] can exhibit higher ASR at low temperatures (below 600°C) than mixed conductors because these ones are limited by their ionic conductivity. Nevertheless most of the literature deals with ceramic, mixed conducting cathodes [36]. In this case, there are more possible reaction routes than in purely metallic electrodes [30] and the reduction of oxygen occurs not only at TPB (or the TPB can be considered as wider). For example, when the cathode is a mixture of an ionic conducting phase and of an electronic conducting one, oxygen molecules can be reduced at the boundary between the two phases, if the porosity is sufficient. In this case, the reaction also occurs at the frontier between the ion conducting phase and the electronic one, even if this zone is far from the electrolyte. If the cathode is a mixed conductor, the reaction can occur all over the grains, if they are in contact with air. Perovskite mixed conductors such as doped lanthanum oxides, [37] or as praseodymium barium cobalt oxides [38] are often used as cathodes. In all the cases, the effect of the microstructure and of the composition of the cathode is very important for the efficiency of the SOFC.

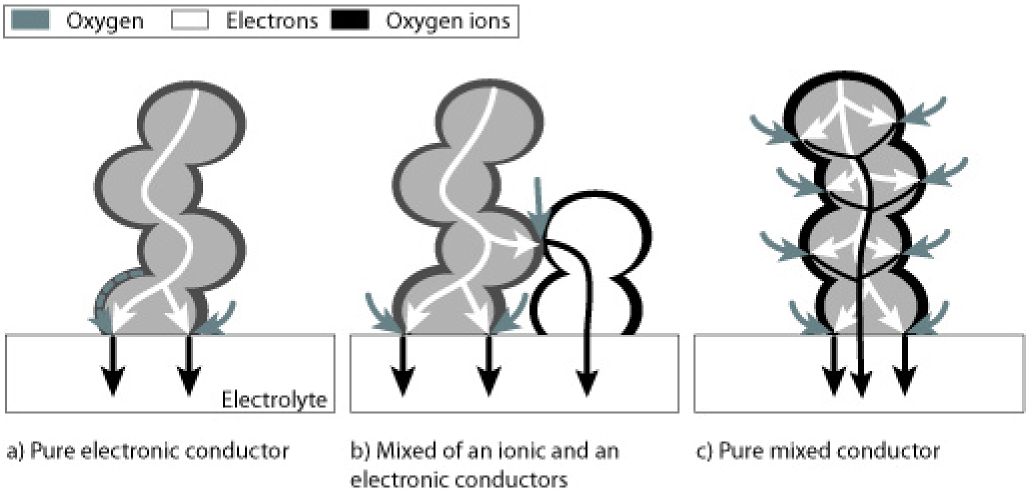

Figure 10: Reaction routes for reduction of oxygen in a pure electronic conductor (a), in a composite of a electronic and an ionic conductor (b) and in a single-phased mixed conductor

For thin electrolytes (<100 μm), the electrolyte conductance deviates from the linear law 1/thickness and also becomes dependent on the electrode microstructure dimensions (grain size and space between them) [33].

1.4.3. The anode

Like the cathode, the anode should conduct ions and electrons and be permeable to gas. Since the anode is exposed to the fuel, there is no risk of oxidation, thus the use of metals such as nickel [39], platinum [40] and ruthenium [41] or cermets is more common [41, 42]. Nickel and YSZ based cermets are still the most common anodes in SOFCs [42] but mixed conducting materials such as CGO are also studied [43]. Nevertheless, in case of PEN stack breaking, the anode can be exposed to oxygen at high temperatures and the resulting oxidation would be a killing factor for the whole cell. The TPB has the same role as on the cathode side, and the diffusion routes of the different species in ceramic-metal cermet are the same as for the cathode.

The catalytic activity of the anode is very important, as the oxidation of hydrogen molecules begins with a chemisorption and dissociations at the surface of the anode [43].

The anode serves as mechanical support in most of the SOFC designs. In this case, the porosity should be sufficient in the anode because its thickness should be more over 100 μm. Most of the supporting anodes are made of NiO or YSZ cermets [29, 44], but the cell can also be supported by a metallic substrate, for example by a nickel porous plate [45].

1.4.4. Polarization

In steady-state conditions, SOFC voltage E_{OCV} follows the laws of thermodynamics and is given by the Nernst equation (1.7). E_{OCV} only depends on the difference of oxygen pressure between the cathode and the anode. Steady-state means that no electrical current is established in the load or even within the cell. Obviously thermodynamics can only describe a situation that is far away from the operating conditions of the SOFC. When a current is drawn out of the cell, or even if some small currents take place within the PEN, its behavior should be described by kinetic relations.

Usually, the establishment of a current density i in or out of the cell implies a voltage drop in the PEN. This drop is called the polarization η and is the difference between E_{OCV} and the voltage measured in series with the cell V. Therefore η is measured in Volts.

$$E_{OCV} = V(i) + \eta(i) \tag{1.11}$$

The polarization η and the measured voltage V are functions of the current density i. If the gas conditions are stable, the voltage at OCV doesn't depend on i and follows the Nernst equation.

The polarization η may have several origins:

1) Ohmic polarization η_{ohm}
2) Concentration polarization η_{conc}
3) Activation polarization η_{act}

The ohmic polarization is due to the transfer of ions or electrons in bulk materials (the electrodes or the electrolyte). η_{ohm} simply follows Ohm's law and is characterized by the lengths l_i and the resistivities ρ_i of the different materials. The index i can be replaced by a for the anode, c for the cathode and e for the electrolyte. With this formalism, η_{ohm} is just the sum of all the PEN elements contributions and the resistance of the contact R_{cont}.

$$\eta_{ohm} = (\rho_e l_e + \rho_a l_a + \rho_c l_c + R_{cont})i \tag{1.12}$$

The concentration polarization η_{conc} is due to the mass balance at reaction points. For example, at the anode the oxidation of hydrogen (equ. (1.2)) involves several fluxes (in number of atoms of molecules per second and per surface):

1) The flux of hydrogen gas $|j_{H2}|$
2) The flux of oxygen $|j_{O2}|$
3) The flux of exhausted water steam $|j_{H2O}|$

4) The flux of electrons or current density *i*.

In the case of the reaction (1.2), the balance of the fluxes implies:

$$\left| j_{H_2} \right| = \left| j_{H_2O} \right| = 2\left| j_{O_2} \right| = \frac{iN_A}{2F} \qquad (1.13)$$

with Avogadro's number N_A (6.022 x 10^{-23} mol^{-1}) and the Faraday constant F (9.649 x 10^4 C/mol)

The activation polarization η_{act} is due to the activation energy needed for chemical reactions occurring during SOFCs operation. For example, the dissociation of an oxygen molecule adsorbed on a metallic cathode into an oxygen atom requires a given activation energy:

$$\frac{1}{2} O_{2,ads}(metal) \rightarrow O_{ads}(metal) \qquad (1.14)$$

This can delay the process and therefore limit the rate of the reaction and the current of the cell. During SOFC operation, the chain of reactions involved in the process is not clear and may vary with materials and operating conditions [46-50]. If possible, the limiting step should be elucidated in order to understand the cell behavior better.

In all the cases, polarization depends on many different parameters such as materials, microstructure, gas pressure, temperature and also on the current density.

1.5. Batteries for portable applications

For the sake of comparison with fuel cells, the existing portable batteries will be briefly described and discussed in this chapter. In figure 1, the performances such as specific energy and energy density are reported and compared to micro fuel cells.

In contrary to fuel cells, the batteries are not relying on the availability of an external fuel. In other words, they do not stop in case of lack of fuel but when the reactants are transformed. As they are sealed, it is also impossible to replenish reactants. Nevertheless, most of the batteries can be recharged as fuel cells can be refuelled. The batteries rechargeable by an electrical current are called secondary batteries and batteries that are not chargeable are referred to as primary batteries. The applied voltage during charge reverses the cell reaction. This mechanism is time-dependent. In contrast, the fuel cells can be refuelled immediately just by filling their tank. Another disadvantage of secondary batteries compared to fuel cells is that they are subject to gassing if overcharged. The phenomena can lead to explosion even if it is well controlled by battery manufacturers. Nevertheless, the market of portable electronics is still dominated by batteries (especially Li-ion) and micro fuel cells are still under development.

Before the description of most of the existing types of portable batteries, we introduce important parameters for the description of batteries and fuel cells such as the energy density and the specific energy.

1.5.1. Important parameters for the description of batteries and fuel cells

As explained in chapter 1, the cell standard potential *E°* is proportional to the change of the system free energy ΔG occurring during the cell reaction (equation 1.1). The *ΔG*'s and *E°*'s of the different basic chemical reactions are listed in handbooks. They can be summed up to find the *ΔG* and *E°* of a more complex reaction. For example:

$$\begin{array}{l} Zn \rightarrow Zn^{2+} + 2e........-(-0.76V) \\ Cl_2 \rightarrow 2Cl^- - 2e............1.36V \\ \hline Zn + Cl_2 \rightarrow ZnCl_2, E° = 2.12V \end{array} \tag{1.15}$$

The theoretical coulombic capacity depends on the amount of active material in the cell. The electrical equivalence in Ah/g or g/Ah are listed in tables such as in Handbook of batteries [51]. By summing up the electrical equivalence of all the active elements involved in a reaction, it is possible to determine the theoretical capacity of a given battery. With the electrical equivalences of Zn (1.22 g/Ah) and of Cl_2 (1.32g/Ah), the theoretical capacity of the previous cell reaction (1.15) can be calculated:

$$1.22 g/Ah + 1.32 g/Ah = 2.54 \text{ g/Ah} \tag{1.16}$$

This theoretical capacity only takes the active anode and cathode materials into account.

The theoretical energy of a battery can be calculated by multiplying the standard potential times the theoretical electrical capacity:

$$Watthour(Wh) = voltage(V) \times ampere - hour(Ah) \tag{1.17}$$

The specific energy (in Wh/g or Wh/kg) can be calculated by dividing the theoretical energy of a cell by its weight. The ratio of the energy divided by the cell volume is called energy density. The energy density has units of watthour per liter (Wh/L).

It is important to notice that the specific energy and the energy density are theoretical values based only on the active materials involved in the cell. Actually the battery is also composed of non-active materials other than the electrolyte and the electrodes. These materials forming the current collectors, the separators or the packaging (sealing, container terminals) are not included into the calculation and their weight and volume reduce the theoretical energy density by almost 50%. Another deduction should be done because in most of the cases it is impossible to totally discharge a battery. Finally, the actual energy density of a battery is only about 25 to 35% of the theoretical value. Nevertheless, the theoretical value is a very good and simple tool for batteries comparison.

1.5.2. Li-ion batteries

Lithium ions batteries are the most widespread power sources in portable electronics. In 2006, 2.5 billion Li-ions cells were sold in the world. They reach a high specific energy of approximately 150 Wh/kg and an energy density of 400 Wh/L, which makes them very competitive for small and light applications. Lithium ions move from the anode to the cathode during the discharge and in the opposite way during the charge. The anode is made of carbon, the cathode is a metal oxide (e.g. CoO_2), and the electrolyte is a lithium salt (e.g. $LiPF_6$) in an organic solvent. The full reaction of a conventional Li-ion battery is [51]:

$$Li_{1-x}MO_2 + Li_xC_n \underset{CHARGE}{\overset{DISCHARGE}{\rightleftarrows}} LiMO_2 + C_n \tag{1.18}$$

Li-ion batteries are often referred to as rocking-chair batteries as lithium ions “rock” from on electrode to the other during charge and discharge. A Li-ion single cell can operate in the range of 2.5 to 4.2V, approximately three times more than NiCd or NiMH batteries. The polymer electrodes degrade when the cell is discharged below 2 V and need a protective circuit since they cannot avoid overcharging.

1.5.3. Zinc-air batteries

Zinc air batteries were first available as primary button type batteries and commercialized in the 1930’s. These buttons have a very high specific energy of 442 Wh/kg and an energy density of 970 Wh/L with a voltage of 0.9 V. They offer the highest available energy density for primary cells and can be used in very small applications such as hearings aids. They are nevertheless limited by their power output and by their short active life [51]. The porous thin cathode should be permeable to oxygen as well as hydrophobic and is thus often coated by Teflon [52]. The cathode catalyses the formation of hydroxide ions by combination of oxygen and water. The anode is simply made of zinc and is oxidised into Zn^{2+} ions. The overall reaction of this kind of battery is given below:

$$Zn + \frac{1}{2}O_2 \rightarrow ZnO \tag{1.19}$$

Zinc air secondary batteries (i.e. capable of recharging) were developed later and the charge remains a problem because of the replating of zinc. The zinc-air secondary batteries provide electrical energy from the oxidation of zinc from oxygen in the air. Their overall reaction is the same as zinc air button cells (cf. equation (1.19)). This type of battery is already used in mobile phones and has a typical energy density of 1000 Wh/L and a specific energy of 400 Wh/kg [51]. Zinc-air batteries also exist in form of a fuel cell where zinc is replenished and zinc oxide waste is removed continuously [53].

1.5.4. Nickel cadmium batteries

Portable sealed nickel cadmium batteries are designed to prevent gassing during overcharge and do not require any other services than recharging. This type of nickel cadmium battery is comparable to other portable power sources discussed in this chapter. The negative electrode is made of cadmium hydroxide ($Cd(OH)_2$), the electrolyte of a solution of potassium hydroxide and the positive electrode of nickel oxyhydroxide (NiOOH). During the discharge, the cadmium electrode is oxidized ($Cd + 2OH^- \rightarrow Cd(OH)_2 + 2e$) and the nickel electrode is reduced ($2NiO(OH) + 2H_2O + 2e \rightarrow 2Ni(OH)_2 + 2OH^-$). The overall charge/discharge reaction is:

$$Cd + 2NiO(OH) + 2H_2O \underset{CHARGE}{\overset{DISCHARGE}{\rightleftarrows}} Cd(OH)_2 + 2Ni(OH)_2 \tag{1.20}$$

Nickel cadmium batteries can operate for 500 cycles and for 5 to 7 years in standby mode and reach a specific energy of 70 Wh/Kg. They have fast charging time and good performance stability with temperature. They are disadvantaged by poor charge retention, a lower capacity than other batteries and the cadmium toxicity that is an environmental concern.

1.5.5. Nickel-metal hydride batteries

The nickel-metal hydride batteries (NIMH) are a new technology with the same characteristics as the nickel cadmium batteries. NIMH batteries are replacing nickel-cadmium cells because of their higher specific energy (100 Wh/Kg). NIMHs are interesting as low cost power sources for computers, mobile phones and other portable electronics. In NIMH, hydrogen is stored in a metal alloy that serves as active negative electrode. This alloy adsorbs and desorbs hydrogen ions as the battery charges and discharges. Rare earth AB_5 compounds like $LaNi_5$ and or AB_2 alloys based on titanium or zirconium are the most common negative electrodes for NIMHs. The other electrode is made of nickel oxyhydroxide (NiOOH) and the electrolyte is an aqueous solution of potassium hydroxide (NaOH). During discharge, the NiOOH is reduced by water and an electron into nickel hydroxide $Ni(OH)_2$ and hydroxide ions (OH^-). The metal hydride (MH) is oxidized by OH^- into metal alloy M with water and an electron. The complete NIMH cell discharge reaction is:

$$MH + NiOOH \rightarrow M + Ni(OH)_2 \qquad (1.21)$$

The charge reaction is the opposite one. When overcharged, the NIMHs positive electrode reaches full charge before the negative one and starts to produce oxygen gas. With an appropriate separator, the gas can diffuse to the negative electrode and it oxidizes the hydrogen to produce water. This mechanism naturally prevents an increase in pressure. Apart from their high capacity and their fast recharging capability, NIMHs batteries take advantage of a long cycle life. Nevertheless, this type of device is disadvantaged by its poor charge retention and the higher cost of the metal hydride electrodes.

1.5.6. Zinc-carbon batteries

Zinc-carbon batteries have been developed by a telegraphic engineer named Georges-Lionel Leclanché in 1866. The majority of primary batteries worldwide are of this type albeit their market is declining as they are replaced by zinc-alkaline systems or secondary batteries. Zinc carbon cells are cheap and show acceptable performances (110 Wh/kg and 250 Wh/L) for a great number of low consuming applications like flashlights and small portable radios. They use a zinc anode, a manganese dioxide cathode and an aqueous solution of ammonium chloride and/or zinc chloride. During the discharge, the zinc is oxidized and the manganese dioxide is reduced. The overall reaction of the cell is:

$$Zn + 2MnO_2 \rightarrow ZnO \cdot Mn_2O_3 \tag{1.22}$$

Apart from well-known Leclanché cells, this category of batteries also involves zinc-chloride batteries. Zinc-chloride batteries use thin paper separators between the electrodes and thus dispose of a higher volume for active materials and can reach a higher capacity than Leclanché cells. Zinc-carbon batteries are characterized by a low cost per watt even if their power density is not so high.

1.5.7. Lead acid batteries

The lead acid battery has been a commercial success since Raymond Gaston Planté developed the first prototype in 1860. In 1999, lead batteries represent 40 to 45% of the sales values of all batteries in the world [51]. Most of these batteries are used in vehicles for which they provide energy for engine starting and car lighting. Lead acid batteries can also power telephone systems, power tools and emergency lighting systems. These batteries are the least expensive ones albeit they reach a low specific energy per weight of 50 Wh/kg. The lead acid batteries are also very versatile as they are available in various sizes and powers.

The negative electrode is made of lead and the positive electrode is made of lead oxide (PbO_2). As the cell discharges, both electrodes are converted to lead sulphate ($PbSO_4$). During charge the process reverses. In contrast to other batteries, there is no ion transport in lead batteries as they only involve a dissolution-precipitation mechanism. The complete reaction of such a cell is:

$$Pb + PbO_2 + 2H_2SO_4 \underset{CHARGE}{\overset{DISCHARGE}{\rightleftarrows}} 2PbSO_4 + 2H_2O \tag{1.23}$$

When overcharged, the cell produces oxygen and hydrogen gases by water decomposition. In some designs, H_2 production can lead to explosion risk. The lead acid batteries are disadvantaged by their relatively low cycle life (50-500 cycles) and their relatively low energy density albeit they show a cell voltage superior to 2 V. A long term storage in a discharged condition can lead to irreversible polarization of electrodes by sulfation.

In the past years, lead-acid batteries have been designed for small portable applications. They are referred to as valve regulated lead-acid batteries (VRLA), are sealed and maintenance free. They work like the other lead-acid cells but are based on thin films with an electrolyte immobilized by absorption in a mat or in form of a gel. VRLA reach a maximal specific energy of 35 Wh/kg in cylindrical form.

1.5.8. Alkaline-manganese dioxide batteries

The alkaline-manganese dioxide batteries are dominant in the portable battery market since their introduction in the 1960s. They are primary batteries meaning that they can not be recharged. Nevertheless, they take advantage of their low cost and low internal resistance to be used in many applications such as remote controls, radios, CD players, cameras and camcorders. Their most familiar designs are the cylindrical (AA size) and the button configuration. The alkaline battery can deliver 130 Wh/kg with a voltage of 1.2 V (AA). The electrolyte is made of concentrated KOH which as a good ionic conductivity and prevents hydrogen gassing. The anode is made of metallic zinc powder with a high reactive surface and the cathode of manganese oxide (MnO_2). The total cell reaction on continuous discharge is:

$$2MnO_2 + Zn + 2H_2O \rightarrow 2MnOOH + Zn(OH)_2 \qquad (1.24)$$

In this case, water management can be a problem as a lack of H_2O can stop the reaction. For intermittent discharge the reactions changes to:

$$3MnO_2 + 2Zn \rightarrow Mn_3O_4 + 2ZnO \qquad (1.25)$$

Here the water management is no a problem anymore. Alkaline batteries are also disadvantaged by their low energy density compared to other small batteries.

1.6. Micro fuel cells (μSOFCs)

Micro-solid oxide fuel cells (μSOFCs) are small energy sources produced by means of microfabrication processes and thin film technology [33, 54]. The idea of a SOFC made of thin films has been presented by Barnett in 1990 [55]. In this paper, the author already pointed out the benefits of reducing the PEN thickness and therefore its ionic resistance. The low resistance permits to reduce the temperature of operation below 500°C and therefore the materials requirements and the costs [18]. The scaling down of a “bulk” technology to thin films implies new challenges and questions. Most of these points are related to the thermal stability of thin PEN membranes and to the behaviour of thin films having a different microstructure than sintered ceramics. The lower temperature also implies new materials choices because the ionic conductivity, the thermal expansion and the chemical degradation are different at 500°C.

1.6.1. From fuel cells to micro solid oxide fuel cells

As F.T. Bacon wrote in 1969 [56], it seems “that electrochemical storage of energy is the most hopeful method for achieving a portable storage device”. In these early years, microsystems were not developed but fuel cells were already shipped in Apollo and Gemini space flights [13, 56]. The production of electricity within a space ship was not governed by the costs but by the efficiency (i.e. by the total weight of the shuttle). The transformation of hydrocarbon fuels into electrical energy by fuel cells is not limited by the Carnot cycle. Therefore, the fuel cells benefit from their higher efficiency compared to electrical generators based on the combustion of hydrocarbon fuels. On the other hand, their high temperature of operation and the corrosivity of chemicals involved in their operation processes (mainly for phosphoric acid fuel cells) imply higher material requirements and therefore higher costs. On earth, the good availability (until now) low cost oil resource and its cost always limited the development of fuel cells. Today, mainly because of the imminent lack of oil and environmental concerns, fuel cells are being developed as green power sources for vehicles [57] or as generators for buildings. These solid oxide fuel cells have very large dimensions and operate at around 1000°C.

The combination of MEMS (Micro Electrical and Mechanical Systems) and fuel cells technologies opens a new field of applications. Micro fuel cells having a volume of some cubic centimetres can be used for laptops, portable video games systems or mobile phones. At the moment, fuel cells operating near room temperature, such as polymer electrolyte membrane fuel cells or direct methanol fuel cells, are favoured. Here again, the relatively low material requirements of these type of cells helps them to be competitive on the market because they are relatively easy to produce. For example, PEMFCs and DMFCs use commercial polymer membranes (e.g. Nafion) that obviously limit their R&D expenses. But at temperatures of around 500°C, micro solid oxide fuel cells can use internal reforming of hydrocarbons [58] and transform their thermal losses into energy by co-generation [59]. Thus, SOFCs have better efficiency and can achieve higher energy density per weight of device (in Wh/kg). μSOFCs can also take advantage of the high energy capacity of the hydrogen gas. Thus, μSOFCs can dispose of smaller fuel tanks and can reach a better specific energy (in Wh/L of device). μSOFCs are very good candidates to replace Li-ion batteries in portable applications [54, 60]. Apart from the Li-ion rechargeable batteries, zinc-air primary cells are the biggest competitor for μSOFCs because of their high energy density. At the moment Zn-air cells are not rechargeable but developments are ongoing [53]. In the future Zn-air batteries could be a very competitive power sources that might delay considerably the introduction of μSOFCs.

1.6.2. Existing micro fuel cells

The importance of micro fuel cells has improved with the demand of small power sources for increasingly consuming portable electronics. The most important developments have been realized in the field of micro polymer electrolyte membrane fuel cells (μPEMFCs) and micro direct methanol fuel cells (μDMFCs) [61]. They both have the advantage of operating at low temperatures (below 100°C) and having a polymer membrane as electrolyte. μSOFCs are hotter (400°C-600°C) but their specific energy and energy density are far better (Figure 14). Thus, unless their development is more difficult, they will probably be very interesting portable power sources in a near future.

The power and the autonomy of a micro fuel cell mostly depend on the energy density of its fuel. For the comparison, the energy densities (in Wh/kg of fuel) of all the fuels that will be discussed in this chapter are reported in the next table:

Table 1: Energy densities of several fuels used in micro fuel cells compared with nuclear material from [61] and [62].

Fuel	Density	Energy density	Cell type
Sodium borohydride ($NaBH_4$)	1.07 kg/l	3600 Wh/kg	μPEMFC
Formic acid (CHOOH)	1.22 kg/l	1532 Wh/kg	μDFAC
Methanol (CH_3OH)	0.79 kg/l	5500 Wh/kg	μDMFC
Most liquid hydrocarbons	~0.6-0.8 kg/l	~12400 Wh/kg	μSOFC and μPEMFC with reformer
Hydrogen gas		33200 Wh/kg	μSOFC, μPEMFC
Nuclear material		2800000 Wh/kg	Nuclear power plant

1.6.2.1. Micro polymer electrolyte membrane fuel cells

Micro polymer electrolyte membrane fuel cells (μPEMFCs) with or without an on-board hydrocarbon reformer have been developed. μPEMFCs without a reformer are simpler and have a higher efficiency because the reformer requires significant energy from the device and therefore lowers its total efficiency [63]. Without a reformer, the only possible fuel is pure hydrogen and its storage becomes the main problem. The availability of a material with a high efficiency of hydrogen storage is a very critical point for this type of devices. With a reformer, μPEMFCs are fuelled by hydrocarbons (e.g. methanol) or by sodium boro hydride.

With the advantage of their low operation temperature of, μPEMFCs can be fabricated on polymer substrates such as PDMS, PMMA or SU8. These substrates are easy to structure by means of hot embossing or molding, photolithography or laser ablation and are therefore very convenient for micro-channel fabrication [64]. μPEMFCs can also be fabricated on silicon or glass wafers. The electrolytes are made of commercial polymer membranes such as Nafion.

The best performances for μPEMFCs have been obtained by the group of Yu with a cell of 5 cm^2 [65] (Figure 11.a) and with twin cells of 3 cm^2 area [66] mounted on silicon, with respectively 194 mW/cm^2 and 190 W/cm^2. These high values have been obtained at room temperature and with pure oxygen in place of air.

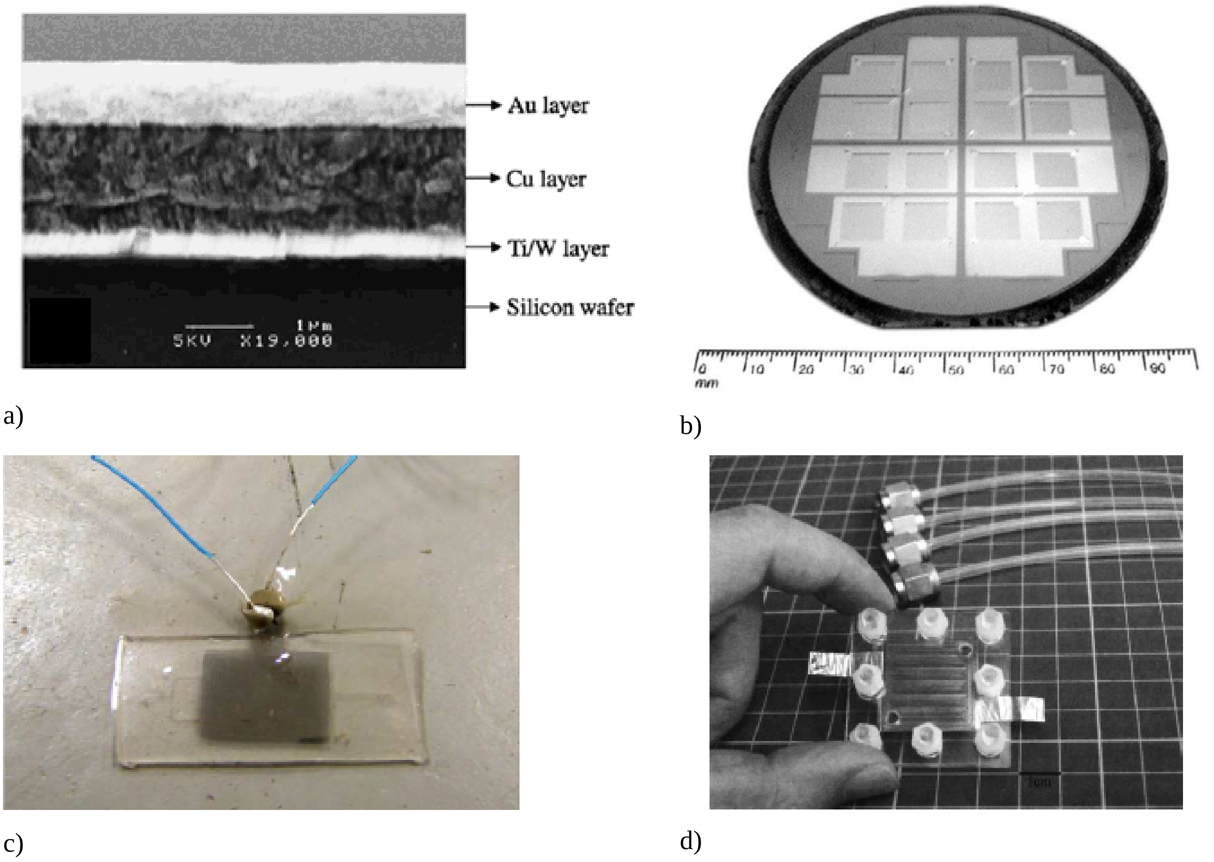

a)

b)

c)

d)

Figure 11: a) SEM cross section of a μPEMFCs fabricated by Yu [65], b) array of 4 μPEMFCs fabricated on a silicon wafer by Lee [67], c) PDMS based μPEMFCs by Shah [68], d) PMMA based μPEMFCs by Hsieh [69].

The group of Prinz has developed 2 and 4 μPEMFCs arrays with flip-flop interconnection on glass and silicon substrates (Figure 11.b). They show a maximal power density of 42 mW/cm^2 with a cell surface of 5 cm^2 [70]. Shah et al. presented cells mounted on PDMS (Figure 11.c) and showing a maximal power density of 35 mW/cm^2, when they are heated to 60°C [68]. Hsieh et al. used laser ablation to create gas channels in PMMA substrates (Figure 11.d) to realize cells that reach a power density of 31 mW/cm^2 at room temperature [69].

1.6.2.2. *Micro direct methanol fuel cells*

Micro direct methanol fuel cells (µDMFCs) directly convert methanol (CH_3OH) and oxygen into electricity producing carbon dioxide and water. They are advantaged by their lightweight, smallness, easy refilling and long duration [61]. Most of these cells have an electrolyte made of a commercial polymer membrane such as Nafion [71] or PVDF [21]. The anode catalyst and the water management are two majors concerns. The catalyst promotes the dissociation of the methanol into protons directly onto the polymer electrolyte. Metals such as palladium, platinum and ruthenium can be used for this purpose [71, 72]. The water management consists of keeping the ratio of water molecules lost to the air per molecule of methanol consumed in the reaction constant. The long term stability of the cell is fully dependent on this ratio that should remain equal to 2 [73]. It’s estimated that 7 to 12 years are needed for µDMFCs to compete with lithium-ion batteries in term of size, cost and overall performances [74].

Toshiba and Hitachi have already presented in 2005 prototypes powering MP3 players [11] and a lot of other international companies are active in the field [61]. PolyFuel claims record for the maximal power density achieved by a µDMFCs with 200 mW at 70°C [75]. Their cell is based on a very thin (20 µm) hydrocarbon membrane used as electrolyte. MEMS based µDMFCs including a silicon membrane micro pump have been fabricated by Yao [76]. Blum et al. presented a µDMFC with plastic housing that show a stable operation for 900h and a peak power density of 12.5 mW/cm^2 [73].

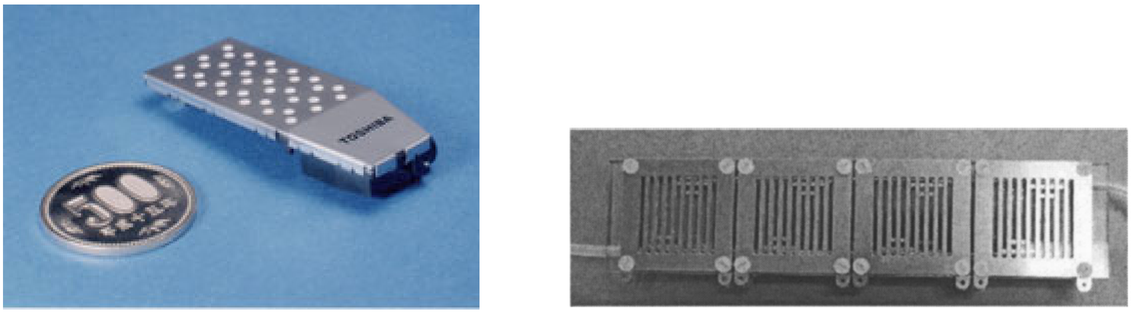

a) b)

Figure 12: a) Toshiba prototype of µDMFC, b) 8 cells air breathing µDMFC stack [77].

1.6.2.3. *Micro direct formic acid fuel cells*

Micro direct formic acid fuel cells (μDFAFCs) convert formic acid (CHOOH) and oxygen into carbon dioxide and water to produce energy. The formic acid does not have many of the limitations of methanol and hydrogen. CHOOH is non-flammable at room temperature and relatively benign chemically as it can even be present in food. The major disadvantage of the formic acid is its relatively small volumetric energy of 1870 Wh/L.

A stack of 15 micro DFACs provides enough energy for the operation of a laptop computer [62]. This stack delivers 30 W at 60 mW/cm^2 and can feed a computer for 2.5 hours using a 280 ml tank of fuel. Chu et al. present μDFACs to be used as on-chip power sources [78]. This system is based on porous silicon membranes directly wet etched into Si wafers. These devices reach a power density of 30 mW/cm^2. The maximum power density for μDFACs was reached by Kundu et al. with a value of 110 mW/cm^2 at 30°C with a Nafion 112 membrane [79].

Figure 13: μDFAFCs stack providing 30 W within a volume of 88 mm x 70 mm x 50 mm [62].

1.6.2.4. *Micro solid oxide fuel cells*

Micro solid oxide fuel cells (μSOFCs) take advantage of the high energy density of the hydrogen gas of 33200 Wh/kg compared to 5500 Wh/kg for methanol [61]. Some studies show that the μSOFCs could ultimately deliver an energy density three times bigger than the long-term goal for lithium-ion batteries [80]. The thermal management is a critical technological point for μSOFCs. Even though the temperature is reduced from 1000°C to 500°C with their miniaturization, the thermal insulation is still a major problem for μSOFCs [80]. At this temperature, it is still possible to reform hydrocarbon directly within the cell and to use the cogeneration, thus the main advantages of the high temperature remain. Finally, the temperature directly influences the design of the μSOFCs and especially the PEN membrane (see paragraph 2.2). At the moment, only a few demonstrators have been fabricated according to the literature and no long-time stability tests have been reported. For the large SOFCs power plants, the carbon poisoning, the interconnect stability and the formation of second phases between the electrodes and the electrolyte are of major concern. All these effects depend on the temperature and should be reduced or even eliminated within µSOFCs. Figure 14 shows a comparison in term of specific energy in Wh/L and energy density in Wh/kg of different primary and secondary batteries with micro fuel cells. At the top right of the graph, the fuels cells are lighter and smaller than other devices. µSOFCs have the best potential because of their higher efficiency than the direct methanol fuel cells and polymer electrolyte membrane fuel cells.

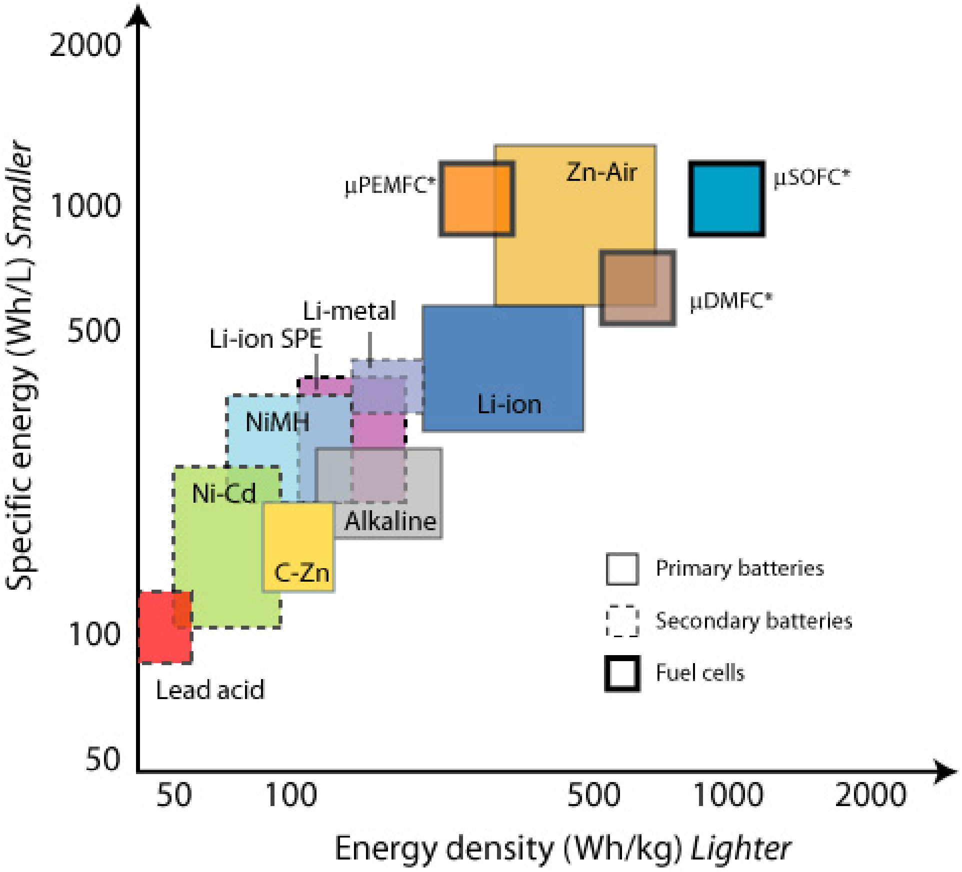

Figure 14: Specific energy (per mass of device) and energy density (per volume of device) of several portable energy sources from [81]. * indicates estimated values as these devices are not fully developed yet.

1.7. Aim of this work

The aim of this work is to study materials and fabrication issues for micro solid oxide fuel cells working in the range of 400°C to 550°C based on silicon MEMS technology and of millimeter to centimeter dimension. At the beginning, this temperature range was chosen rather for stability reasons than based on actual knowledge of required gas forming temperatures. With the evolvement of this work, however, it has been shown by the ETH thermodynamics laboratory that 530 °C would be sufficiently high to reform butane with high efficiency. Silicon was chosen as substrate because it is conveniently patterned by dry etching techniques, and because it is - apart of a thin oxide scale formation - a stable material at the mentioned temperature range. It was also decided to concentrate on membrane structures with defined gas separation, because such structures should be more efficient and safer in operation than single chamber fuel cells. This implies, however, the solution to a heavy technical problem: the weak mechanical stability of thin membranes made of brittle ceramic films. Hence, as further goal, the study of means to reinforce such brittle membrane structures was included into the work program. More specifically, it was attempted to create a metal-ceramic composite membrane combining the functional properties of the electrolyte ceramics with the toughness of a nickel grid structure.

1.8. Outline

Apart from this first introducing chapter dedicated to fuel cells in general and to the working principle, the materials and the design of SOFCs, the thesis has been structured as follow:

Chapter 2 covers the state of the art for the fabrication of μSOFCs with dimensions in the millimeter range. The existing designs of μSOFCs and their properties are discussed and then the deposition methods for thin films are reviewed.

Chapter 3 presents the study of YSZ, CGO, LSCO and porous platinum thin films deposited by reactive magnetron sputtering. Structural and compositional analysis, ionic and electronic conduction, and thermal stress, are the major issues.

Chapter 4 discusses the microfabrication of μSOFCs and the problems related to the miniaturization of such devices. Electrical characterization of the fabricated cells and lifetime tests are also presented.

Chapter 5 gives an overall discussion, conclusions and reviews potential improvements for the future.

1.9. References

1. IEA, *Key World Energy Statistics.* 2005.
2. Pacala, S. and R. Socolw, *Stabilization wedges: solving the climate problem for the next 50 years with current technologies.* Science, 2004. **305**: p. 968-972.
3. Hirsch, R.L., R.H. Bezdek, and R.M. Wendling, *Peaking oil production: Sooner rather than later?* Issues in Science and Technology, 2005. **21**(3): p. 25-30.
4. Marban, G. and T. Valdés-Solis, *Towards the hydrogen economy?* International journal of hydrogen Energy, 2007. **32**: p. 1625-1637.
5. McDowall, W. and M. Eames, *Forecasts, scenarios, visions, backasts and roadmaps to the hydrogen economy: A review of the hydrogen futures literature.* Energy policy, 2006. **34**: p. 1236-1250.
6. Züttel, A., *Materials for hydrogen storage.* Materials Today, 2003. **6**(9): p. 24-33.
7. Dixon, R.K., *Advancing towards a hydrogen economy: status, opportunites and barriers.* Mitigation and Adaptation Strategies for Global Change, 2007. **12**: p. 325-341.
8. Kordesh, K. and G. Simader, *Fuel cells and their applications*. 1996, Weinheim: VCH.
9. *The Honda FCX fuel cell vehicles.* AutoTechnology, 2007(SPEC. ISS 2007): p. 59-63.
10. Osman, A. and R. Ries, *Life cycle assessment of electrical and thermal energy systems for commercial buidings.* International Journal of Life Cycle Assessment, 2007. **12**(5): p. 308-316.
11. *News: Toshiba, Hitachi DMFCs feature in prototype audio players, cell phones.* Fuel Cells Bulletin, 2005. **11**: p. 8.
12. Groove, W.R., Philos. Mag., 1839. **Ser. 3**.
13. Perry, M.L. and T.F. Fuller, *A historical perspective of fuel cell technology in the 20th century.* Journal of the Electrochemical Society, 2002. **149**(7): p. S59-S67.
14. Minh, N.Q., *Ceramic Fuel Cells.* Journal of the American Ceramic Society, 1992. **76**(3): p. 563-588.
15. Ostwald, Z., Z. Elektrochemie, 1894. **1**: p. 122.
16. Steele, B.C.H. and A. Heinzel, *Materials for fuel-cell technologies.* Nature, 2001. **414**: p. 345-352.
17. Kinoshita, K., *Electrochemical oxygen thenology*. 1992, New York: John Wiley & Sons.
18. Doshi, R., et al., *Development of Solid-Oxide Fuel Cells That Operate at 500°C.* Journal of Electrochemical Society, 1999. **146**(4): p. 1273-1278.
19. Huang, H., et al., *High-performance ultrathin solid oxide fuel cells for low-temperature operation.* Journal of the Electrochemical Society, 2007. **154**(1): p. B20-B24.

20. Gauckler, L.J., et al., *Solide Oxide Fuel Cells: Systems and Materials.* Chimia, 2004. **58**(12): p. 837-850.
21. Blum, L., et al., *Worldwide SOFC technology overview and benchmark.* International Journal of Applied Ceramic Technology, 2005. **2**(6): p. 482-492.
22. Vora, S.D., *Advances in solid oxide fuel cell technology at Siemens Westinghouse.* Advanced Materials and Processes, 2005. **163**(8): p. 54.
23. Schmidt, M., *The Hexis Project: Decentralised Electricity Generation with Waste Heat Utilisation in the Household.* Fuel Cells Bulletin, 1998. **1**: p. 9-11.
24. Eyraud, C., et al., Académie des Sciences, 1961. **252**: p. 1599.
25. Hibino, T., et al., *Single-chamber solid oxide fuel cells at intermediate temperatures with various hydrocarbon-air mixtures.* Journal of the Electrochemical Society, 2000. **147**(8): p. 2888-2892.
26. Kuhn, M., et al., *Direct-write microfabrication of single-chamber solid oxide fuel cells with interdigitated electrodes.* Materials Research Society Symposium Proceedings, 2007. **972**(211-216).
27. Buergler, B.E., et al., *From macro- to micro-single chamber solid oxide fuel cell.* Journal of Power Sources, 2007. **171**: p. 310-320.
28. Srikar, V.T., et al., *Structural design considerations for micromachined solide-oxide fuel cells.* Journal of Power Sources, 2004. **125**: p. 62-69.
29. Jung, H.-W., et al., *Characterization of thin-film YSZ deposited via EB-PVD technique in anode-supported SOFCs.* Journal of Electrochemical Society, 2006. **153**(6): p. A961-A966.
30. Weber, A. and E. Ivers-Tiffe, *Materials and concepts for solide oxide fuel cells (SOFCs) in stationary and mobile applications.* Journal of Power Sources, 2004. **127**: p. 273-283.
31. Takeyama, T., et al., *d-Bi2O3 thin films deposited on dense YSZ substrates by CVD method under atmospheric pressure for intermediate temperature SOFC applications.* Surface Coating Technology, 2006. **16-17**(4797-4801).
32. Taniguchi, I., R.C.v. Landschoot, and J. Shoonmann, *Electrostatic spray deposition of Gd0.1Ce0.9O1.95 and La0.9Sr0.1Ga0.8Mg0.2O2.87 thin films.* Solid State Ionics, 2003. **160**(3-4): p. 119-123.
33. Fleig, J., H.L. Tuller, and J. Maier, *Electrodes and electrolytes in micro-SOFCs: a discussion of geometrical constraints.* Solid State Ionics, 2004. **174**: p. 261-270.
34. Radhakrishnan, R., A.V. Virkar, and S.C. Singhal, *Estimation of charge-transfer resistivity of Pt cathode on YSZ electrolyte using patterned electrodes.* Journal of Electrochemical Society, 2005. **152**(5): p. A27-A36.
35. Gödickemeier, M., K. Sasaki, and L.J. Gauckler, *Electrochemical characteristics of cathodes in solid oxide fuel cells based on ceria electrolytes.* Journal of the Electrochemical Society, 1997. **144**(5): p. 1635-1645.

36. Beckel, D., *Thin film cathodes for micro solid oxide fuel cells*, in *Nichmetallische und inorganishe Material*. 2007, Swiss Federal Institue of Technology ETH: Zurich.
37. Yu, H.-C., et al., *Electrochemical characterization and performance evaluation of intermediate temperature solid oxide fuel cell with La0.75Sr 0.25CuO2.5-d cathode.* Journal of Power Sources, 2005. **152**(1-2): p. 22-26.
38. Kim, G., et al., *Oxygen exchange kinetics of epitaxial* $PrBaCo_2O_{5+d}$ *thin films.* Applied Physics Letters, 2006. **88**: p. 263106.
39. Jiang, S.P., *Hydrogen oxidation at the nickel and platinum electrodes on yttria-tetragonal zirconia electrolyte.* Journal of Electrochemical Society, 1997. **144**(11): p. 3777-3784.
40. Uchida, H., M. Yoshida, and M. Watanabe, *Effects of ionic conductivities of zirconia electrolytes on polarization properties of platinum anodes in solid oxide fuel cells.* Journal of Physical Chemistry, 1995. **99**(10): p. 3282-3287.
41. Suzuki, M., et al., *High power density solid oxide electrolyte fuel cells using Ru/Y2O3 stabilized zirconia cermet anodes.* Solid State Ionics, 1993. **62**(1-2): p. 125-130.
42. Jiang, S.P. and S.H. Chan, *A review of anode materials development in solid oxide fuel cells.* Journal of Materials Science, 2004. **39**: p. 4405-4439.
43. Goodenough, J.B. and Y.-H. Huang, *Alternative anode materials for solid oxide fuel cells.* Journal of Power Sources, 2007. **173**: p. 1-10.
44. Abe, H., et al., *Microstructural control of Ni-YSZ cermet anode for planar thin-film SOFCs.* Fuel Cells Bulletin, 2006. **3**: p. 12-15.
45. Kang, S., et al., *Thin-film solid oxide fuel cells on porous nickel substrates with multistage nanohole array.* Journal of the Electrochemical Society, 2006. **153**(3): p. A554-A559.
46. Fleig, J., *Solid oxide fuel cell cathodes: polarization mechanisms and modeling of the electrochemical performance.* Annual Review of Material Research, 2003. **33**: p. 361-382.
47. Singhal, S.C. and K. Kendall, *High temperature solid oxide fuel cells: Fundamentals, design and applications*, ed. S.C. Singhal and K. Kendall. 2003, Oxford: Elsevier Ltd.
48. Hammouche, A., et al., *Electrocatalytic Properties and Nonstoichiometry of the High Temperature Air Electrode Lal-xSrxMn03.* Journal of the Electrochemical Society, 1991. **138**: p. 1212-1216.
49. Prestat, M., J.-F. Koenig, and L.J. Gauckler, *Oxygen reduction at thin dense La0.52Sr0.48Co 0.18Fe0.82O3-d electrodes: Part I: Reaction model and faradaic impedance.* Journal of Electroceramics, 2007. **18**(1-2): p. 87-101.
50. Chan, S.H., K.A. Khor, and Z.T. Xia, *A complete polarization model of a solid oxide fuel cell and its sensitivity to the change of cell component thickness.* Journal of Power Sources, 2001. **93**: p. 130-140.
51. Linden, D. and T.B. Reddy, *Hanbook of batteries*. McGraw-Hill Handbooks. 2002, New York: McGraw-Hill.

52. Elmore, G.W. and H.A. Moos, *US Patent 3419900*.

53. Smedley, S.I. and X.G. Zhang, *A regenerative zinc-air fuel cell.* Journal of Power Sources, 2007. **165**: p. 897-904.

54. Bieberle-Hütter, A., et al., *A micro-solid oxide fuel cell system as battery replacement.* Journal of Power Sources, 2008. **177**(123-130).

55. Barnett, S.A., *A new solid oxide fuel cell design based on thin film electrolytes.* Energy, 1990. **15**(1): p. 1-9.

56. Bacon, F.T., *Fuel cells, past, present and future.* Electrochimica Acta, 1969. **14**: p. 569-585.

57. Ormerod, R.M., *Solid oxide fuel cells.* Chemical Society Review, 2002. **32**: p. 17-28.

58. Stutz, M.J., N. Hotz, and D. Poulikakos, *Optimization of methane reforming in a microreactor-effects of catalyst loading and geometry.* Chemical Engineering Science, 2006. **61**(12): p. 4027-4040.

59. Mantzaras, J., et al., *Fuel cell modeling and simulations.* Chimia, 2004. **58**(12): p. 857-868.

60. *http://www.mhtx.com*, Manhattan Scientific.

61. Kundu, A., et al., *Micro-fuel cells-Current development and applications.* Journal of Power Sources, 2007. **170**: p. 67-78.

62. Miesse, C.M., et al., *Direct formic acid fuel cell portable power system for the operation of a laptop computer.* Journal of Power Sources, 2006. **162**(1): p. 532-540.

63. Radulescu, M., et al., *Experimental results with a natural gas cogeneration system using a polymer exchange membrane fuel cell.* Journal of Power Sources, 2006. **159**(2): p. 1142-1146.

64. Becker, H. and C. Gärtner, *Polymer microfabrication technologies for microfluidic systems.* Analytical and Bioanalytical Chemistry, 2008. **390**(1): p. 89-111.

65. Yu, J., et al., *Fabrication of miniature silicon wafer fuel cells with improved performance.* Journal of Power Sources, 2003. **124**: p. 40-46.

66. Yu, J., et al., *Fabrication of a miniature twin-fuel-cell on silicon wafer.* Electrochemica Acta, 2003. **48**: p. 1537-1541.

67. Lee, S.J., et al., *Design and fabrication of a micro fuel cell array with 'flip-flop' interconnection.* Journal of Power Sources, 2002. **112**(410-418).

68. Shah, K., W.C. Shin, and R.S. Besser, *A PDMS micro proton exchange membrane fuel cell by conventional and non-conventional microfabrication techniques.* Sensors and Actuators B, 2004. **97**: p. 157-167.

69. Hsieh, S.-S., et al., *A novel design and microfabrication for a micro PEMFC.* Microsystem Technologies, 2004. **10**(121-126).

70. Lee, S.J., et al., *Design and fabrication of a micro fuel cell array with ‘‘flip-flop’’ interconnection.* Journal of Power Sources, 2002. **112**: p. 410-418.

71. Liu, X., et al., *Novel modification of Nafion117 for a MEMS-based micro direct methanol fuel cell (μDMFC).* Journal of Micromechanics and Microengineering, 2006. **16**: p. S226-S232.

72. Lu, G.Q., et al., *Development and characterization of a silicon-based micro direct methanol fuel cell.* Electrochemica Acta, 2004. **49**(5): p. 821-828.
73. Blum, A., et al., *Water-neutral micro direct-methanol fuel cell (DMFC) for portable applications.* Journal of Power Sources, 2003. **117**: p. 22-25.
74. Ilic, D., et al., *Fuel cells and batteries: Competition or separate paths?* Journal of Power Sources, 2006. **155**: p. 72-76.
75. *PolyFuel's ultra-thin membrane claims record.* Fuel Cells Bulletin, 2007. **1**: p. 8.
76. Yao, S.-C., et al., *Micro-electro-mechanical systems (MEMS)-based micro-scale direct methanol fuel cell development.* Energy, 2006. **31**: p. 636-649.
77. Lu, G.Q. and C.Y. Wang, *Development of High Performance Micro DMFCS and a DMFC Stack.* Journal of Fuel Cell Science and Technology, 2006. **3**: p. 131-136.
78. Chu, K.-L., et al., *A Nanoporous Silicon Membrane Electrode Assembly for On-Chip Micro Fuel Cell Applications.* Journal of Microelectromechanical Systems, 2006. **15**(3): p. 671-677.
79. Zhu, Y., S.Y. Ha, and R.I. Masel, *High power density direct formic acid fuel cells.* Journal of Power Sources, 2004. **130**: p. 8-14.
80. Nikbin, D., *Micro SOFCs: why small is beautiful.* The Fuel Cell Review, 2006. **(April/May)**(21-24).
81. Broad, R.J., *Recent developments in batteries for portable consumer electronic applications.* Interface, 1999. **8**(3): p. 20-23.

State of the art of µSOFCs

2.1. Micro solid oxide fuel cells

2.1.1. Actual performances of existing demonstrators

Prior to the start of this work in 2003, only a few reports were available on µSOFCs. In 1990, S.A. Barnett described for the first time a SOFC fabricated with thin films [1]. He demonstrated that such a device can operate at temperature below 750°C and deliver a power of approximately 500 mW/cm^2 with a YSZ electrolyte of thickness comprised between 0.5 to 10 µm. He already pointed out the difficulty to deposit dense and crack free thin films on porous substrates and proposed to etch them subsequently. In 2002, Jankowski et al. presented the first µSOFC demonstrator. They have processed a silicon based µSOFC by mean of photolithography and silicon wet etching [2]. This cell reached a power density of 145 mW/cm^2 with hydrogen fuel at 600°C, and contained a 1.2 µm thick YSZ electrolyte made by sputtering. The anode was made of a 0.5 µm thick nickel layer and the anode is made of 0.8 µm thick silver layer. The PEN membrane was supported by a patterned silicon nitride layer. The cell dimensions were 2 x 2 mm^2 and the openings in the silicon nitride layer were squares of 5 x 5 µm^2. The grid covered 75% of the total cell surface and as the nitride is not active in any manner for the cell operations the total output power per device was relatively small. But this work, showed that µSOFCs can be implemented on a silicon substrate and that microfabrication method can be used to render a dense substrate porous and still reaching a reasonable power density.

More recently, the best results for µSOFCs were obtained by Huang et al. with a power density of 400 mW/cm^2 at 400°C [3] in 2007. This power density was measured on a 50 x 50 µm^2 cell. The electrolyte is a very thin YSZ membrane (50 nm) deposited by RF sputtering. The cell areas are comprised between 50 x 50 µm^2 and 240 x 240 µm^2. The energy per device is only 0.2 mW but arrays of cells can be put in parallel. The electrodes were made of porous platinum deposited by DC sputtering. I-V curves were measured on a heater with micro probes on the anode side in the air. This technique allows testing the 832 cells on the silicon wafer in a very short time. Cells mounted on a photostructurable glass (Foturan) have been developed by the group of Gauckler [4] also in 2007. These µSOFCs have maximal power density of 150 mW/cm^2 at 550°C, with a YSZ bilayer electrolyte composed of a 550 nm thick pulsed laser deposited film and of a 200 nm thick spray pyrolised one. The anode is made of sputtered platinum and the cathode of platinum paste (20 µm thick). Before 2007, a single chamber µSOFCs (SC-µSOFC) stack designed by Shao et al. reached a power density of 250 mW/cm^2 and a power output of 350 mW for a total cathode area of 1.42 cm^2. The single chamber design insures the mechanical stability of the PEN and therefore the system is very robust. This construction avoids most of the processing problems due to the membrane fabrication, but the selectivity of electrodes to gases can be a critical issue. In that work, the catalytic oxidation reaction supplies sufficient thermal energy to maintain the system at 500°C-600°C during 200 hours. The cell is supported by a 0.7 mm thick anode made of nickel and of samaria doped ceria (SDC) supporting a SDC electrolyte and a composite cathode made of $Ba_{0.5}Sr_{0.5}Co_{0.8}Fe_{0.2}O_{3-x}$ (BSCF) and SDC.

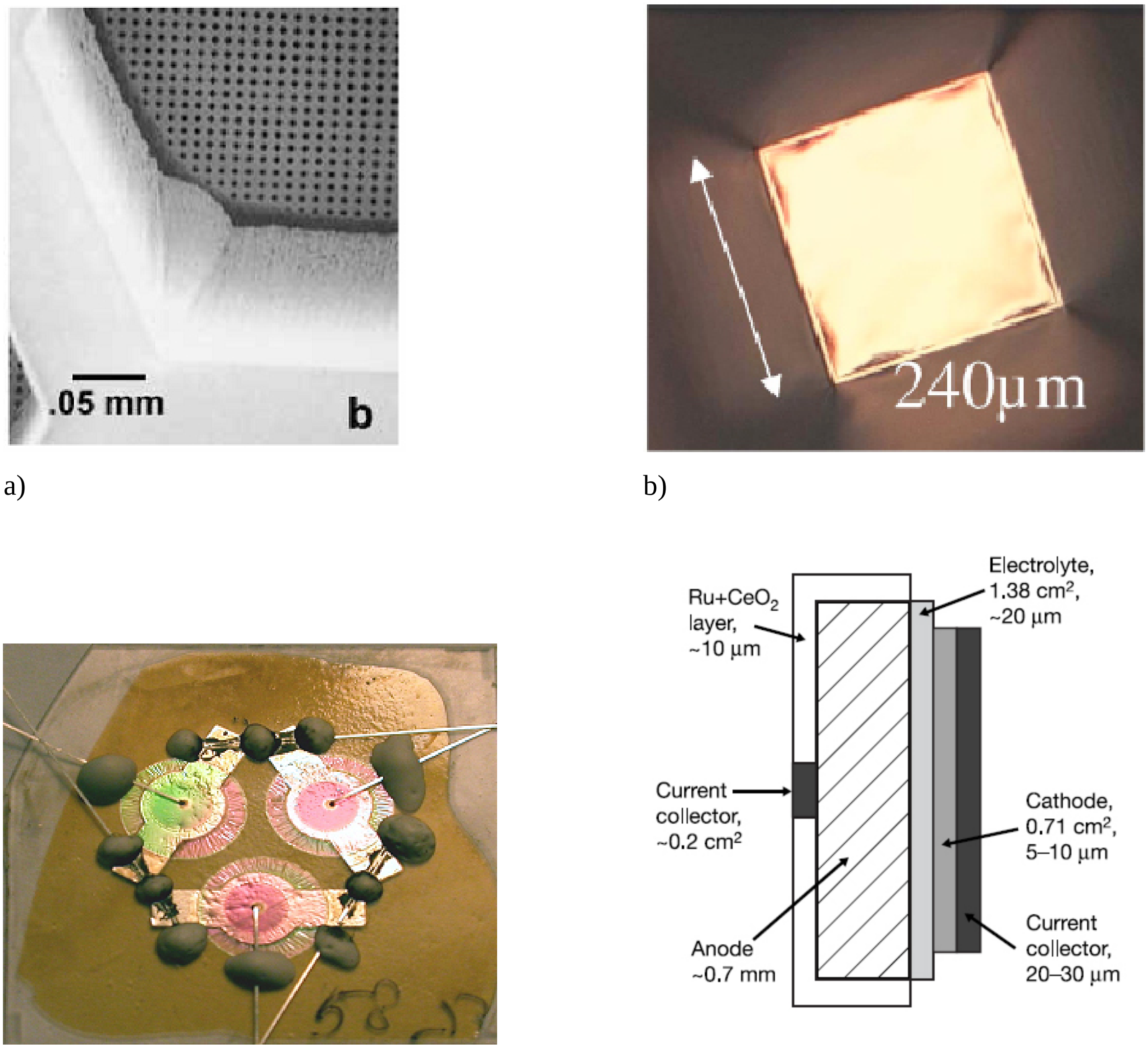

a) b)

c) d)

Figure 1: a) μSOFC supported by a silicon nitride grid [2], b) Free standing μSOFC Huang [3], c) 3 μSOFCs mounted on a Foturan substrate [4] and d) schematic view of a single chamber μSOFC [5].

2.1.2. Comparison with the performances of other type of micro fuel cells

For an easier comparison, the characteristics of the micro solid oxide fuel cells presented in this chapter are compared with other type of micro fuel cells, in the next table:

Table 1: Summary of the characteristics of the micro fuel cells presented in this chapter

Type of cell	Temp.	Fuel	Electrolyte	Single cell size	Substrate	Power density	Ref.
μPEMFC	25°C	H_2		5 cm^2	Si	190 mW/cm^2	[6, 7]
μPEMFC	25°C	H_2		5 cm^2	Si/glass	42 mW/cm^2	[8]
μPEMFC	60°C	H_2		1.4x1.2 cm^2	PDMS	35 mW/cm^2	[9]
μPEMFC	25°C	H_2	Nafion	5 cm^2	PMMA	31 mW/cm^2	[10]
μDMFC	70°C	C_2H_6	Fluorocarbon 20 nm thick			200 mW/cm^2	[11]
μDMFC		C_2H_6		1 cm^2	Si	25 mW/cm^2	[12]
μDMFC		C_2H_6	PVDF	6 cm^2	Plastic	12 mW/cm^2	[13]
μSOFC	400°C	H_2/H_2O	YSZ sputt.	50x50 μm^2	Si	400 mW/cm^2	[3]
SC-μSOFC	~550°C	C_3H_8	SDC	1.42 cm^2	Anode Ni-SDC	250 mW/cm^2	[5]
μSOFC	600°C	H_2	YSZ	5x5μm^2	Si/Si_3N_4	145 mW/cm^2	[2]
μSOFC	550°C	H_2	YSZ bilayer. PLD/Spray	150μm diam.	Foturan	150 mW/cm^2	[4]
μDFAC stack	25°C	Formic acid	Nafion		Si	60 mW/cm^2 Stack 30W	[14]
μDFAC	30°C	Formic acid	Nanoporous Si	100μm diam.	Si	30 mW/cm^2	[15]
μDFAC	60°C	Formic acid	Nafion	5 cm^2		110 mW/cm^2	[16]

As seen in table 2, μSOFCs have the highest energy density but demonstrators are less developed than for direct methanol fuel cells. Furthermore, no stack of μSOFCs has been developed up to now and their dimensions are limited to the micrometer range.

2.1.3. Summary of the actual performances of μSOFCs

Up to now, the micro solid oxide fuel cells are limited in size (<0.01 mm^2). This is mainly due to the electrolyte membrane that is a brittle and thin (< 1μm) ceramic film and to their high temperature of operation (400-550°C) in comparison with other types of micro fuel cells. With their small size, the total output per device of µSOFC is very limited, even if their power density is already of some hundreds of mW/cm^2. The technologies used in the processing of µSOFCs allow for fabrication of cell arrays but there are no reports on this topic in the literature as far as we know. The reason is probably the difficulty to obtain a reproducible process at this stage of development of µSOFCs. Thus, the fabrication of larger cell or array of cells will only occur when the technical problems for small single cell have been solved. As shown in Figure 2, µSOFCs already reach higher power density than other types of cells but are limited by their size. PEMs and DMFCs operate below 70°C and have polymer electrolytes. Thus, they are more ductile than ceramic electrolytes and less subject to the thermal stress.

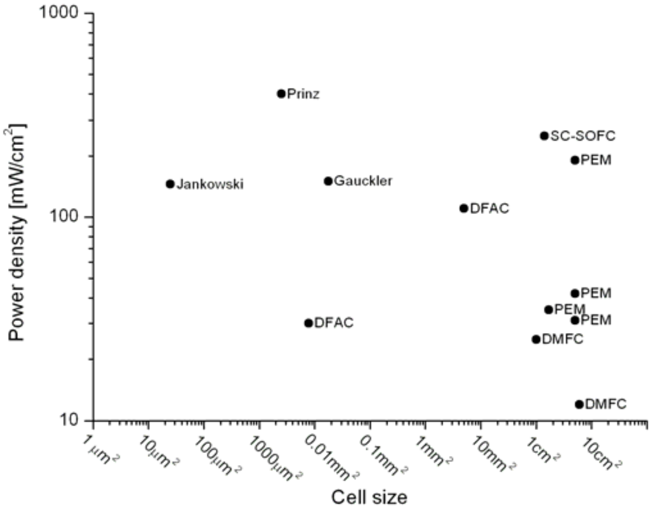

Figure 2: Comparison of µSOFC with other type of micro fuel cells in terms of cell size and power density. References: PEMs [6, 8-10], DMFCs [12, 13], DFACs [15, 16], SC-SOFC[5], SOFCs [2-4].

As far as we know, only one demonstrator of a µDMFC cell has been fabricated for the moment by Toshiba [17]. In comparison and for the reasons exposed before, the µSOFCs will not reach the market within the next 10 to 15 years. One of the previous works shows a cell membrane supported by a stiffener [2] to reduce mechanical and thermal stresses. These cells have a large aperture of 4 mm^2 but only 25% of the surface is effectively producing energy as the silicon nitride used as support is not part of the PEN. Another work shows a cell supported by a porous metallic anode [18]. In this case, the support is an active part of the system and the proportion of active surface is increased. Nevertheless, it is difficult to grow thin and dense electrolyte film on this type of support. In addition, the resistance of the PEN becomes dependent of the electrode microstructure, when its thickness is in the range of the porous electrodes particle size [19]. In conclusion, up to now the literature only reports on µSOFCs prototypes and no long-term study or complete systems have been made.

2.2. The design of micro SOFCs

μSOFCs are subject to severe constraints due to their smallness and their thin PEN membrane. The use of new fabrication methods, with lower processing temperatures such as sputtering, reduces the costs [1]. Furthermore, thin films of rare earth compounds are less expensive than thicker ones. Although μSOFCs have the advantage of low temperatures (400°C-600°C) [20-22], the thermal stress is still a major problem for the membrane stability. The reduction of temperature also requires the thinning down of the electrolyte to keep the area specific resistance (ASR) below the critical value of 0.2 Ω/cm^2. Single chamber μSOFCs [23] could be a solution for thermal stresses. In this design, the whole cell is supported by a thick electrolyte and the ion flux is parallel to this substrate. For better cell efficiency, it is worth to use interdigited electrodes with the smallest gap between them [19], but the photolithography resolution is limited (to ~1 μm) and thus diffusion length is larger with this type of electrode. Futhermore selectivity of the electrodes to gases will still limit the efficiency of such cells and even more when electrodes are very close to each other. In the rest of this paragraph, we will concentrate on two chambers μSOFCs.

Apart from thermo-mechanical stress, residual stress due to processing also plays a role. Most of the deposition methods presented in the next paragraph involve high temperatures steps to crystallize the films. After cooling down from the sputtering temperature, ceramic thin films usually show tensile stress as they have a bigger thermal expansion coefficient than the silicon wafer. This contribution to the stress can be reduced by using other types of substrates. It is still important to consider that most of the microfabrication process tools have been developed for Si.

Heat losses are very important in μSOFCs as the ratio of surface over volume is very high. Heat losses are mainly due to radiation, convection in the gases and conduction to the substrate or to the other parts of the cell.

Finally, the interconnection of the fuel cell elements and the gas channels into the stack remain a problem [24], even if the reduced operation temperatures of μSOFC are of a great advantage. The microfabrication methods can also simplify the stack fabrication.

2.2.1. Thermal stress

Since μSOFCs operate at temperatures between 400°C and 600°C, the thermal expansion coefficient mismatch between the substrate and the PEN is a major issue. The thermal S_{th} stress in the electrolyte membrane can be written as the product of the thermal mismatch α_{film}-$\alpha_{substrate}$, the temperature variation T_{final}-$T_{initial}$ during heating, the biaxial Young modulus $Y_{film}/1-\nu_{film}$ where ν_{film} is the Poisson's coefficient of electrolyte film:

$$S_{th} = \frac{(T_{initial} - T_{final}) \cdot (\alpha_{film} - \alpha_{substrate}) \cdot Y_{film}}{1 - \nu_{film}} \tag{2.1}$$

The choice of a substrate with a thermal expansion coefficient close to the one of the electrolyte is the simplest way to reduce the thermal stresses.

During the ramping up of the cell from the ambient temperature to the temperature of operation, the thermal mismatch between the supporting wafer and the membrane itself can create buckling or even cracks in the membrane. Tang et al. [25] give the maximal temperature ramp ΔT_{crit} sustainable by a free standing membrane in function of its radius R_{mem} and its thickness h_{mem}:

$$\Delta T_{crit} = \frac{1.22}{(1+\nu_{film})(\alpha_{film} - \alpha_{substrate})} \left(\frac{h_{mem}}{R_{mem}} \right)^2 \tag{2.2}$$

From this relation, it is possible to calculate the maximal membrane radius in function of its thickness (see figure 1). For a 1μm thick YSZ membrane operating at 500°C and supported by a silicon wafer, the maximal radius 500°C is only 25 μm.

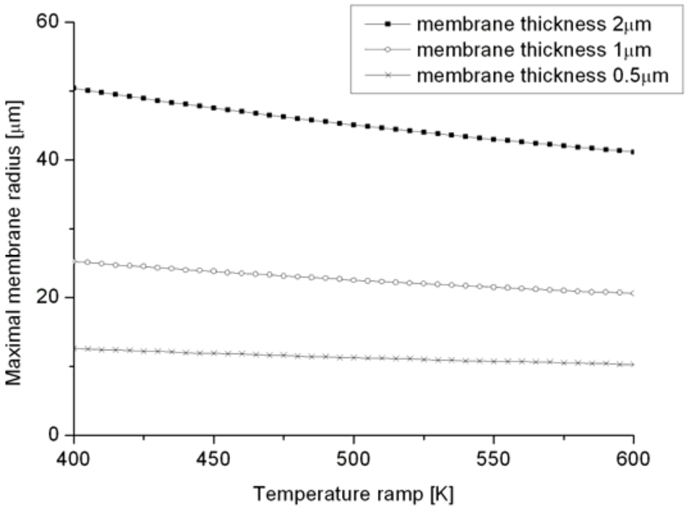

Figure 3: Maximal membrane radius for a YSZ membrane supported by a silicon wafer with the temperature ramp [25].

Because of thermal stress, μSOFCs self supporting electrolytes either YSZ of CGO membranes are limited to a sub millimeter size [26]. Since the electrolyte should remain thin to reduce the cell resistance, large self-supported membranes are almost impossible to fabricate. Interestingly the YSZ membrane of Prinz giving the spectacular results of 400 mW/cm^2 [3], should buckle very much since the critical temperature ramp (equation (2.2)) is calculated as less than 1 K with a thickness of 50 nm and an aperture of 50 µm. So we can consider as open question whether a membrane thickness far less than the critical one could also be considered as a viable approach.

The mechanical and thermal stability of MEMS thin membranes has already been solved using corrugated design [27, 28]. The use of corrugation steps, as schematically shown on figure 2, helps to improve the critical stress of failure of the membrane without reducing its radius or its thickness [25]. The gain of resistance increases with the ratio of the step height H_{step} over the membrane thickness h_{mem}.

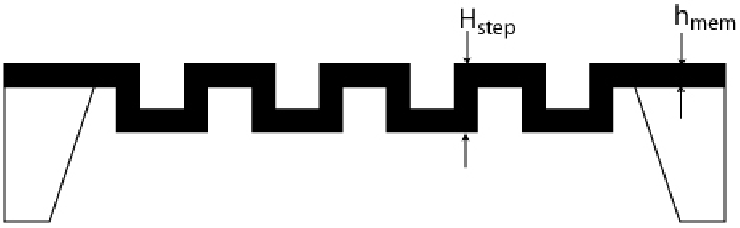

Figure 4: Schematic view of a corrugated membrane of thickness h_{mem} and with a step of corrugation H_{step}.

Nevertheless, such a design requires more complicated microfabrication process flows and, for µSOFCs, flat surfaces are more advantageous. The corrugation steps increase the diffusion path in some areas and electrolyte films deposited onto steps are much prone to form cracks. For better convenience, the membrane can be supported by a mechanical support. This part can by made of stiffeners [29] or of a porous substrate. In the second case, the porosity is obtained by using special substrates [30] or by subsequent etching of a metallic plate [31]. Furthermore special techniques are required to grow a dense thin film electrolyte on a porous substrate [32-34]. Finally the conducting properties of the support also affect the power density of the device and thus ionic or electronically conductors supports are more favorable than insulating materials such as silicon nitride [2].

2.2.2. Process induced stresses

Stresses are usually present in thin films even if they are not externally loaded. This is due to deposition conditions. These stresses directly affect different phenomena such as the adhesion, the defect concentration and even the film roughness. Residual stresses can also affect the functionality of microfabricated devices. For example, the resonant frequency of vibrating devices such as transducers [35] depends on their stress state and a gradient of stress can bend cantilevers [36].

The origin of this stress is usually divided into two parts: the thermal stress and the intrinsic stress. The thermal stress occurs when the deposition is held at high temperatures. It is due to the thermal expansion coefficients mismatch between the growing film and the substrate. During the cooling, the film expansion or shrinkage is limited by the substrate and it leads to a residual stress in the film as shown in Figure 5. This stress is also described by the equation (2.1) but the temperature of operation should be replaced by the temperature of deposition and the sign of ΔT is negative as the film is cooled and not heated.

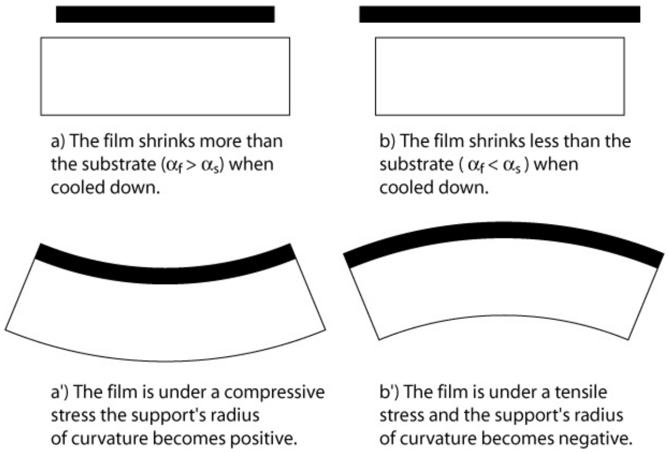

Figure 5: Stress due to cooling of the film after its deposition at high temperature onto a substrate with a different thermal expansion coefficient. A film with a higher expansion coefficient than the substrate becomes compressive (a). A film with a lower expansion coefficient than the substrate becomes tensile (b).

Apart from the thermal stresses, the deposition process can also induce intrinsic stress in the film. The intrinsic stress is due to several phenomena and is less well understood than the thermal stress. The intrinsic stress is defined as the total stress minus the thermal contribution [37]. The intrinsic stress contribution depends on the temperature of the process, the type of process and the materials it self. The thermal activation helps reducing the intrinsic stress by atomic rearrangements and it is considered that the intrinsic contribution diminishes with the increasing process temperature, thus when the thermal stress increases [37]. During sputtering, the bombardment forces some ions into the interstitial sites of the lattice. The lattice is thus denser and the clamping to the substrate creates a compressive stress [38].

In ion conducting oxides, strain and elastic modulus are related to the density of oxygen vacancies in the film [39, 40] and thus to the ionic conductivity [41]. The defect density doesn’t affect directly the stress, but some material properties strongly related to it, like the elastic modulus or the thermal expansion coefficient of YSZ [42]. In CGO thin films, fast and slow elastic modulii have been reported [43]. In this case, the intrinsic chemical stress is reduced by atomic rearrangements that are time dependent [44]. As the concentration of defects is related the environemental conditions, the chemical stress can also develop when changing the outside temperature or the oxygen pressure.

A thermal annealing reduces the intrinsic stress in the film after its deposition [45]. The temperature and the time are the most important parameters for annealing. The temperature allows atom motion by increasing the amplitude of the thermal vibrations in the crystal. The probability of moving an atom to another site increases with time.

2.2.3. Heat losses

The heat losses can be very important in μSOFCs as the PEN membrane is very thin and should cover the largest possible area. There are three ways of heat losses in μSOFCs: air convection, structure thermal conduction and radiation [25].

The convection losses are due to heat transfer from the PEN to the surroundings atmosphere. For a circular membrane of radius R_{mem}, the heat losses by laminar air flow convection Q_a may be expressed as:

$$Q_a = 1.27 \Delta T^{5/4} R_{mem}{}^{7/4} \tag{2.3}$$

The properties of the fluid are used to obtain equation (2.3) are given in [46]. Convection losses almost change linearly with the thin film area ($R_{mem}{}^2$) and the temperature difference ΔT with the surroundings.

The conduction losses Q_h are due to the difference of temperature between the centre of the membrane T_0 and its border T_b, with $T_0 > T_b$. This difference is due to the cooling of the support substrate. The whole losses by thermal conduction for a circular membrane of thickness h_{mem} and thermal conductivity k_{mem} is given by [47]:

$$Q_h = \pi k_{mem} (T_0 - T_b) h_{mem} \tag{2.4}$$

The conduction losses are linearly dependant of the film thickness, as heat is conducted through it to the support.

It is assumed that there is a radial distribution of the temperature over the circular surface of the membrane of radius R_{mem}. T_0 is the temperature in the centre of the membrane and T_b at its border. According to the Stephan-Boltzmann law, heat losses Q_e can be expressed as function of the emissivity of the membrane ε_{mem} (0.4 for zirconia [48]) and Boltzmann constant ($\sigma_B = 5.67x10^{-8}$ W/m^2K^4):

$$Q_e = \frac{\varepsilon_{mem} \sigma_B \pi R^2}{5} (T_0^4 + T_0^3 T_b + T_0^2 T_b^2 + T_0 T_b^3 + T_b^4) \tag{2.5}$$

The radiation losses are proportional to the surface of the membrane.

The figure 9 summarizes these different effects with the size of the membrane. For membranes with a small radius, conduction losses are the most important but they are reduced as the size of the membrane increases. It is due to the fact that the heat is released at the perimeter of the membrane. The convection and the radiation losses increase with the membrane radius because heat is exchanged at the surface of the membrane. In cell normal operation conditions, the conduction losses into the gases (the air the fuel) are more important than the radiation losses. The conduction losses can be reduced by pre-heating the gases before they reach the membrane and for smaller fluxes. The heat loss by natural convection through the ambient air can be reduced by suitable packaging, such as vacuum packaging.

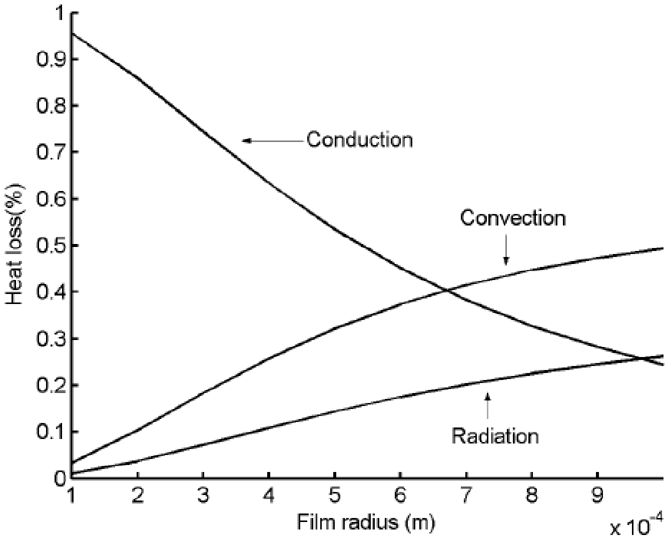

Figure 6: Heat losses versus film radius for a circular membrane with a difference of 350 °C between its centre and its border [47].

2.3. Approach of this work

It is sought to achieve large and thin ceramic membranes by adding a metallic supporting structure. Ideally, the metal should have the same expansion coefficient as the ceramic membrane. Nickel with 10 ppm/K differs only by 1 ppm/K from YSZ and appears to be a good choice, also to assume part of the electrode structure on the anode side. Such a nickel grid would solve the buckling problem at least in the interior of the membrane where the thermal expansion of the nickel grid is dominating the mechanical behaviour. According to equation (2.2) much higher critical temperatures are obtained. For example, if the electrolyte is 700 nm thick, a nickel grid with apertures of 30 μm allows for maximal temperature differences of 520 °C before buckling of the ceramic layer. It is planned to focus the stress due to mismatch with silicon into the nickel structure.

All the PEN elements are deposited by sputtering which is good for research as well as for upscaling to industrial fabrication. The sputtering method also permits the deposition of different type of microstructures, for example a porous composite anode and a dense electrolyte.

We also will test the conductivity of the electrolyte and electrode thin films as a function of temperature and in different gas atmospheres to find out if the sputtered films can be applied to a SOFC system. We also will assess the thermal stress in the membrane to improve designs.

Finally, we will test the fabricated cells in operation conditions by impedance spectroscopy, open circuit voltage and I-V measurements. We will also concentrate on the lifetime properties of the cell and especially on the thermal oxidation of the nickel grid.

2.4. References

1. Barnett, S.A., *A new solid oxide fuel cell design based on thin film electrolytes.* Energy, 1990. **15**(1): p. 1-9.
2. Jankowski, A.F., et al. *Micro-Fabricated Thin-Film Fuel Cells for Portable Power Requirements*. in *Proceedings of the Materials Research Symposium*. 2002.
3. Huang, H., et al., *High-performance ultrathin solid oxide fuel cells for low-temperature operation.* Journal of the Electrochemical Society, 2007. **154**(1): p. B20-B24.
4. Bieberle-Hütter, A., et al., *A micro-solid oxide fuel cell system as battery replacement.* Journal of Power Sources, 2008. **177**(123-130).
5. Shao, Z., et al., *A thermally self-sustained micro solid-oxide fuel cell stack with high power density.* Nature, 2005. **435**(9): p. 795-798.
6. Yu, J., et al., *Fabrication of miniature silicon wafer fuel cells with improved performance.* Journal of Power Sources, 2003. **124**: p. 40-46.
7. Yu, J., et al., *Fabrication of a miniature twin-fuel-cell on silicon wafer.* Electrochemica Acta, 2003. **48**: p. 1537-1541.
8. Lee, S.J., et al., *Design and fabrication of a micro fuel cell array with ‘‘flip-flop’’ interconnection.* Journal of Power Sources, 2002. **112**: p. 410-418.
9. Shah, K., W.C. Shin, and R.S. Besser, *A PDMS micro proton exchange membrane fuel cell by conventional and non-conventional microfabrication techniques.* Sensors and Actuators B, 2004. **97**: p. 157-167.
10. Hsieh, S.-S., et al., *A novel design and microfabrication for a micro PEMFC.* Microsystem Technologies, 2004. **10**(121-126).
11. *PolyFuel's ultra-thin membrane claims record.* Fuel Cells Bulletin, 2007. **1**: p. 8.
12. Yao, S.-C., et al., *Micro-electro-mechanical systems (MEMS)-based micro-scale direct methanol fuel cell development.* Energy, 2006. **31**: p. 636-649.
13. Blum, A., et al., *Water-neutral micro direct-methanol fuel cell (DMFC) for portable applications.* Journal of Power Sources, 2003. **117**: p. 22-25.
14. Miesse, C.M., et al., *Direct formic acid fuel cell portable power system for the operation of a laptop computer.* Journal of Power Sources, 2006. **162**(1): p. 532-540.
15. Chu, K.-L., et al., *A Nanoporous Silicon Membrane Electrode Assembly for On-Chip Micro Fuel Cell Applications.* Journal of Microelectromechanical Systems, 2006. **15**(3): p. 671-677.
16. Zhu, Y., S.Y. Ha, and R.I. Masel, *High power density direct formic acid fuel cells.* Journal of Power Sources, 2004. **130**: p. 8-14.

17. Nikbin, D., *Micro SOFCs: why small is beautiful.* The Fuel Cell Review, 2006. **(April/May)**(21-24).
18. Hui, S., et al., *Metal-supported solid oxide fuel cell operated at 400-600 °C.* Journal Power Sources, 2007. **167**.
19. Fleig, J., H.L. Tuller, and J. Maier, *Electrodes and electrolytes in micro-SOFCs: a discussion of geometrical constraints.* Solid State Ionics, 2004. **174**: p. 261-270.
20. Perry, M.L. and T.F. Fuller, *A historical perspective of fuel cell technology in the 20th century.* Journal of the Electrochemical Society, 2002. **149**(7): p. S59-S67.
21. Ormerod, R.M., *Solid oxide fuel cells.* Chemical Society Review, 2002. **32**: p. 17-28.
22. Kleinlogel, C.M., *Cathode supported thin electrolytes and nano sized ceria solid solutions for solid oxide fuel cells*, in *Materials Science*. 1999, Swiss Federal Institute of Technology: Zurich.
23. Buergler, B.E., et al., *From macro- to micro-single chamber solid oxide fuel cell.* Journal of Power Sources, 2007. **171**: p. 310-320.
24. Lee, S.J., et al., *Design and fabrication of a micro fuel cell array with 'flip-flop' interconnection.* Journal of Power Sources, 2002. **112**(410-418).
25. Tang, Y., et al., *Design consideration of micro thin film solid-oxide fuel cells.* Journal of Micromechanics and Microengineering, 2005. **15**(9): p. S185-S192.
26. Baertsch, C.D., et al., *Fabrication and structural characterization of self-supporting electrolyte membranes for a micro solid-oxide fuel cell.* Journal of Materials Research, 2004. **19**(9): p. 2604-2615.
27. Hammer, R., *Solving the “stencil” problem in vacuum deposition masks using rib-supported structures.* Journal of Vacuum Science and Technology, 1977. **14**(5): p. 1208-1210.
28. Van den Boogaart, M.A.F., et al., *Corrugated membranes for improved pattern definition with micro/nanostencil lithography.* Sensors and Actuators A, 2006. **130-131**(Spec. iss.): p. 568-574.
29. Srikar, V.T., et al., *Structural design considerations for micromachined solide-oxide fuel cells.* Journal of Power Sources, 2004. **125**: p. 62-69.
30. Kang, S., et al., *Thin-film solid oxide fuel cells on porous nickel substrates with multistage nanohole array.* Journal of the Electrochemical Society, 2006. **153**(3): p. A554-A559.
31. Chen, L., et al., *High temperature electrical conductivity of epitaxial Gd-doped CeO2 thin films.* Solid State Ionics, 2004. **175**: p. 103-106.
32. Mineshige, A., et al., *Vapor-phase deposition for dense CeO2 film growth on porous substrates.* Journal of Electrochemical Society, 2006. **153**(6): p. A975-A981.
33. Park, Y.-I., et al., *Thin-Film SOFCs Using Gastight YSZ Thin Films on Nanoporous Substrates.* Journal of The Electrochemical Society, 2006. **153**(2): p. A431-A436.

34. Yoo, Y., *Fabrication and characterization of thin film electrolytes deposited by RF magnetron sputtering for low temperature solid oxide fuel cells.* Journal of Power Sources, 2006. **160**: p. 202-206.
35. Lee, S., et al., *Stress influences on the ultrasonic tansducers.* Sensors and Actuators A, 2004. **119**(2): p. 405-411.
36. Laconte, J., et al., *Thin films stress extraction using micromachined structures and wafer curvature measurements.* Microelectronic Engineering, 2004. **76**(1-4): p. 219-226.
37. Thornton, J.A. and D.W. Hoffman, *Stress-related effects in thin films.* Thin Solid Films, 1989. **171**(1): p. 5-31.
38. Jansen, F., *Plasma-enhanced chemical vapor deposition*, ed. A. Monographie. 1998.
39. Greenberg, M., et al., *Elasticity of solids with a large concentration of point defects.* Advanced Functional Materials, 2006. **16**: p. 48-52.
40. Wang, Y., et al., *The effect of oxygen vacancy concentration on the elastic modulus of florite-structured oxides.* Solid State Ionics, 2007. **178**: p. 53-58.
41. Arima, T., et al., *Molecular dynamics simulation of yttria-stabilized zirconia between 300 and 2000 K.* Journal of Molecular Liquids, 2004. **113**: p. 67-73.
42. Terblanche, S.P., *Thermal-expansion coefficients of yttria.stabilized cubic zirconias.* Journal of Applied Crystallography, 1989. **22**: p. 283-284.
43. Lubomirsky, I., *Stress adaptation in ceramic thin films.* Physical Chemistry Chemical Physics, 2007. **9**: p. 3701-3710.
44. Lubomirsky, I., *Mechanical properties and defect chemistry.* Solid State Ionics, 2006. **177**: p. 1639-1642.
45. Bilek, M.M.M. and D.R. McKenzie, *A comprenhensive model of stress generation and relief processes in thin films deposited with energetic ions.* Surface Coating Technology, 2006. **200**(4345-4354).
46. Hewitt, G.F., G.L. Shires, and T.R. Bott, *Process heat transfer*, ed. C. Press. 1993, FL.
47. Incorpera, F.P. and D.P. Dewitt, *Fundamentals of heat and mass transfer*, ed. Wiley. 1996, New York.
48. Sully, A.H., E.A. Brand, and R.B. Waterhouse, *Some measurements of the total emissivity of metals and pure refractory oxides and the variation of emissivity with temperature.* Journal of Applied Physics, 1952. **3**(97-101).

Thin film deposition and characterization

3.1. Thin film deposition and characterization

3.1.1. Thin film sputtering

3.1.2. Stress measurement in thin films

3.1.3. Electrical characterization of thin films
  3.1.3.1. DC conductivity measurements in furnace with controlled atmosphere
  3.1.3.2. DC conductivity measurements on a hot plate
  3.1.3.3. Impedance spectroscopy measurements
  3.1.3.4. Arrhenius plot of the ionic conductivity

3.2. YSZ thin film electrolyte

3.2.1. Growth and microstructure characterization of single layer YSZ thin films

3.2.2. Growth and microstructure characterization of multilayer YSZ films

3.2.3. Stress in (111) YSZ thin films

3.2.4. Electrical characterization of multilayer and single layer YSZ films

3.3. CGO thin film electrolyte

3.3.1. Growth conditions and microstructure characterization

3.3.2. Stress in the CGO thin film

3.3.3. Electrical characterization of CGO thin films

3.4. LSCO thin film cathode

3.4.1. Growth conditions and microstructure characterization

3.4.2. Electrical characterization

3.5. Ni-CGO composite thin films

3.5.1. Study of the morphology of porous composite nickel-CGO thin films

3.5.2. Study of the composition of porous composite CGO-Ni thin films

3.5.3. Electrical characterization of the Ni-CGO thin films

3.6. Porous platinum electrodes

3.6.1. Growth conditions and microstructure characterization

3.7. Summary

3.8. References

3.1. Thin film deposition and characterization

All the thin films discussed in this chapter have been deposited by reactive magnetron sputtering. The first paragraph of this chapter will describe the specific tool used to sputter the films. Then, the used deposition processes will be explained. Finally, the characterization results of these films will be reported and their properties discussed.

3.1.1. Thin film sputtering

During sputtering, a target of a given material is bombarded with positive ions emitted by a noble gas (argon) discharge between an anode and the target mounted on the cathode. The discharge is obtained by applying a high electrical field between the anode and the cathode, while the substrate and the chamber are usually close to the anode potential, the latter being usually grounded. The deposition of metals works well by using a DC source for powering the cathode. In the case of a dielectric target, the use of a radio frequency (RF) source is required. Higher sputtering efficiency and deposition rates are obtained with magnetron sources. They possess a magnetic field to confine the secondary electrons ejected from the target, thus increasing collision probability with neutral atoms and so increase plasma density. Important parameters for sputtering are: the applied voltage (400-1000 V), the temperature of the substrate, the distance target-substrate, the sputter gas pressure and eventually the applied electrical bias on the substrate.

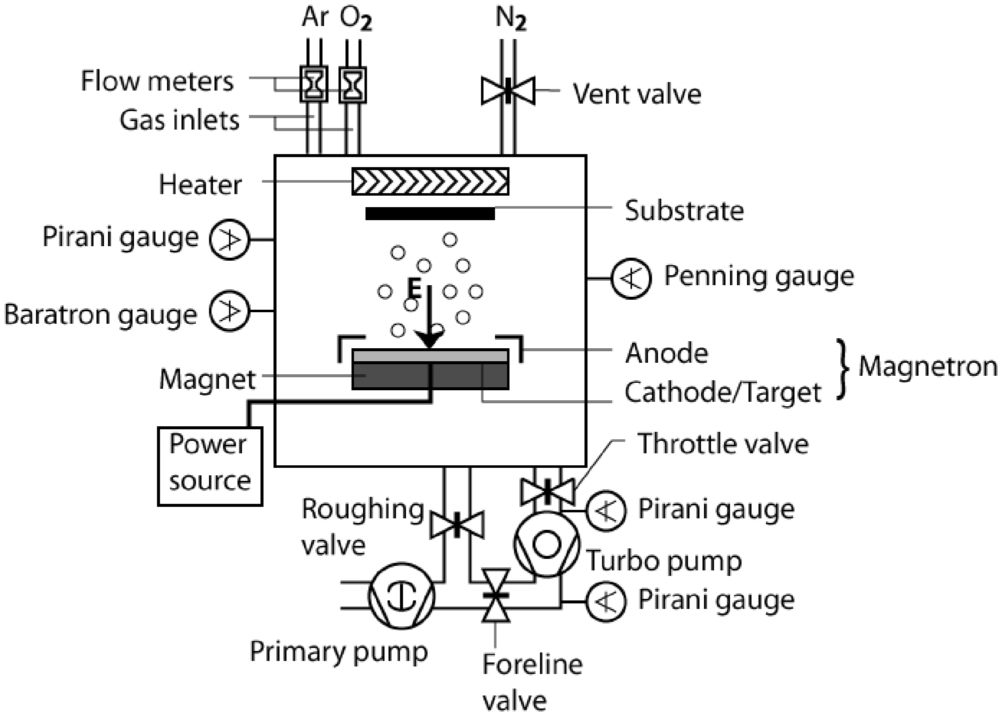

Figure 1: Schematic representation of a typical sputtering system. The parameters used for the different films deposition are summarized in paragraphs 3.2 to 3.6.

By adding a reactive gas in the chamber such as oxygen or nitrogen it is possible to deposit compounds as oxides or nitrides from a metallic target. The conditions required to yield compounds in place of metallic films depend on the flow rate of reactive gas Q_r added to the non reactive gas (Ar) at P_0 and the total pressure in the chamber P [1]. Without sputtering process, the pressure varies linearly with the flow of gas (dotted line in Figure 2) for a constant pumping speed. With working sputter source, the pressure first remains stable and equal to P_0, because the reactive gas is incorporated into the film and thus removed from the gas phase. When the flow Q_r reaches Q_i*, the pressure jumps to P_1, indicating that the target surface is fully oxidized (to use the example of oxygen gas), resulting in a drop of the sputtering yield. If no reactive sputtering took place, the pressure would reach a higher value of P_3. Once the equilibrium pressure P_1 is achieved, a change of Q_r causes a linear increase or decrease of P. If the flow decrease below $Q(0)$, P reaches the initial pressure again. The hysteretic behaviour represents two stable states with a rapid transition between them. Along the line A, the concentration of reacted material increases with Q_r. At Q^*_r, the change from state A to B is due to the drop of the sputter rate when the target surface reaches a critical value of oxide coverage. Due to the rate drop, target and film are suddenly pumping less reactive gas, the pressure increases and saturation of the reaction is reached, usually at stoichiometry or slightly above. State B is maintained even if the reactive gas flow is reduced. When reaching $Q_i(0)$ the system falls back into state A. This hysteresis can be monitored by measuring the cathode voltage because ion-induced secondary electron emission is higher for compounds than for metals. According to Ohm’s law, the plasma impendency is lower in the state B than in the state A. Thus a high cathode voltage indicates the deposition of a metallic film and a voltage drop indicates the deposition of a compound. An example of this hysteretic behaviour is given in the Figure 2.

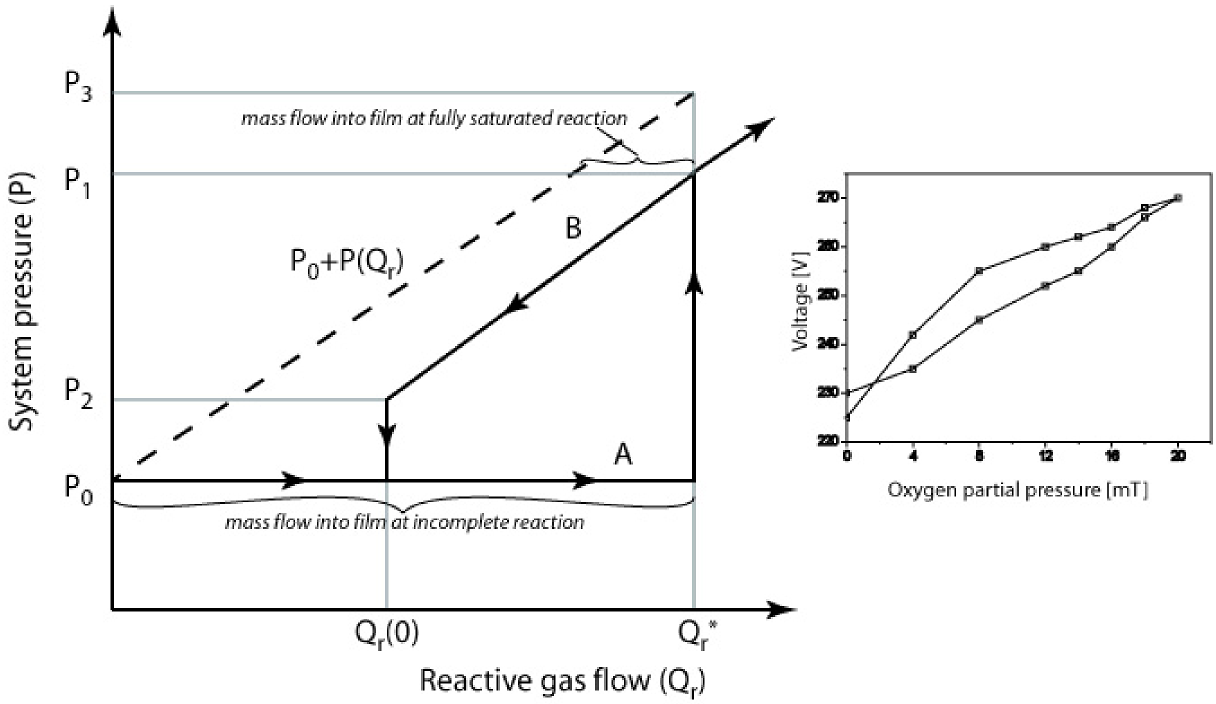

Figure 2: System pressure *P* according to the reactive gas flow Q_r during reactive sputtering. Without sputter process, $P(Q_r)$ curve is hysteretic. Line A is the result of strong pumping of reactive gas by the fast growing film below the saturation is reached. Line B is the result of reached saturation leading to a low deposition rate. Right: Hysteretic behaviour of the voltage versus the oxygen partial pressure during sputtering of YSZ (total pressure 20 mT)

Sputtering is a very popular technique for the study of all PEN elements (anode, electrolyte and cathode). Films obtained by this method are usually dense with columnar microstructure and are thus very good candidates for electrolytes. Yttria stabilized zirconia YSZ [2], $La_2Mo_2O_9$ [3], Sm-doped ceria SDC and scandia stabilized zirconia ScSZ [4] have been deposited by this method. Dense and thick (2-12 µm) electrolytes [5] and even the whole stack of layers [6] can also be obtained on porous substrates. Electrodes such as Ni-YSZ [7] and can also be sputter deposited and it's even possible to obtain porous films on dense layers [6].

In this work we used a Nordiko sputter system having a single chamber containing four magnetrons and a 360° rotating substrate holder (see Figure 3). Two DC generators and one RF generator can be operated simultaneously for the cosputtering from maximal three targets. The substrate holder can either stop in front of one of the targets or rotate over all of them at a given speed (1 to 10 rpm). Thus it is possible to deposit consecutive layers or a compound of the different target materials. This system has for instance been used to deposit $PbZr_xTi_{1-x}O_3$ by co-sputtering from titanium, zircon and lead targets [8]. Two DC and one RF sources are used to apply voltage on the different targets. The RF source is used to sputter from dielectric targets.

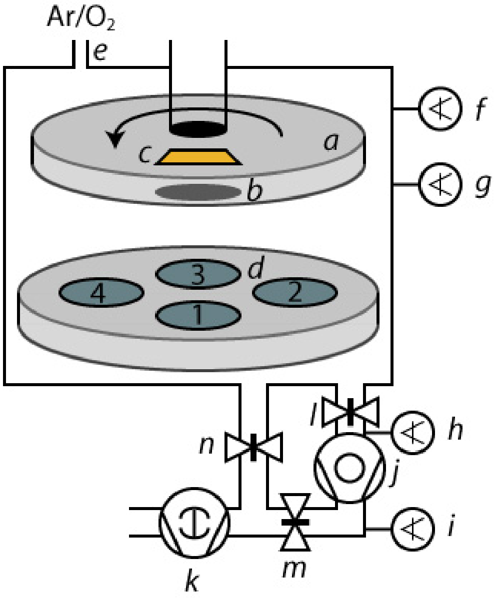

Figure 3: Configuration of the reactive magnetron sputtering tool Nordiko a) Rotating substrate holder, b) 4"substrate, c) heating lamps, d) 4 different targets, e) entry for process gases Ar and O_2, f) Baratron gauge used during process, g) Pirani gauge used during pumping, h) Pirani gauge, i) Pirani gauge, j) turbo pump, k) primary pump, l) high-vacuum valve, m) foreline valve, n) roughing valve. The four power generators for targets (2 DC and 1 RF) and substrate bias (1 RF) are not shown on this scheme.

The substrate is heated indirectly by the radiation of lamps and can reach a nominal temperature of 800°C. The distance between substrate and targets can be varied between 1 and 10 cm. The pressure in the chamber is monitored by a Baratron gauge controlling the aperture of a gate-valve. During the process, the fluxes of argon and of oxygen are fixed between 1 and 60 sccm for Ar and 1 and 20 sccm for O_2 and the pressure is controlled by the aperture of the gate-valve. The working pressure can by varied between 1 and 100 mTorr. The chamber base pressure is approximately of $5x10^{-4}$ mbar.

3.1.2. Stress measurement in thin films

The stress in the deposited thin films is evaluated by a Tencor FLX-2900 apparatus. It measures the radius of curvature r of the substrate, derived from the deflection angle θ of a laser beam hitting the surface of the substrate. The laser source and the detector are mounted on a single module that scans along the substrate length.

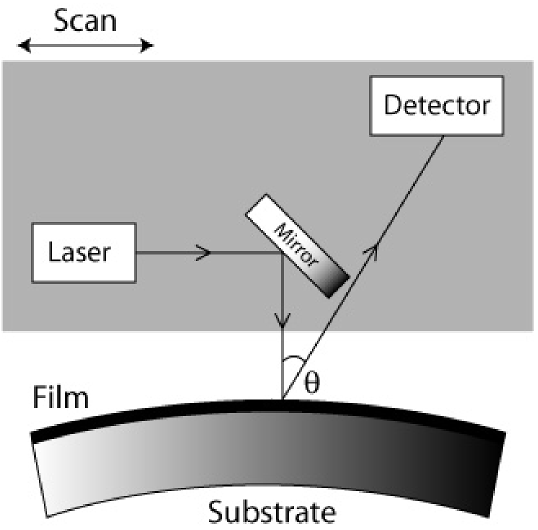

Figure 4: Schematic view of the Tencor Flex 2900 stress gauge

The following equation is used to determine the film stress S depending to the Young modulus $Y_{substrate}$, Poisson coefficient $\nu_{substrate}$ and thickness $t_{substrate}$ of the substrate, the film thickness t_{film} and the radii of curvature before r_1 and after deposition r_2:

$$S = \frac{Y_{substrate} t_{substrate}^2}{6(1-\nu_{substrate}) t_{film}} \left[\frac{1}{r_2} - \frac{1}{r_1} \right] \tag{3.1}$$

For silicon (100) wafers and 4 x 1 cm^2 samples the following parameters were used:

Table 1: Mechanical properties of the silicon (100) substrates

Young modulus [GPa]	Poisson coefficient [-]	Thickness [µm]
180.5	0.2	380 or 525

When several films of thickness t_i are deposited on the substrate, the change of the curvature $\Delta(1/r)$ is given by the following law:

$$\Delta\left(\frac{1}{r}\right) = \frac{\sum_i t_i S_i}{\frac{Y_{substrate}}{1-\nu_{substrate}} t_{substrate}^2} \tag{3.2}$$

In this case, the total stress S_{tot} is by the sum of the products of the films thicknesses t_i multiplied by their corresponding stress S_i:

$$S_{tot} = \sum_i S_i \times t_i \qquad (3.3)$$

Tencor FLX-2900 includes an oven and allows measuring the stress at temperatures from 20°C up to 900°C at a given rate controlled by a thermocouple. It is also possible to undergo experiments under a given gas flux of argon or oxygen but the chamber is not gas tight and the pressure cannot be controlled.

3.1.3. Electrical characterization of thin films

3.1.3.1. DC conductivity measurements in furnace with controlled atmosphere

DC 4 points conductivity measurements were performed in a tubular furnace under a controlled atmosphere. The sample was place on a sample holder shown in the Figure 5:

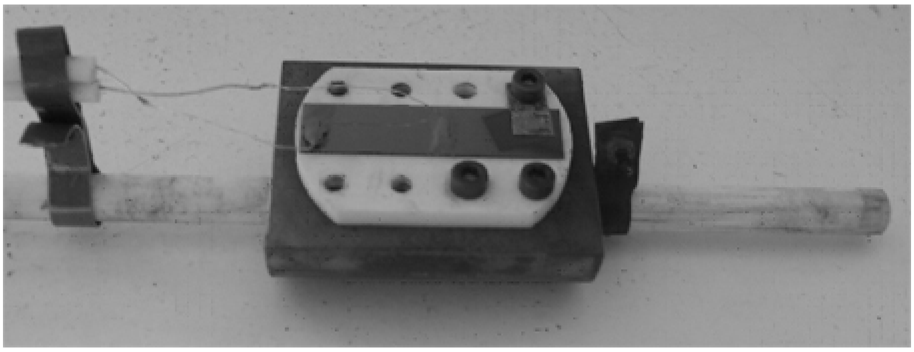

Figure 5: Sample holder for conductivity measurements in the furnace

Two platinum electrodes with dimensions of approximately 10 x 5 mm^2 were sputtered on the sample to serve as electrical contacts. Four Pt wires (from Goodfellow), with a diameter of 0.5 mm, were stuck to the electrodes with a commercial Pt paste (Heraeus LPA 88/11 S). The 4 point resistance of the sample was measured with a digital multimeter (Hewlett Packard 34401A). The atmosphere in the furnace was set by controlling the flows of argon, oxygen and hydrogen with 3 flowmeters (MKS 1179) and a flow controller (MKS 647B). Most of the experiments were performed under pure oxygen or nitrogen. A Pt/PtRh thermocouple was placed in the furnace near the sample holder. A schematic view of the experimental setup is shown in the Figure 6:

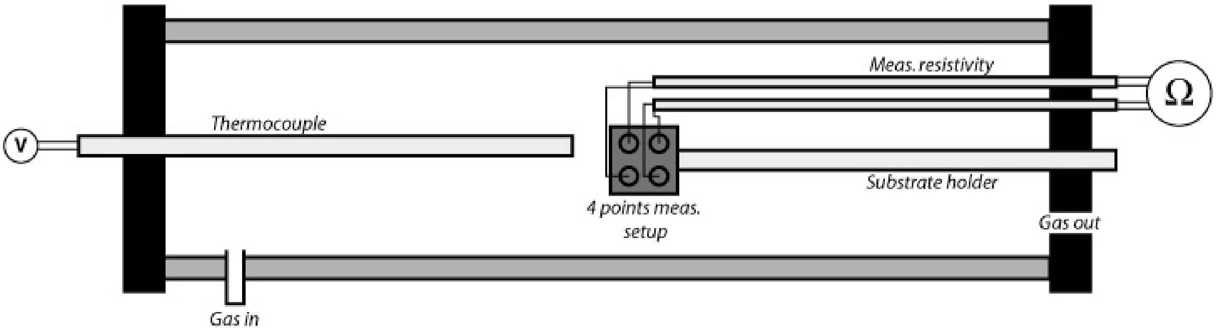

Figure 6: Schematic view of the DC conductivity measurement in the furnace.

The in-plane conductivity of the film was calculated from the measured 4 points resistance R_4 and the dimensions (length L, thickness t and width w) of the sample as seen in the Figure 7:

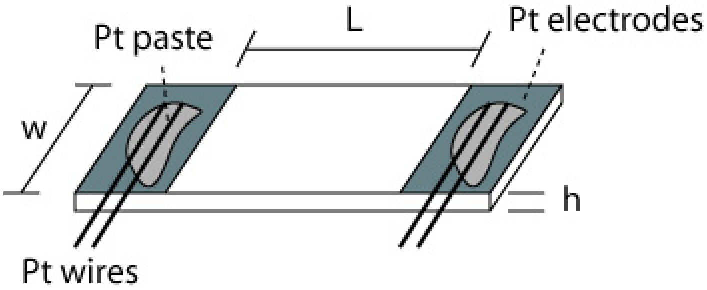

Figure 7: Schematic view of the sample dimensions and electrical connections.

The in-plane conductivity of the sample σ is simply given by:

$$\sigma = \frac{1}{R_4} \frac{L}{w \cdot t} \tag{3.4}$$

3.1.3.2. DC conductivity measurements on a hot plate

The tested samples are in the form of an electrical capacitor with Pt top and bottom electrodes. The size of the capacitor is determined by the surface of the top electrode of diameter *d*. A schematic view of the sample with its relevant dimensions is given in the Figure 8:

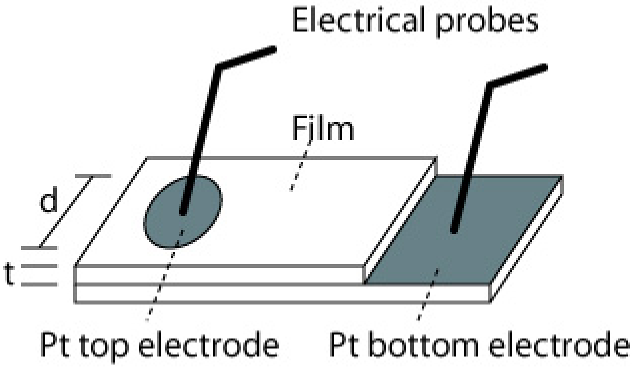

Figure 8: Schematic view of the sample dimensions and electrical connections

The measurements are made by using an impedance analyzer (Hewlett Packard 4194A). It measures the capacity *C* in Farad and the losses *tan*δ at different frequencies (100Hz to 10MHz). The experimental setup is also composed of a hot plate capable of ramping up to 520°C. A Pt/PtRh thermocouple is placed on the hot plate near the sample. Two tungsten probes are used to measure the capacity and the losses *tan*δ between the top and the bottom electrodes. The experience is held in air. The admittance *Y* of the film can be written in a complex form as:

$$Y = \frac{1}{R_{//}} + j\omega C = j\omega C(1 - j\frac{1}{R_{//}\omega C}) \tag{3.5}$$

The total parallel resistance $R_{//}$ of the film capacity is the imaginary part of the capacity and is related to the pulsation ω by the following equation:

$$R_{//} = \frac{1}{\omega C \tan\delta} \tag{3.6}$$

If the loss tangent is entirely due to leakage or conduction, the film conductivity σ is the inverse of $R_{//}$ multiplied by the ratio of the film thickness *t* divided by the capacitor area $\pi d^2/4$:

$$\sigma = \frac{{}^{4t}\!/_{\pi \cdot d^2}}{R_{//}} = \frac{4t \cdot \omega \cdot C \tan\delta}{\pi \cdot d^2} \tag{3.7}$$

3.1.3.3. Impedance spectroscopy measurements

The samples for impedance spectroscopy have the shape of a capacitor with the same dimensions as the ones described in the paragraph 3.1.3.2. The impedance spectra are measured with an HP 4194A Impedance Analyzer from 100 Hz to 10MHz or with HP4284A from 20 Hz to 1 MHz. The analyzer measures the real and imaginary parts of the electrical impedance Z for a given range of frequencies or pulsations ω. The obtained data are shown on a Nyquist plot with *Re(Z)* as x-axis and *–Im(Z)* as y-axis. Each point of the Nyquist plot corresponds to a given value of ω. The resistance of the film was obtained for the impedance spectra by fitting the curves using a resistance R_s in series with a capacity C and a resistance $R_{//}$ in parallel. The total complex impedance of this circuit Z is equal to:

$$Z = R_s + \frac{1}{j\omega C + {}^{1}\!/\!_{R_{//}}} \tag{3.8}$$

In the limits of infinite and zero pulsation ω, the impedance assumes the following values:

$$\begin{aligned} \lim_{\omega \to \infty} Z &= R_s \\ \lim_{\omega \to 0} Z &= R_s + R_{//} \end{aligned} \tag{3.9}$$

Between these two extremes, the impedance curves describes a semicircle in the *(-Im(Z), Re(Z))* plane, as shown in the Figure 9:

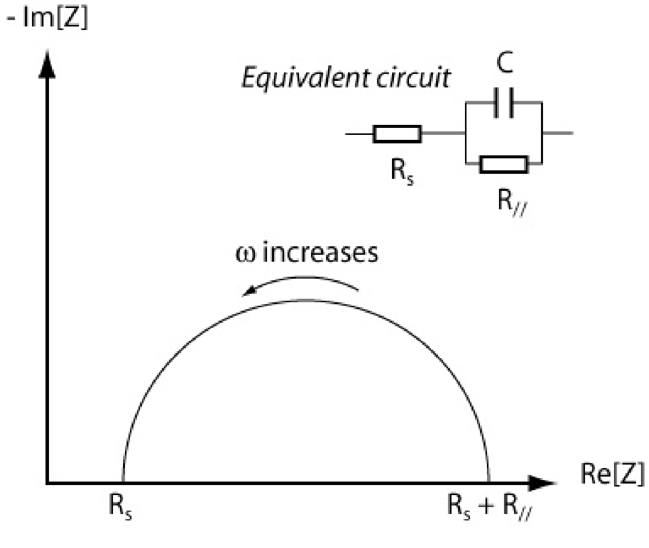

Figure 9: Schematic view of the plot of the real and imaginary part of the equivalent circuit impedance

Finally, the film conductivity σ is obtained from the sample geometry (electrode diameter d, and thickness t) and measured resistance $R_{//}$ by means of the Equation (3.10):

$$\sigma = \frac{1}{R_{//}} \frac{4t}{\pi \cdot d^2} \tag{3.10}$$

3.1.3.4. Arrhenius plot of the ionic conductivity

The ionic conduction is a diffusion process and thus requires thermal activation. The diffusion constant D relating current to concentration gradient has the form:

$$D = D_0 \cdot e^{-\frac{E_a}{kT}} \tag{3.11}$$

Where k is the the Boltzmann constant *k* (1.38 x 10^{-23} J/K or 8.61 x 10^{-5} eV/K), *T* the temperature (in K) and E_a the activation energy (in eV). At infinite temperature, the diffusion constant is limited to D_0 (in m^2/s):

The ionic conductivity σ is given by [9]:

$$\sigma = A \frac{1}{T} e^{-\frac{E_a}{kT}} \tag{3.12}$$

Where *A* is constant with the temperature and depends on *k*, D_0, the carrier density n (in 1/mol), the charge of the carriers *z* and the charge of the electron *e* (1.602 x 10^{-19} C/mol):

$$A = \frac{n \cdot z^2 \cdot e^2 \cdot D_0}{k} \tag{3.13}$$

E_a can be directly derived from the slope of the Arrehnius plot, i.e. from the slope $-E_a/k$, of $ln(\sigma T)$ vs *1/T*.

3.2. YSZ thin film electrolyte

Yttria stabilized zirconia thin films containing 8% mol. Y_2O_3, referred to as 8YSZ, were deposited by reactive magnetron sputtering. The goal was to develop dense and columnar films as well as multilayer films with interrupted columns. Optimal parameters for the growth of both types of films were found.

3.2.1. Growth and microstructure characterization of single layer YSZ thin films

8YSZ films have been deposited by reactive magnetron sputtering onto (100)-oriented, 100 mm diameter silicon wafers of 0.1 to 100 Ωcm resistivity. The wafers were cut into 4 x 1 cm2 pieces for characterization by electron microscopy, X-ray diffraction (XRD), electrical measurements or thermal stress analysis. The full wafer size was used for the fabrication of µSOFCs, which will be treated in Chapter 5. If required, the wafers were oxidized in a furnace to obtain 0.5 to 1.5 µm thick layers. Pt electrodes were deposited by DC sputtering under a Ar flow of 15 sccm and a power of 1000 W at 300°C. They were 100 nm thick and exhibited a (111) texture.

8YSZ was deposited from a commercial zirconium-yttrium alloy target of composition 16/84 purchased from Kurt J. Lesker. The purity amounted to 99.9%. Target diameter and thickness amounted to 10 cm and ¼", respectively. . The metallic target has the advantages of being a better thermal conductor and more ductile than a ceramic, thus it is less sensitive to cracking than a ceramic target, and allows for higher sputter powers. In DC mode operation the plasma was instable and some sparks appeared. Sparking always produces particles, and bears the risk to get pinholes into the film. We thus changed to RF power supply, even though the deposition rate was smaller.

The deposition conditions for the 8YSZ films are reported in Table 2:

Table 2: Deposition conditions for the YSZ thin films of type A.

Pressure [mT]	**Ar flow [sccm]**	**O_2 flow [sccm]**	**RF power [W]**	**RF voltage [V]**	**Temperature [°C]**	**Rate [nm/min]**	**Dist. T-S. [mm]**
5	10	10	200	200	500	2.1	100

After deposition at 500°C, the samples were cooled down during 3 hours in the chamber under 80 mT of pure oxygen (20 sccm flow).

The morphology and orientation of the obtained thin YSZ films were investigated by using scanning electron microscopy SEM (Zeiss LEO 1550) and X-ray diffraction (Kristalloflex 805 Siemens, with Cu Kα radiation).

As seen in Figure 3, the film has a columnar microstructure with a grain width of approximately 50-100 nm. Hence, most of the grain boundaries are crossing the film slab on the shortest way. The grain boundary density δ_{gb} has been calculated using the equation (3.14) with the assumption that the grains have a circular base of diameter d. For d equals to 75 nm, the density is approximately of 50 µm^{-1}.

$$\delta_{gb} = \frac{\pi d_g}{\pi \left(\frac{d_g}{2} \right)^2} \tag{3.14}$$

Albeit the film is very dense, this high density of grain boundary per surface turned out to be very critical for electronic leakage and H_2 permeability across the layer. The substrate (amorphous SiO_2, {111}-platinum or {100}-silicon) does not affect the morphology of the film. In all cases, X-ray diffraction patterns revealed higly {111}-textured films {see Figure 11 for the case of YSZ grown on thermal oxide). It appears that the (111)-plane of the cubic face-centred fluorite structure nucleates more easily, as it is the case for all fcc metals.

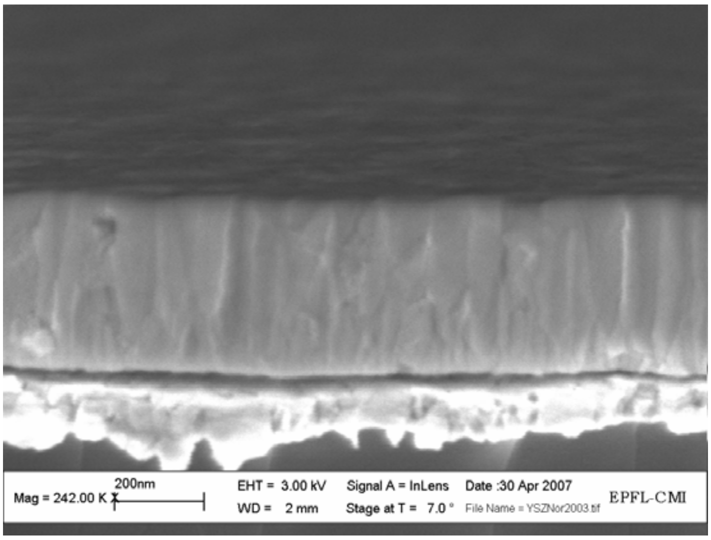

Figure 10: SEM cross-section of a 500 nm thick film of YSZ deposited onto a Pt layer (100 nm).

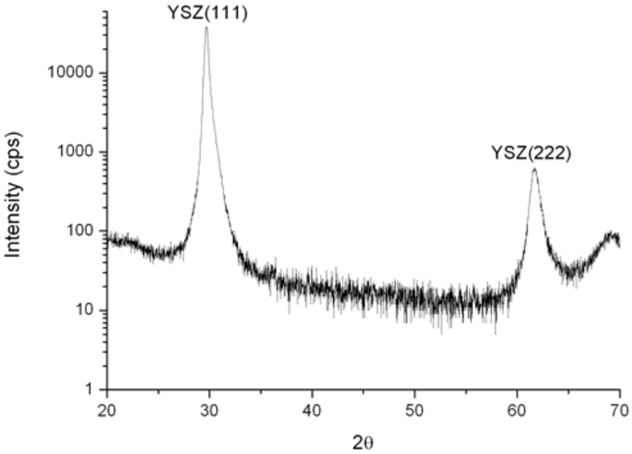

Figure 11: X-ray diffraction pattern of a 300nm thick YSZ deposited on amorphous SiO_2.

3.2.2. Growth and microstructure characterization of multilayer YSZ films

Multilayer YSZ films were deposited in sequence from the same target as reported in paragraph 3.2.1. Rudell et al. have shown experimentally that it was possible to interrupt zirconia film growth and to obtain a stack of layers with different microstructures and orientations [10]. The multilayer films were deposited in sequence with a different set of conditions for each step. YSZ films of type A were sputtered with conditions as in paragraph 3.2.1 and Table 2. Films of type B were deposited while applying a substrate bias and at room temperature as described in Table 3.

Table 3: Deposition conditions for YSZ thin films of type B.

Press. [mT]	**Ar flow** [sccm]	**O_2 flow** [sccm]	**RF power** [W]	**RF voltage** [V]	**Subst. biais** [W]/[V]	**Temp.** [°C]	**Rate** [nm/min]	**Dist. T-S.** [mm]
5	10	10	200	200	100/80?	25	2.8	100

Stacks of two or three layers alternating A and B types were deposited on small silicon samples and 4" wafers (as described in paragraph 3.2.1).

The X-ray diffraction pattern obtained after the deposition of the A-type layer shows that it is mainly (111) oriented as reported in paragraph 3.2.1. After the sputtering of the B-type layer, the XRD pattern shows a small (200) peak (Figure 12). This (200) peak obviously belongs to the 2nd layer as the recrystallizsation of the first layer can be excluded for a room temperature deposition. The smaller intensity of the (200) peak compared to the (111) is due to the smaller grain size of the B-type layer as observed by SEM (see Figure 13). The B-type layer shows a disordered structure of small grains with diameters of 20 nm and is obviously porous.

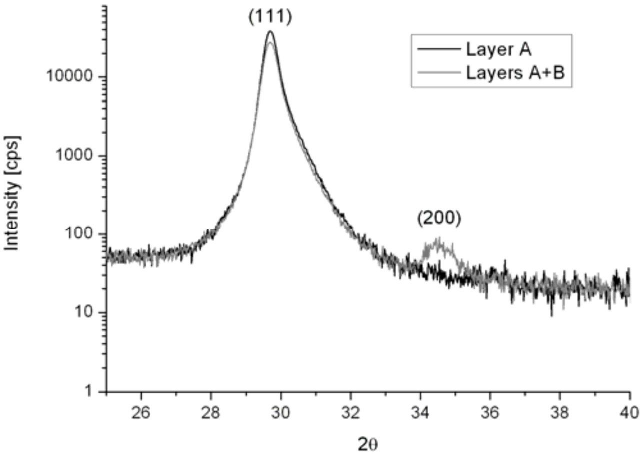

Figure 12: X-ray diffraction patterns of the YSZ after deposition of the layer A and A+B.

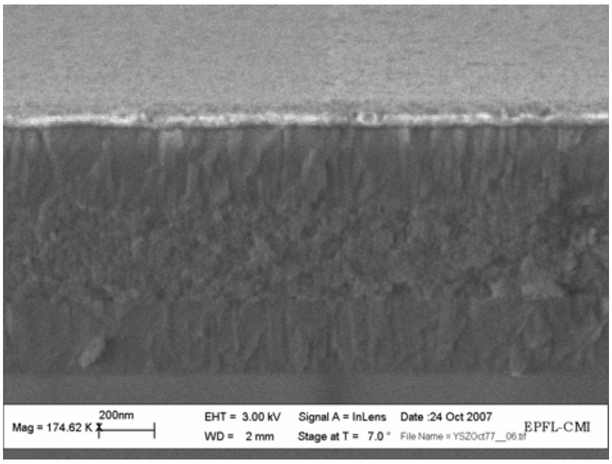

Figure 13: SEM cross section of a stack of three YSZ layers A+B+A covered by a 50 nm thick gold layer.

A TEM picture (Figure 14) shows the sequence of the three YSZ layers deposited onto Si substrate followed by Cr and Pt layers. The thickness of the 2nd YSZ layer of B-type (307 nm) is 25% larger than the thickness of each of the 1st and 3rd YSZ layer of A-type (245 nm). The A-type layers showed a dense columnar microstructure with columns having diameters between 50 and 100 nm. The grain size in the B-type layer is approximately 20 nm. Diffraction patterns show that the A-type layers are strongly (111) textured, whereas the B-type layers are randomly oriented. This phenomenon can be explained by a higher sputter yield of (111)-planes, leading to a partial or total suppression of (111)-oriented grains. Such phenomena are known from fcc metal systems such as aluminum. The 3rd layer - again of type A - is less textured than the 1st layer. Apparently, the columnar growth of (111) grains is disturbed by the nano porosity and inhomogeneous orientation of the 2nd layer.

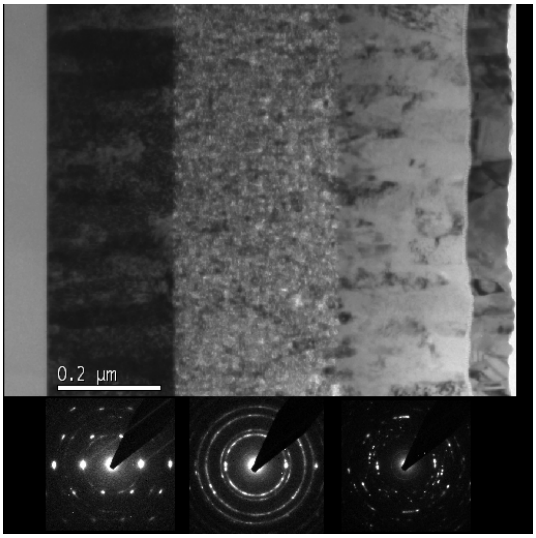

Figure 14: TEM cross section and diffraction patterns of the 3 layer YSZ electrolyte deposited on SiO_2 (left) and covered by a thin gold layer (right)

The relative mass density of the second layer was estimated using EDAX (Electron Diffraction X-Ray Analysis) by comparing the total intensity of the X-rays characteristic spectra taken in identical conditions on each layer. The X-ray intensity depends proportionally on the number of atoms excited by electrons. Assuming a similar thickness of the layers close to their interface, the X-ray intensities are directly proportional to the density of the material. For all three YSZ layers the spectra look very similar. The density ratios are *d2/d1*= 0.75 and *d3/d1* = 1. So the 2nd layer has a porosity higher than 25%. Because the atomic fluxes from the YSZ target are the same (same applied power) in the deposition chamber, the changes of densities induced by the different growth mechanism should be correlated with the thickness variation, The observed higher porosity (lower density) corresponds well with the observed larger thickness. Theses results prove that it is possible to disturb the columnar microstructure of the YSZ film by ion bombardment at lower temperature Even if the 2nd layer is porous, the (111) layer deposited onto it is dense and columnar as shown by TEM. For application in µSOFC, the electrolyte should be gas tight to prevent gas mixing between the anode and the cathode. For this purpose, we propose the deposition of two (111) oriented layers separated by a thin 2nd porous layer to prevent the formation of YSZ columnar grains along the entire film thickness.

3.2.3. Stress in (111) YSZ thin films

The stress in the multilayered film is mainly due to the dense (111) oriented layers. The porous (200) layer does not contribute. The stress in two YSZ (111) thin films with a thickness of 500 nm has been measured as a function of temperature in air by using the Tencor FLX 2900 described in the paragraph 3.1.2. The YSZ films were deposited by reactive sputtering from the ceramic target at a temperature T_{dep} of 430°C on oxidized silicon samples (1 x 4 cm^2), and then cooled down during 3 h in the process chamber at various oxygen pressures. To compensate the stress variation due to the presence of the 1.5 µm thick oxide layer, a sample that was not coated by YSZ was tested up to 700°C (Figure 15).

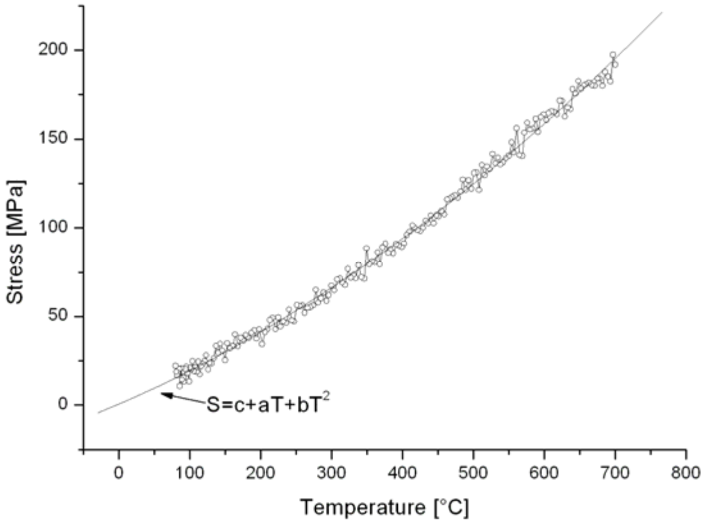

Figure 15: Stress versus temperature curve for a silicon sample covered with 1.5 μm of thermal wet silicon oxide.

The obtained stress versus temperature curve was fitted with a polynom of the second degree and this background was subtracted to the YSZ data according to the equation (3.3). The obtained coefficients are very close (0.501 x 10^{-6} K^{-1} and 0.25 10^{-9} x 10^{-4} K^{-2}) to the ones of quartz glass (0.518 x 10^{-6} K^{-1} and 0.29 10^{-9} x 10^{-4} K^{-2} [11]).

In case of a film reacting by pure elastic deformation, the thermal mismatch with the substrate causes a mechanical stress S_{th} during cooling down to room temperature that adds to a stress $S_{dep}(T_{dep})$ resulting from the deposition process. When growing at 430 °C, local diffusion at the growing surface should indeed reduce the compressive stress that might be caused by ion bombardment, thus $S_{dep}(T_{dep})$ should be relatively small. The experiment includes a heating ramp at 3.8°C/min from 20°C to 700°C, a plateau of 1 hour at 700°C and cooling to 70°C at the rate of -3.8°C/min. Below 100°C, the cooling rate is limited by the cooling capacity of the equipment.

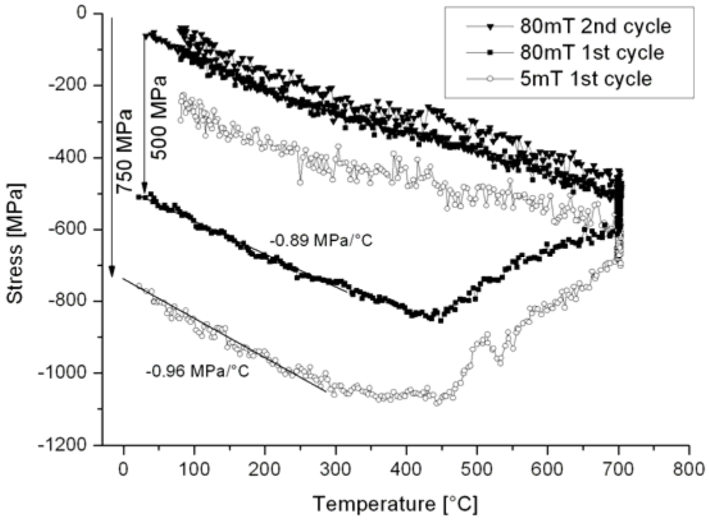

Figure 16: Total stress with temperature of YSZ thin films deposited at 500°C and then cooled for 3 hours in 80 mT or 5 mT of oxygen. The film cooled in 80 mT of O_2 has undergone two thermal cycles.

The thermal expansion coefficient of YSZ (10 ppm/K at 500°C, [14]) being considerably larger than the one of the silicon substrate (3 ppm/K), a tensile state of stress is expected at room temperature for the (111) films that are deposited at 430°C according to equation (3.15).

In case of ceramics, Young's modulus Y_{cer} and Poisson ratio ν_{cer} are reported as Y_{cer}=220 GPa, and ν_{cer}=0.315, respectively. Since our thin film exhibits a (111) textured columnar growth, it is more appropriate to use single crystal values valid in the plane perpendicular to the {111} direction. These were calculated as Y_{film} =190 GPa, and ν_{film}=0.27 from the stiffness constants given by Ingel and Lewis [12] (as explained in Appendix A.4). From equation 2.12, the thermal stress S_{th} is of:

$$S_{th} = \frac{(T_{dep} - T)\cdot(\alpha_{film} - \alpha_{sub})\cdot Y_{film}}{1 - \nu_{film}} = \frac{(703K - 298K)\cdot(10\times10^{-6}K^{-1} - 3\times10^{-6}K^{-1})\cdot 190GPa}{1 - 0.27} = 737MPa \quad (3.15)$$

In contradiction to expectations, however, we always obtained large compressive stresses, even when increasing the growth temperature (Figure 16). This means that a much different mechanism is responsible for stress development. We will show evidence that oxygen loss that leads to additional oxygen vacancies is the reason for stress development. Stoichiometric, charge neutral YSZ contains half as much oxygen vacancies as Y^{3+} ions. At not too high temperature, these are bound to the yttrium site [13] , more specifically to the 2nd neighbour oxygen positions [14]. Such vacancies can be considered as trapped vacancies (density c_{Vtp}) since the attractive Y_{Zr}' point defect does not move with the vacancy. The usual ionic conduction in YSZ is due to hopping of vacancies from trap to trap requiring an activation energy of 1.07 eV [15]. In reducing ambient, additional oxygen vacancies are formed by means of the process:

$$O_O^x \rightarrow V_O^{\bullet\bullet} + 2e' + \tfrac{1}{2} O_2(gas) \tag{3.16}$$

These occupy arbitrary oxygen sites and are not subject to a Coulomb attraction by Y dopants, as their charge is already compensated by the trapped vacancies. The additional oxygen vacancies are thus less bound and require less activation energy for hopping. In the following we call these the free vacancies (density c_{Vfe}). Such vacancies have been postulated earlier [15] and chemical stress T_{chem} induced by a change of the defects concentration in the film [16] or by gradient defect concentration, for example in the case of defects recombination [17], as already been reported in the literature. In equilibrium and respecting electrical neutrality, the concentration of free oxygen vacancies c_{vfe} is installed according the mass action law to yield the following concentration:

$$c_{Vfe} = \frac{4K(T)}{(p_{O2})^{1/6}} \tag{3.17}$$

where $K(T)$ is the reaction constant and p_{O2} the oxygen partial pressure.

It is well known that oxygen vacancies lead to an increase of the volume if we deal with a mechanically free body. In case of a clamped film, a stress S_{chem} results accordingly:

$$S_{chem} = \frac{Y_{film}}{1-\nu_{film}} \beta \cdot (c_{vfe} - c_{0,vfe}) \tag{3.18}$$

Where $(c_{vfe}$- $c_{0,vfe})$ is the change of free vacancies concentrations, $Y_{film}/1-\nu_{film}$ is the biaxial modulus of the film and β the volume change induced by the defect creation or movement. The parameter β is the proportionality factor relating strain and vacancy concentration. This factor is estimated to be 0.06 from atomistic calculations, knowing that when an oxygen ion is released from the YSZ lattice, three of the oxygen nearest neighbours move towards the vacancy and the second nearest neighbours move away from it thus increasing the lattice constant [18], as seen in Figure 17.

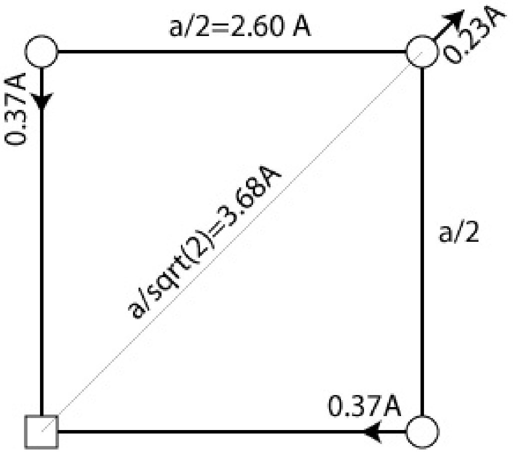

Figure 17: Expansion of the oxygen lattice in YSZ after the creation of an oxygen vacancy. The scheme shows a quarter of the lattice plane. The oxygen vacancy is represented by a square and the oxygen ions by circles. Adapted from [18].

We tested the hypothesis of oxygen pressure impact according to equations (3.17) and (3.18) by cooling down identically processed films at different oxygen pressures of 5 mT or 80 mT. The effect of oxygen pressure is clearly observed (Figure 16). According to equation (3.17), the stress ratio at room temperature is expected to be $16^{1/6}$=1.66. The experiment yields a ratio of 1.5 other than vacancy contibutions. The annealing experiments discussed later justify the assumption that the stress without oxygen vacancies is near to zero at room temperature, meaning that the whole stress at room temperature can be assigned to oxygen vacancies. The corresponding concentrations of oxygen vacancies created in the film are calculated as 3.2 % and 4.8 % for the films cooled in 80 mT and 5 mT of oxygen, respectively, when assuming the isotropic deformation without rigidity reduction by vacancy migration:

$$\begin{aligned} c_{vfe}(80mT) &= S_{chem}\left(\frac{Y_{film}}{1-\nu_{film}}\right)^{-1}\beta^{-1} = 500MPa\times\left(\frac{190GPa}{1-0.27}\right)^{-1}\times(6\%)^{-1} = 3.2\% \\ c_{vfe}(5mT) &= S_{chem}\left(\frac{Y_{film}}{1-\nu_{film}}\right)^{-1}\beta^{-1} = 750MPa\times\left(\frac{190GPa}{1-0.27}\right)^{-1}\times(6\%)^{-1} = 4.8\% \end{aligned} \tag{3.19}$$

More information is gained by heating/cooling cycles in air. Such cycles for T_{max}= 700°C are shown in (Figure 16). Theoretically, a misfit stress of -1.56 MPa/K should be seen in the linear behavior below 400 °C. The measured curve shows less, i.e. -0.96 MPa/K. It is very common to measure a smaller rigidity in thin films. In a recent paper, an even smaller value was published for the stress vs. temperature slope: 0.67 MPa/K [19]. Also by nanoindentation, a smaller stiffness with Y ranging from 120 to 150 GPa is observed in thin films [20]. This range of values is quite compatible with our findings (Y=120 GPa) if we assume the thermal expansion to be the same as in a cubic crystal. Various reasons may be forwarded for such a difference. One is of course the microstructure that might contain softer, or open grain boundaries, or eventually a size effect of the special (111)-orientation. It has been proposed by Lubomirsky and coworkers that in slow strain or stress accommodation processes the increase in elastic energy is partially counterbalanced by defect migration between two non-equivalent sites [21]. If such slow phenomena play role the stress change should depend on heating and cooling rates. We did not find any difference in slope when heating with 3.8°C/min or 10C°/min in the linear range below 400 °C (Figure 18). This means that such phenomena, if occurring are either much faster of much slower. In order to give a correction to the apparent rigidity, they would be required to be much faster, in contradiction with the findings in [21]

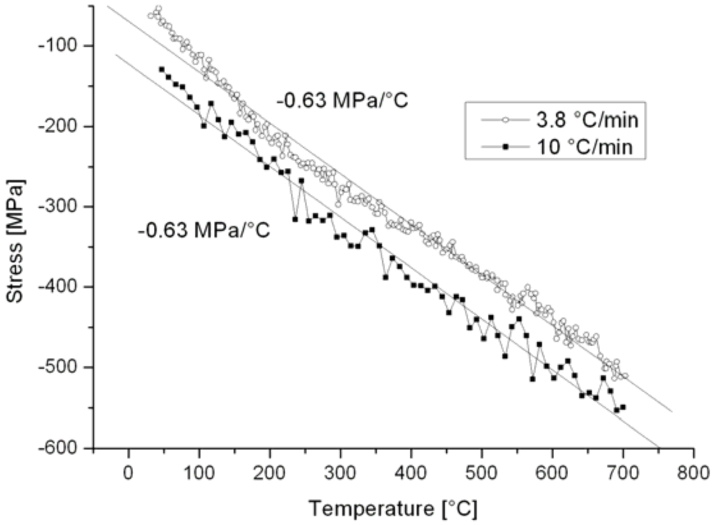

Figure 18: Comparison of the stress vs temperature curve for the same YSZ sample at two different heating speed 3.8 and 10 °C/min.

For the anomalous part above 400 °C, we have evidence that gas exchange with ambient air pressure is responsible for the anomalous stress behaviour observed at non-annealed films. The vacancy desorption process is a combination of diffusion processes in the bulk, and the oxygen chemisorption at the surface. The electrons created during the reduction process must stay around the vacancies, meaning that a free vacancy diffuses as kind of pseudo He atom. The complete process can be written as:

$$V_{O,fe}^{\cdot\cdot} + 2e \xrightarrow{diffusion} V_{O,fe}^{\cdot\cdot}(surface) + 2e(surface) + \frac{1}{2}O_2 + \longrightarrow O^x(surface) \qquad (3.20)$$

There are two thermally activated processes going on: The diffusion of vacancies with the electrons to the surface, and the up-take of oxygen, including the dissociation of O_2. It is more convenient to describe the latter process as a desorption of vacancies. Both processes are thermally activated and show thus similar temperature dependences. However, they should differ in their time (*t*) dependence.

If desorption is limited by the diffusion from the inside, the amount of desorbed vacancies γ per area follows the well known $\sqrt{Dt}$ behaviour, where D is the diffusion constant:

$$\gamma(t) = c_{Vfe}(surface)\sqrt{\frac{D_{Vfe}\cdot t}{\pi}} \tag{3.21}$$

The average vacancy concentration $\bar{c}_{Vfe}$ is diminished as $\bar{c}_{Vfe}(t) = \bar{c}_{Vfe}(0) - \gamma(t)/t_f$, where t_f is the film thickness. As we measure the average stress of the YSZ film, according to:

$$\bar{S}_{Vfe} = -\frac{Y_{film}}{1-\nu_{film}}\beta_{fe}\cdot\frac{1}{t_f}\int_0^{tf} c_{Vfe}(z)dz = -\frac{Y_{film}}{1-\nu_{film}}\beta_{fe}\cdot\bar{c}_{Vfe} \tag{3.22}$$

we obtain then as a function of time, at a given temperature:

$$\Delta\bar{S}_{Vfe}(T,t) = \frac{Y_{film}}{1-\nu_{film}}\beta_{fe}\cdot\frac{\gamma(T,t)}{t_f} = \frac{Y_{film}}{1-\nu_{film}}\beta_{fe}\cdot\frac{c_{Vfe}(surface)}{t_f}\sqrt{\frac{D_{Vfe}(T)\cdot t}{\pi}} \tag{3.23}$$

This equation does not strictly apply because the surface concentration decreases with time. However, as long as the change is small to the total amount of vacancies, we can do as if the concentration is constant for a certain time. Comparison with the experiment indeed shows that the fit with a $\sqrt{t}$ function works well (Figure 20). This means that we deal with rate limitation by diffusion from within the film. Doing the experiment for different temperatures, we can in addition derive the thermal activation energy E_a for the free vacancy diffusion as seen in the Figure 21:

$$D_{Vfe}(T) = D_{Vfe,0}\exp(-E_a/(kT)) \tag{3.24}$$

$$\Delta\bar{S}_{Vfe}(T,t) = B\cdot c_{Vfe}(surface)\cdot\exp\left(-\frac{E_a}{2kT}\right)\sqrt{t} \tag{3.25}$$

We can now make an approximation for the vacancy concentration in the surface layer, since this one must be smaller (or equal) to the average vacancy concentration. The stress curve gives a clear indication in the latter. At high temperature, the vacancy induced stress must go to zero. Therefore we conclude that the stress S_{Vfe} is zero, or nearly zero in the contribution to the cool down stress. In this way we obtain an absolute value for S_{Vfe} and thus also for the average vacancy concentration:

$$\frac{\bar{c}_{Vfe}(T_1)}{\bar{c}_{Vfe}(T_2)} = \frac{\bar{S}_{Vfe}(T_1)}{\bar{S}_{Vfe}(T_2)} \tag{3.26}$$

Hence we can write:

$$\Delta\bar{S}_{Vfe}(T,t) \leq B \cdot \bar{c}_{Vfe} \cdot \exp\left(-\frac{E_a}{2kT}\right)\sqrt{t} \tag{3.27}$$

Now, for calculating the stress curve during the whole temperature ramp (Figure 22), we used in iteration procedure:

$$S_{Vfe}(t=0) = S_{total}(t=0) - S_{total}(cool-down) \tag{3.28}$$

$$\bar{S}_{Vfe}(t_n) = \bar{\Sigma}_{Vfe}(t_{n-1}) + B \cdot \bar{c}_{Vfe}(0)\frac{\bar{S}_{Vfe}(t_{n-1})}{\bar{S}_{Vfe}(0)} \cdot \exp\left(-\frac{E_a}{2kT}\right)\sqrt{(t_n - t_{n-1})} \tag{3.29}$$

Since we have a constant heating rate, the time factor in Equation (3.29) is constant, and if we assume a constant vacancy density, the change in mechanical stress should follow an Arrhenius law with slope $E_a/2k$:

$$S_{def} = A \times e^{\frac{-E_{a,vfe}}{2kT}} \tag{3.30}$$

Before curve fitting, the thermal component of the stress was removed from experimental data by adding 0.96 MPa/K to the stress curve. The activation energy $E_{a,vfe}$ was derived as 0.54+/- 0.01 eV for both samples, independently of oxygen cooling pressure (Figure 19).

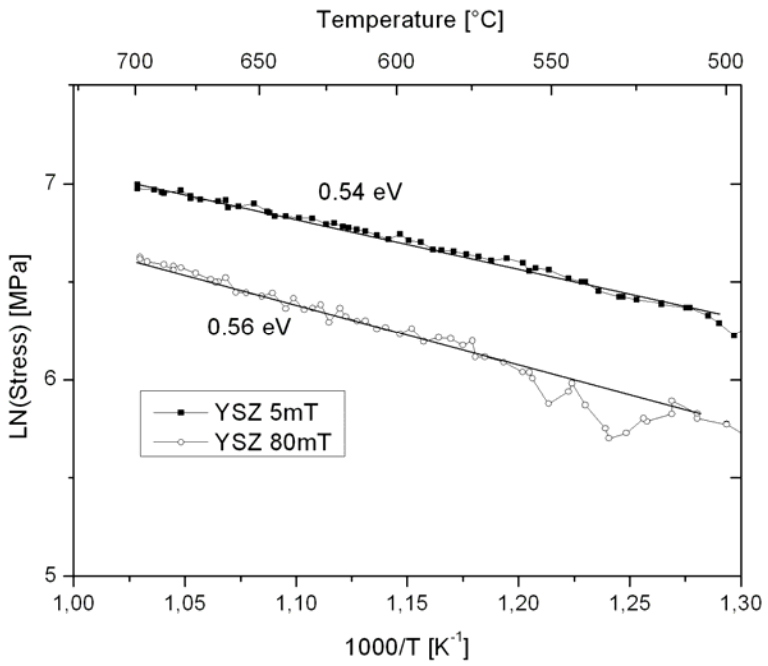

Figure 19: Arrhenius plot of the stress change due to the incorporation of oxygen ions in the YSZ films cooled in 5mT or 80mT of oxygen.

In order to test the time dependence as given is equation (3.25) and (3.27), we measured the stress of the film cooled in 80 mT as a function of time for various, stable temperatures. The film was heated from 25°C to 200°C at the rate of 3.8 °C/min and then it was kept at this temperature for 1 hour. Successive plateaus of 1 hour were made at 400°C, 600°C and 700°C. The heating rate between the plateaus was kept constant (Figure 20). The time dependence indeed follows a $\sqrt{t}$ behaviour, confirming the diffusion character of the underlying mechanism. The prefactor in front of the $\sqrt{t}$ term contains the exponential factor that again should reproduce an Arrhenius law. This is shown in Figure 21 and 22. This time a slightly higher value of 0.6 eV is obtained. Nevertheless, the agreement with the heating curve is quite satisfying.

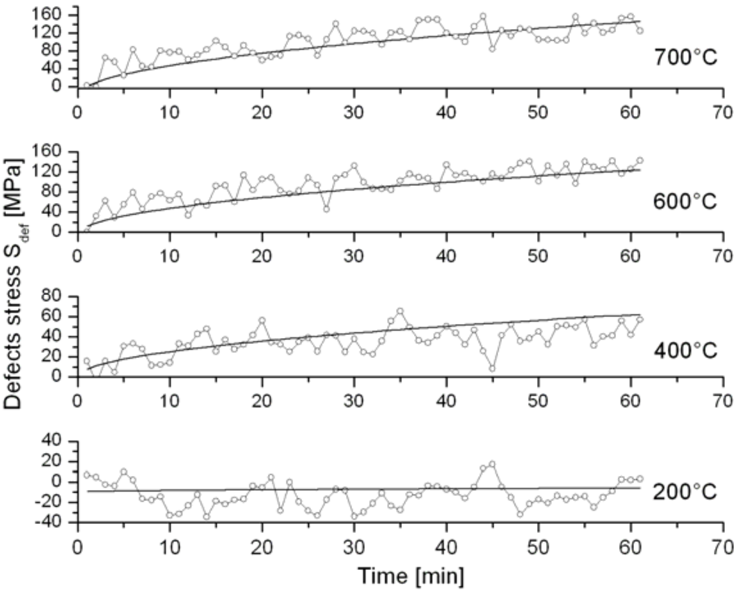

Figure 20: Variation of the stress in YSZ film with time for different temperatures

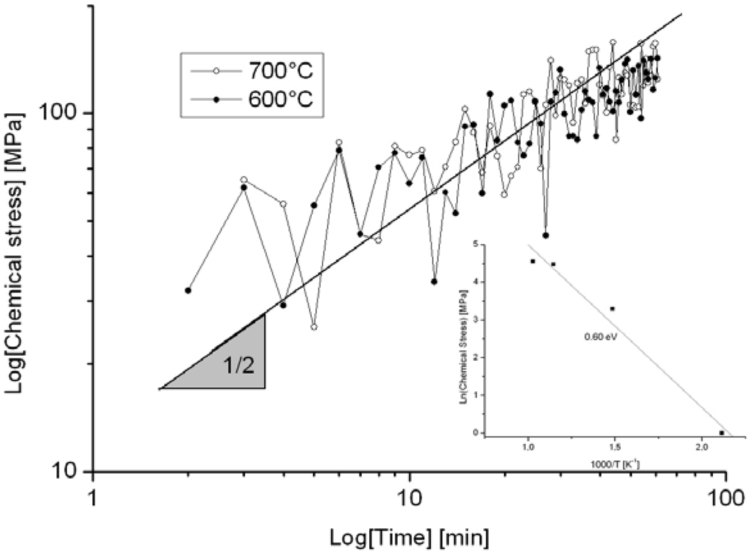

Figure 21: Log-Log plot of the chemical stress showing the square root dependency with time. Inserted: Arrhenius plot of the stress variation during 1 hour at 200°C, 400°C, 600°C and 700°C.

Finally, the experiment is compared to the overall behaviour as described by iteration equation (3.29), as seen in Figure 22:

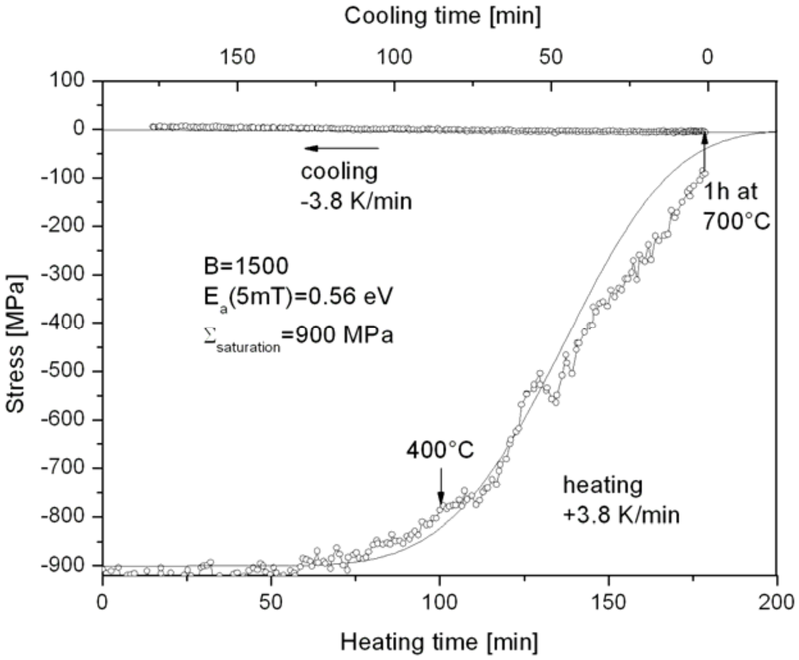

Figure 22: Stress change with time for the YSZ sample (cooled in 5mT of oxygen) measured experimentally during heating and cooling and compared with the iteration model including the diminishing vacancy concentration.

The obtained values of $E_{a,vfe}$ and prefactors are equivalent as for the previous experiment. The experimental deviations from the calculated curve are due a certain "noise" in the experimental curve at lower temperatures. The noise can be assigned to grain boundaries, which release vacancies quicker as the bulk. The deviation at higher temperature is rather due to the inaccuracy of the model that overestimates the diffusion flux at higher temperatures, where the small concentration gradients lead to smaller fluxes than assumed in the model.

All the stress experiments and their evaluation yield an activation energy for free O vacancy diffusion of 0.56-60 eV. This is almost half of the activation energy for trapped O vacancies (1.07 eV [20].). As reported in paragraph 3.2.4, the ionic conductivity of this YSZ film was measured at a capacitor of 2 mm diameter, yielding an activation energy of 0.94 eV.

Computer-based calculations have shown that in tetragonal zirconia the activation energies for the diffusion of oxygen ions differs with the presence of dopants [13]. In pure ZrO_2, the activation energy is of 0.30 eV and in yttria doped ZrO_2 it increases to 1.07 eV. In Cormack's work [15], it is claimed that the energy needed for ions diffusion is divided into two parts. The first is needed to separate the O^{2-} from its two associated Y^{3+} defects and the second is needed to move the ion through the zirconia lattice. The oxygen vacancies created during the post-deposition cooling under low oxygen pressure are not related to cationic Y^{3+} defects. We suppose that these vacancies are paired with electrons, as the Zr^{4+} cations are monovalent. Thus these additional vacancies are randomly distributed in the film and are mostly surrounded by Zr^{4+} ions as if they were in pure ZrO_2. Therefore the activation energy for the diffusion of these free vacancies, is smaller and calculated as 0.3 eV in ref. [15]. Obviously, we measure something in between. What is not clear in the cited theoretical work is the question of charge compensation. Since Zr vacancies cannot be formed during cool down of the film, we only can postulate free electrons. Since they have to migrate with the O vacancies, the overall activation energy might be increased. Finally we also have to explain why a higher activation energy is obtained by conductivity measurements. Reliable data for the Arrhenius fit are only obtained at higher temperatures. There, the ionic conduction with trapped vacancies is dominating, and so the measured value is closer to 1.07 than to 0.6 eV. In addition, the free vacancies should be removed with time when measuring in air.

The study of the behaviour of the stress in the YSZ thin films with the temperature helps to discriminate between the O^{2-} ions induced by the doping and the ones created by the process. The high compressive stress due to the vacancies created during the post process cooling will break YSZ membranes. Annealing of these films in air permits to fill the unexpected oxygen vacancies and to stabilize the behaviour of the film up to 700°C. After annealing, the variation of the stress with the temperature is limited and 500 nm thick membranes can survive thermal cycles up to 600°C as seen in Chapter 4.

3.2.4. Electrical characterization of multilayer and single layer YSZ films

The YSZ films are deposited on a titanium platinum bottom electrode which was deposited by sputtering with the parameters given in Table 4. Ti/Pt bottom electrodes with respective thicknesses of 5 and 100 nm were deposited on silicon wafers with a 1 μm thick wet oxide layer. The wafers were subsequently cut into 4 x 1 cm^2 samples. The depositions were carried out in the SPIDER sputtering tool.

Table 4: Deposition parameters for the Ti/Pt (5/100nm) electrode in the SPIDER.

Film	**Ar flow [sccm]**	**DC power [W]**	**Dep. time [sec]**	**Temperature [°C]**	**Rate [nm/min]**
Ti	15	1000	3	300	250
Pt	15	1000	22	300	280

Then YSZ was deposited onto the platinum bottom electrode in the form of a single layer or of a stack of three layers. The parameters for these two types of depositions can be found in Table 2 and Table 3.

Platinum electrodes with a thickness of 100 nm were deposited by DC magnetron sputtering in the Nordiko tool through a patterned hard mask. The resulting electrodes are circular with a diameter of 2 mm. The parameters for deposition are given in Table 5:

Table 5: Deposition conditions for platinum electrodes in the Nordiko tool.

Press. [mT]	**Ar flow [sccm]**	**O_2 flow [sccm]**	**DC power [W]**	**Dep. time [min]**	**Temperature [°C]**	**Rate [nm/min]**	**Dist. T-S. [mm]**
5	40	0	45	6	25	17	100

Capacity C and losses tanδ of multilayered YSZ films were measured as a function of temperature. Figure 23 shows the Arrhenius plots of the film conductivity. During the first temperature ramp to 520°C, the conductivity shows a deviation from the ideal behaviour above around 280°C. This temperature corresponds approximately to the deviation from the linear stress/temperature behaviour during the first anneal. At this point, the conductivity is lower than during the second temperature ramp. As during stress measurements, this behaviour is only observed during the first annealing of the film and seems irreversible, at least when the film is kept in the air. Possibly, the free oxygen vacancies build up space charges that are hindering the motion of the ordinary trapped vacancies. The second cycle also presents a deviation of its conductivity from the linear activation behaviour. If as during stress measurements, the oxygen saturation is achieved only after several cycles up to 700°C, the maximal value of the conductivity has not been reached at 500°C. After annealing at 500°C, the maximal conductivity reaches 0.007 S/m at 500°C as seen in the Figure 23:

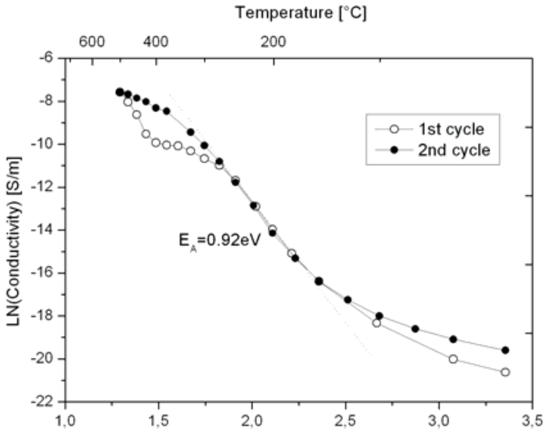

Figure 23: Arrhenius plots of the conductivity (in S/m) versus 1000/T for a 700 nm YSZ film measured at 100Hz. The conductivity was measured during the 1st and 2nd heating cycles.

The conductivity is comparable to literature value (5.5 x 10^{-3} S/m at 500°C [22]) of thin film deposited by pulsed laser deposition. This study also confirms that the conductivity is increased when the film is annealed for 8h at 800°C (1.5 x 10^{-2} S/m). An activation energy of 0.92 eV was measured, with the method explained in 3.1.3.4, and is slightly lower than the literature values for PLD films (1.03 to 1.15 eV).

3.3. CGO thin film electrolyte

3.3.1. Growth conditions and microstructure characterization

Ceria doped gadolinia thin films containing 20% molar Gd_2O_3, referred to as CGO, were sputter deposited from 2 different targets:

1) A ceramic target of 4” diameter and ¼” thickness, from Neyco, containing 20% mol. of gadolinia with a purity of 99.9%.
2) A metallic target of 4” diameter and ¼” thickness, from Kurt J. Lesker made of a cerium gadolinium alloy and containing 13% atomic of Gd.

The ceramic target was pasted on a molybdenum disk to improve the thermal conduction to the target holder.

The composition of the (500 nm) CGO thin films deposited was elucidated by Energy Dispersive X-ray spectroscopy (EDX) in SEM. The intensities of the Ce L and Gd L lines were used to find out the %at. of cerium and of gadolinium. The films deposited from the stochiometric ceramic target ($Ce_{0.8}Gd_{0.2}O_2$) contain of 30%at. of Gd in place of 20%. To compensate this excess of gadolinium, the metallic target was chosen with a Ce-richer composition ($Ce_{0.87}Gd_{0.13}$). The EDX shows that the films deposited from the metallic target can reach the stoichiometric composition of $Ce_{0.8}Gd_{0.2}O_2$ (see Table 6).

Table 6: Composition of the targets and deposited CGO films

Target type	Target composition	Film composition
Ceramic	$Ce_{0.8}Gd_{0.2}O_{2-x}$	$Ce_{0.7}Gd_{0.3}O_{2-x}$
Metallic	$Ce_{0.87}Gd_{0.13}$	$Ce_{0.81}Gd_{0.19}O_{2-x}$

The choice of a metallic target is due to the fact that the ceramic target starts to crack and peel off after a very small number (<20) of depositions. Thus, it was replaced by a metallic target after the composition of the film was proven to be too rich in Gd. This metallic target showed a better chemical and mechanical stability and can be used for more than 50 depositions without any deterioration.

The first objective of this work was to find out parameters for the deposition of the CGO thin films from the metallic target. 200 nm thick CGO films were deposited onto bare (100) silicon samples with dimensions of 4 x 1 cm^2, or covered with 1µm of wet oxide or 100 nm of (111) Pt. In order to analyze the film orientation, the samples have been deposited under various conditions as listed in Table 7:

Table 7: Conditions of deposition for CGO thin films from the metallic target. *) the sample's name is given without the suffix referring to the substrate type (Si for silicon, Pt for platinum and Ox for wet oxide)

Sample*	**Pressure [mT]**	**Ar flow [sccm]**	**O_2 flow [sccm]**	**RF power [W]**	**Temperature [°C]**	**Dist. T-S. [mm]**
Cold Ar	15	10	0	250	20	100
Cold O	15	10	10	250	20	100
Hot Ar	15	10	0	250	500	100
Hot O	15	10	10	250	500	100

The texture index P(hkl) is defined as the ratio of the peak intensity I(hkl) relative to the absolute intensity I_0(hkl) for a randomly oriented powder (for $Ce_{0.8}Gd_{0.2}O_2$ JCPDS file #33-784) divided by the sum of all the intensities relative to their absolute values [23]:

$$P(hkl) = \frac{\dfrac{I(hkl)}{I_0(hkl)}}{\sum_i \dfrac{I(hkl)_i}{I_0(hkl)_i}} \tag{3.31}$$

The texture indexes for all orientations of growth have been measured on the three different substrates at RT and at 500°C, with pure Ar flow or with a mix of Ar and O_2 (ratio 1/1). The texture indexes for the twelve samples are given in Figure 24:

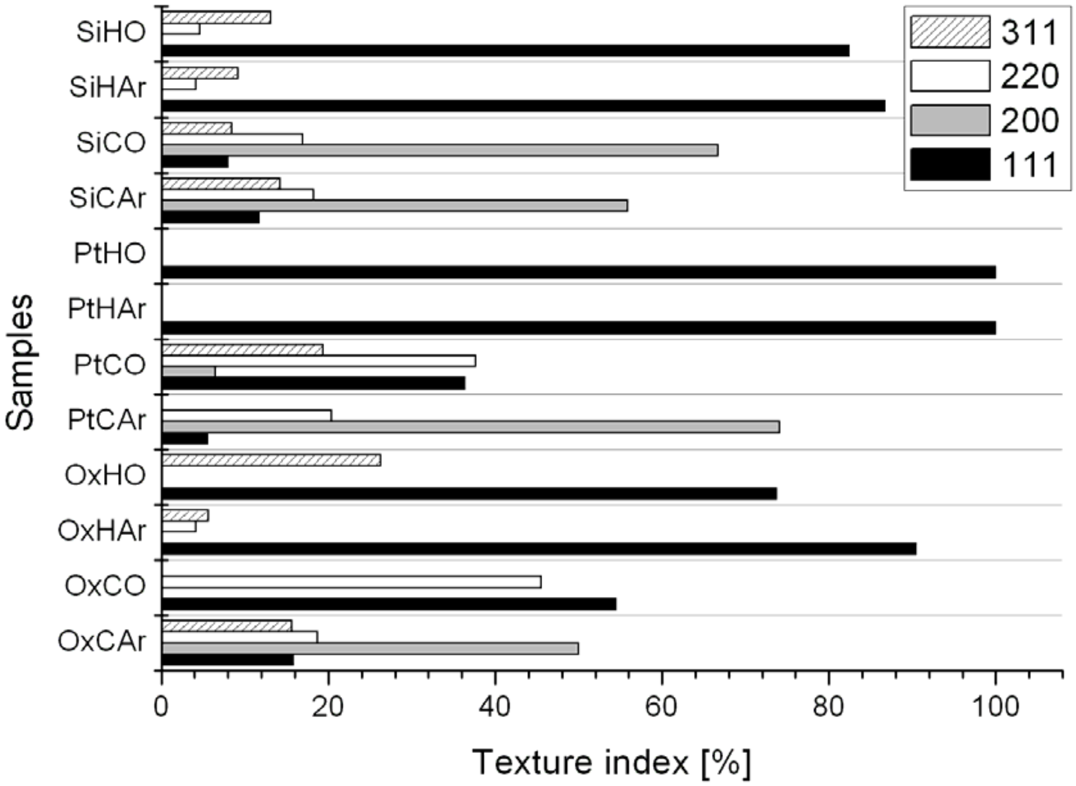

Figure 24: Texture index for the various CGO film orientations for the different samples. The 2 first letters of the name refer to the substrate (Ox for amorphous SiO_2, Pt for (111) Pt and Si for (100) Si). The 3^{rd} letter refers to the temperature (H for 500°C and C for 25°C) and the last one to the gas atmosphere (Ar for pure argon and O for a 1/1 mix of Ar and O_2).

The films sputtered at room temperature do not present any preferential orientation. The {111}-texture is favoured by the high temperature (500°C) and by the presence of the (111) platinum layer. On this substrate, the CGO film has a perfect {111} texture. On the amorphous SiO_2, the maximal texture index for the {111}-orientation is of 90 % and on Si it reaches 87%. A pure argon atmosphere also helps the growth of the grain oriented in the (111) direction but only by a few percents. For the devices, the film will be deposited on a Pt mesh covering a silicon oxide layer. Thus the control of the texture will be more difficult than on small homogenous samples. The deposition conditions used for the CGO films comprised in the μSOFC structure are given in Table 8:

Table 8: Deposition conditions for the CGO films used as electrolytes for the μSOFCs

Pressure [mT]	**Ar flow** [sccm]	**O_2 flow** [sccm]	**RF power** [W]	**RF voltage** [V]	**Temperature** [°C]	**Rate** [nm/min]	**Dist. T-S.** [mm]
15	10	10	250	180	500	2.4	100

After being deposited, the CGO films were cooled for 3 hours in the chamber at the base pressure (~5 x 10^{-6} bar).

On a 4” Si (100) wafer the thickness of the film deposited with the conditions shown in Table 8 varies by 30% from the border to the centre of the wafer. This inhomogeneity is due to the small size of the target and to the use of a magnetron that confines the plasma over the centre of the wafer [1].

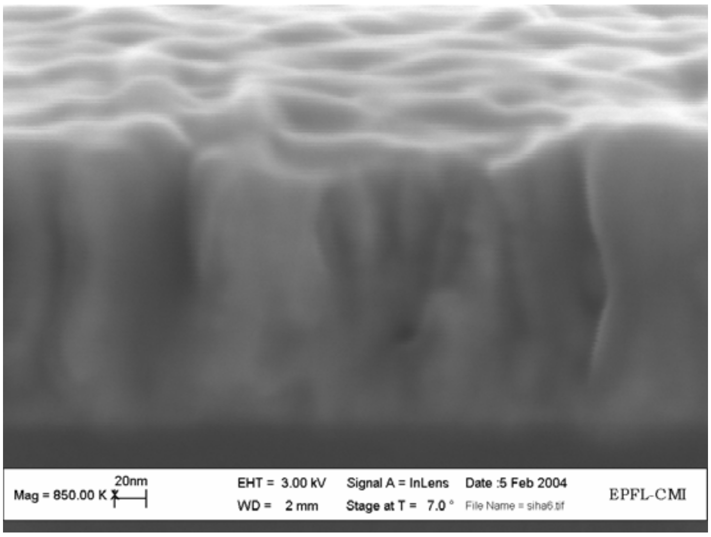

Figure 25: SEM cross section of a 100nm CGO thin film deposited on SiO_2

3.3.2. Stress in the CGO thin film

The cerium is capable of having a +III or +IV valence. Thus in reducing conditions, Ce^{+3} ions can exist in the crystals [24, 25]. The reduction of Ce^{4+} ions can also lead to hopping electronic conduction at low oxygen pressures ($<10^{-15}$ atm [26]). The reduction of cerium ions creates oxygen vacancies:

$$O_O^x + 2Ce_{Ce}^x \rightarrow \tfrac{1}{2}O_2 + V_O^{\bullet\bullet} + 2Ce_{Ce}' \qquad (3.32)$$

The possible existence of two different types of cationic defects (Gd^{3+} and Ce^{3+}) is the most important difference between CGO and YSZ. As in YSZ, the loss of oxygen ions due to the film sputtering process creates stress [21]. Ce^{3+} has a greater ionic radius than Ce^{4+}, 1.14 Å in place of 0.97 Å [27] and can be a reason for compressive stress in addition to the oxygen vacancies. The cohabitation of these two types of defects and the possible reactions between them and with Gd^{3+} complicate the analysis of stress measurements. For a better understanding, some authors have defined new parameters such as the non-stoichiometry δ. δ is the oxygen deficit in the CGO composition written as $Ce_{1-y}Gd_yO_{2-y/2-\delta}$.

The relation between δ, due to the formation of oxygen vacancies in low oxygen pressure p_{O2} and at high temperatures, and the subsequent strain has been measured [24]. This strain is positive and varying with the -¼ power of the p_{O2} and with the -1/2 power of the concentration of Gd^{3+}.

$$\delta \propto [Gd_{Ce}^{'}]^{-1/2} \, p_{O_2}{}^{-1/4} \tag{3.33}$$

Thus, the presence of oxygen vacancies (ie. $\delta>0$) increases the volume of the film at low p_{O2} and at sufficient high temperatures. The deformation is then proportional to the non-stoichiometry δ. As in YSZ, oxygen vacancies induce a compressive state of stress.

It was also reported that even the association of Gd^{3+} and oxygen vacancies can lead to stress variations [21]:

$$V_O^{\bullet\bullet} + Gd_{Ce}^{'} \underset{\Delta S>0}{\overset{\Delta S<0}{\rightleftarrows}} (V_O^{\bullet\bullet} + Gd_{Ce}^{'})^{\bullet} \tag{3.34}$$

It is proposed in the cited work that by pairing or un-pairing Gd^{3+} and oxygen vacancies, the film compensates mechanical stress even at room temperature and under atmospheric pressure.

The stress of CGO thin films with a thickness of 100 nm has been measured as function of temperature in the air by using the Tencor FLX 2900 as described in the paragraph 3.1.2. The experiment include a heating ramp at 4.4°C/min from 20°C to 700°C and a cooling to 70°C at the rate of -4.4°C/min. Below 100°C, the cooling rate is limited by the cooling capacity of the equipment. The films were deposited from the ceramic CGO target on 4 x 1 cm^2 silicon samples. A set of samples was deposited at 20°C and the other at 600°C with the parameters corresponding respectively to CO and HO as given in Table 7.

The Figure 26 shows the stress/temperature curves for the two types of samples:

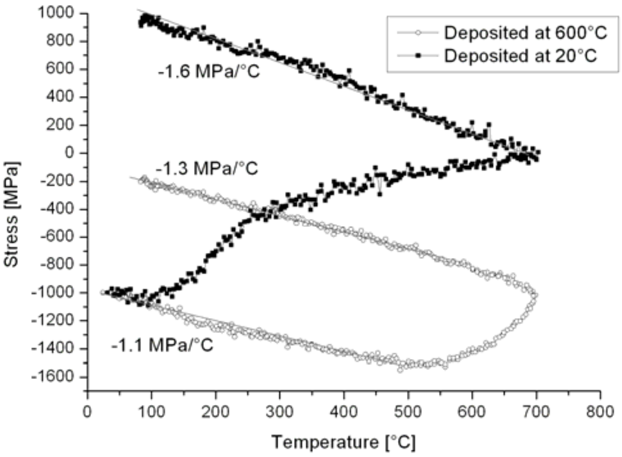

Figure 26: Total stress with temperature for CGO films deposited at 20°C or at 600°C.

Both the CGO film deposited at 20°C and the film deposited at 600°C are under a compressive state of stress of -1 GPa after deposition. For depositions at 600°C, the loss of oxygen ions during the cooling in the sputtering chamber can be a reason for this state of stress as it was the case for YSZ thin films. Then during annealing, oxygen ions are incorporated into the film decreasing its volume and creating a tensile stress (Figure 26). Comparing the stress/temperature curves of the samples deposited at 20°C and 600°C brings some experimental evidences. First, the slope calculated from the linear part of the stress/temperature curves (in MPa/°C, see Figure 26) increases with decreasing compressive residual in the films. This slope is due to the stress induced by the thermal mismatch which is proportional to the elastic modulus of the films as discussed earlier. In oxides, the elastic modulus decreases with the increasing concentration of oxygen vacancies [28]. A steeper curve means that less oxygen vacancies are present. The modulus for the different CGO films and after different anneals can be calculated using otherwise standard parameters (ν_{CGO}=0.33 and α_{CGO}= 12 ppm/K [16]) and are listed in Table 9:

Table 9: Young modulus for the different CGO films

Deposition temperature [°C]	Annealing procedure	Slope [MPa/K]	Elastic modulus [GPa]
600°C	As deposited	-1.1	122
600°C	One cycle to 700°C	-1.3	144
600°C	Two cycle to 700°C	-1.4	156
20°C	As deposited	-1.1	122
20°C	One cycle to 700°C	-1.6	178

This means that after annealing, the film deposited at 20°C has incorporated more oxygen ions than the one deposited at 600°C, and is thus stiffer. The 600°C film can indeed remove further vacancies during a second anneal, and increase its elastic modulus from 144 to 156 GPa (Figure 27):

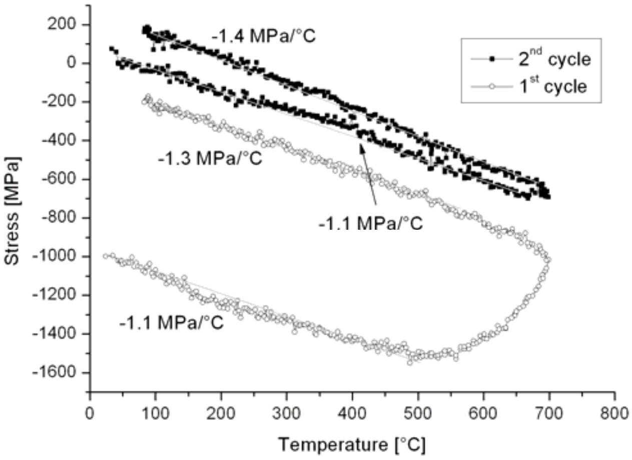

Figure 27: Total stress with temperature for CGO films deposited at 600°C for 1st and 2nd cycles of annealing.

Without annealing treatment the CGO membrane are subject to strong compressive stress as seen in the Figure 28.

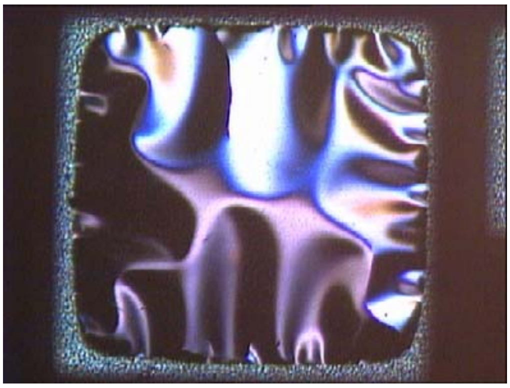

Figure 28: 500μm wide CGO membrane subject to compressive strain.

The room temperature deposited film can incorporate oxygen ions faster than the one deposited at 600°C. As seen in Figure 27, the film deposited at 600°C needs several annealing cycles to reach the elastic modulus, or oxygen ions concentration, of the sample deposited at 20°C.

For the films deposited at room temperature, the effect of the oxygen partial pressure in the chamber has been studied more carefully. Three films were deposited under 3 different oxygen pressures p_{O2} (0 mT, 7.5 and 10 mT). The total pressure was kept at 15 mT with addition of argon. The stress/temperature curves of these films are given in the Figure 29:

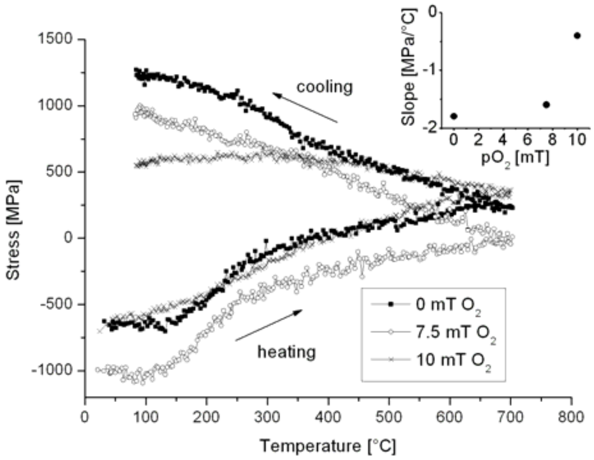

Figure 29: Stress/temperature curves for CGO thin film deposited at 25°C from a ceramic target with different oxygen pressure (0, 7.5 and 10 mT). The inserted graph shows the slope in MPa/°C of the cooling ramp for the different oxygen pressures.

The change of stress during the cooling was measured for the 3 films and the elastic modulii calculated as previously are given in Table 10:

Table 10: Young modulus for the CGO films sputtered at different oxygen pressures.

Deposition temperature [°C]	**Oxygen pressure during deposition [mT]**	**Slope [MPa/°C]**	**Elastic modulus [GPa]**
20°C	0	-1.8	200
20°C	7.5	-1.6	178
20°C	10	-0.4	44

The elastic modulus is higher for the film deposited without oxygen and then decreases as p_{O2} increases. During the annealing, the films deposited at low p_{O2} can incorporate more oxygen than the film deposited in pure argon. The film deposited at high temperatures or high p_{O2} are more susceptible to incorporate oxygen ions during their depositions. Then during cooling, the films deposited at 500°C loose oxygen and become compressive. When annealed to 700°C, these samples can incorporate more oxygen than the film deposited at high p_{O2}.

To understand better how the two types of films incorporate oxygen during annealing we calculate the Arrhenius plot of the chemically induced stress with *1/T* as in paragraph 3.2.3. As seen in the Figure 30, there are two different activation energies related to this phenomenon:

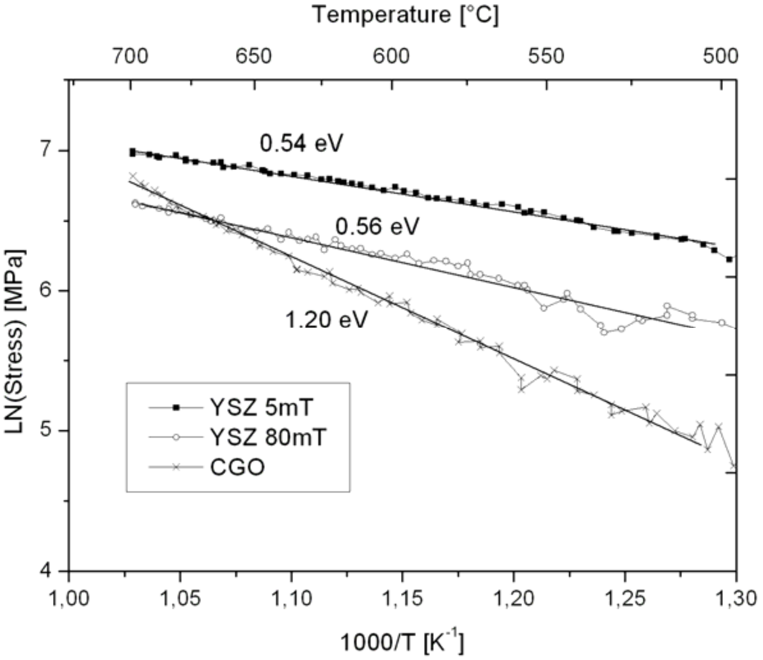

Figure 30: Arrhenius plots of the chemical stress (in MPa) for the annealing of CGO thin films deposited at 530°C compared with YSZ film deposited at 430°C.

For a better understanding of the mechanisms of oxygen ion diffusion, we compare CGO films with YSZ. As in YSZ, it is supposed that incorporation of oxygen ions relieve the stress by filling vacancies. The increase of the elastic modulus with the annealing cycles clearly confirms this phenomenon. In YSZ, the activation energy that has been observed is smaller than in the CGO (0.5 eV in place of 1.2 eV for the films deposited at high temperatures). In CGO, the oxygen vacancies can be trapped either by Ce^{+3} or Gd^{+4} ions. As said before, the change of valency is not possible in YSZ, as the zirconium ions cannot have a valency of +III. For divalent ions, like Ce, the negatively charged defect can be the cation. In YSZ, after deposition, a major part of the oxygen vacancies are not associated with Y^{3+} ions because these cations are already associated with the vacancies induced by the doping with yttria. In CGO, the oxygen vacancies can be trapped by the Ce^{+3} ions. Therefore the activation energy for the diffusion of these free vacancies, or the converse ions diffusion, should be higher than in YSZ as shown in Figure 31:

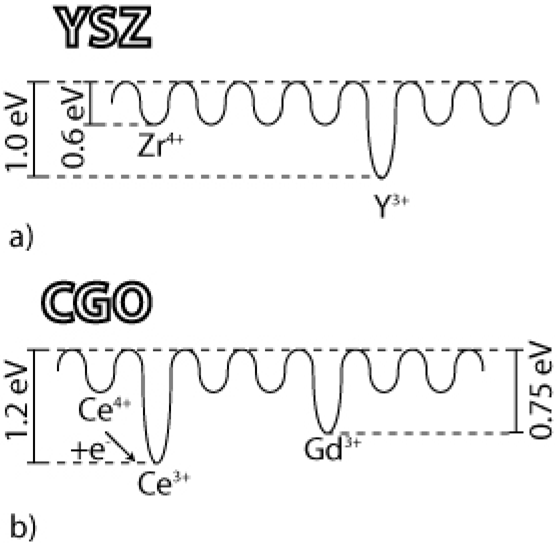

Figure 31: Proposed ionic potentials of the YSZ (a) and CGO (b). The activation energies for ionic conduction vary with the type of next cation.

The activation energy for the ionic conduction of CGO that was measured in this work (see paragraph 3.3.3) and of the literature are in the range of 0.75 eV [29, 30]. As in YSZ, we claim that this is the energy required to move an oxygen vacancy away from a Gd^{3+} ion as all the free vacancies were filled during the annealing treatment of the film before conduction measurements.

3.3.3. Electrical characterization of CGO thin films

The CGO films were deposited on silicon 4 x 1 cm^2 samples covered with a 1 μm thick wet oxide layer. Two CGO thin films with composition of $Ce_{0.7}Gd_{0.3}O_{2-x}$ and $Ce_{0.8}Gd_{0.2}O_{2-x}$ were prepared by reactive magnetron sputtering with the parameters given in Table 8. The $Ce_{0.7}Gd_{0.3}O_{2-x}$ was deposited from the ceramic target and the $Ce_{0.8}Gd_{0.2}O_{2-x}$ from the metallic target (see Table 6). Platinum electrodes (100 nm thick) were sputtered in the Nordiko with parameters given in Table 5 at both ends of the sample. The conductivity of the 200 nm CGO layers was measured in the plane of the film between the two electrodes separated by 1 mm. The platinum wires used for the contact were attached on the Pt electrodes with a commercial Pt paste. Then the paste was sintered at 500°C during 1 hour. The measurements were held in a tubular furnace in oxygen with the method explained in 3.1.3.4.

The Arrhenius plots are given in the Figure 32. The conductivity of the 80/20 films is higher than for 70/30 films. The 80/20 CGO has a conductivity of 0.5 S/m at 550°C and the 70/30 film of 0.06 S/m at 600°C. The adhesion between the Pt paste and the very smooth Pt electrodes limits the measurements to this range of temperatures. For the operation of the μSOFC, the conductivity of the 80/20 film was sufficient and comparable to the literature value at this temperature (0.53 S/m [30]). The activation energies for the 80/20 film is lower than the values reported in the literature (0.72 eV [29] and 0.78 eV

[30]). Albeit, CGO was considered as a very good ionic conductor at low temperatures [9, 31], the hopping conduction due to the reduction of Ce ions in H_2 makes it very difficult to use in thin film form for SOFC applications. CGO thin films with columnar grain boundaries can be reduced through their entire thickness and it results in electronic leakage in the cell. Thus CGO was abandoned and replaced by YSZ.

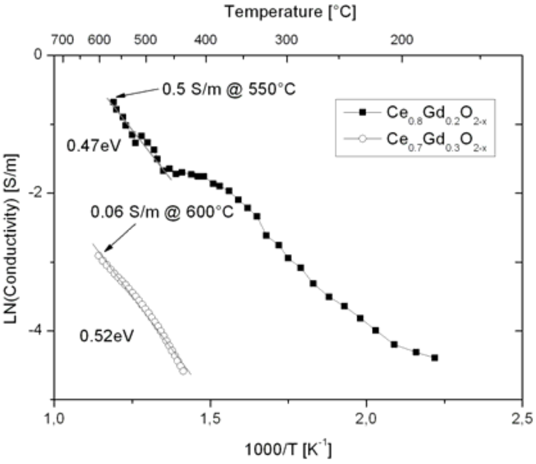

Figure 32: Arrhenius plots of the CGO thin films conductivity. The $Ce_{0.7}Gd_{0.3}O_{2-x}$ film was deposited from the ceramic target $Ce_{0.8}Gd_{0.2}O_{2-x}$ from the metallic target.

$Ce_{0.8}Gd_{0.2}O_{2-x}$ conductivity was measured by impedance spectroscopy at different temperatures (70°C, 200°C, 300°C 400°C and 500°C) in air. The impedance spectra are obtained with an HP 4194A Impedance Analyzer as described in 3.1.3.3. The sample is in the form of a cylindrical capacitor with a diameter of 2 mm and a thickness of 300 nm with Pt electrodes deposited as explained in the paragraph 3.2.4.

In the Nyquist plot, the curve for each temperature are semicircles. The resistance of the film was obtained by the method described in 3.1.3.3.

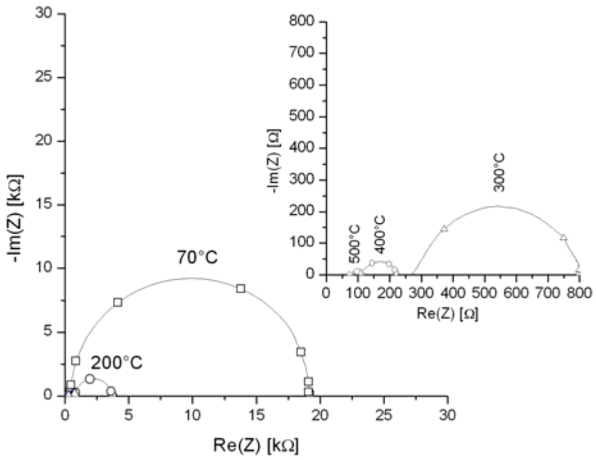

Figure 33: Impedance spectroscopy measurement of the $Ce_{0.8}Gd_{0.2}O_{2-x}$ at different temperatures.

An Arrhenius plot of $R_{//}$ for the different temperatures permits to calculate an activation energy of 0.56 eV for the conductivity in the CGO film. This value is slightly higher that the one measured by DC in the plane of the film.

No further investigation has been carried on the CGO films as the cells fabricated with these films show zero OCV. It is assumed that the reduction at the anode side leads to large electronic conduction across the film.

3.4. LSCO thin film cathode

3.4.1. Growth conditions and microstructure characterization

Strontium doped lanthanum cobaltite films, referred to as LSCO were also deposited by reactive magnetron sputtering from a $La_{0.32}Sr_{0.68}CoO_3$ ceramic target prepared by sintering. This set of films is deposited on small silicon samples (4 x 1 cm^2) covered by 1 µm of SiO_2 grown by wet oxidation. The deposition parameters were adapted from the work of Masumuto et al. [32] and are given in Table 11:

Table 11: Deposition conditions for the LSCO thin films.

Pressure [mT]	**Ar flow [sccm]**	**O_2 flow [sccm]**	**RF power [W]**	**RF voltage [V]**	**Temperature [°C]**	**Rate [nm/min]**	**Dist. T-S. [mm]**
15	0	20	100	-	550	0.5	100

After being deposited the LSCO films were cooled for 3 hours in the chamber at the base pressure of ~5 x 10^{-6} bar.

The LSCO films will serve as dense and thin cathode for the µSOFC. Thus the low rate of deposition is not a critical issue. X-ray diffraction shows that the LSCO film has no preferential orientation (see Figure 34). The low intensity of the different peaks is due to the low thickness of the sample (50 nm).

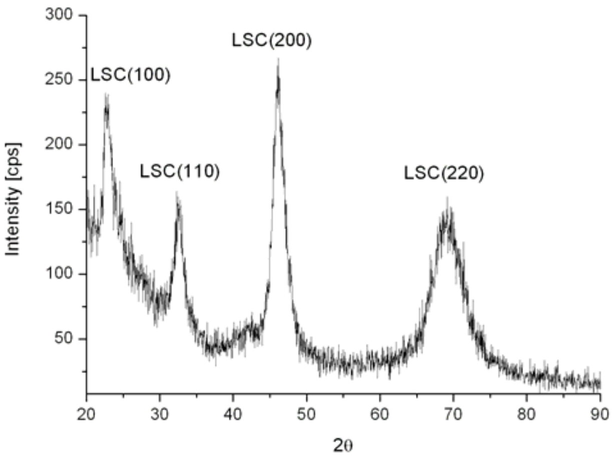

Figure 34: X-ray diffraction pattern of a 50nm thick LSCO deposited on amorphous SiO_2.

3.4.2. Electrical characterization

The LSCO films were deposited with the conditions of Table 11 on silicon 4 x 1 cm^2 samples covered with a 1 µm thick wet oxide layer. Platinum electrodes (100 nm thick) were sputtered in the Nordiko with parameters given in Table 5 at both ends of the sample. The conductivity of the 200 nm LSCO layers was measured in the plane of the film between the two electrodes separated by 1 mm. The platinum wires used for the contact were attached on the Pt electrodes with a commercial Pt paste. Then the paste was sintered at 500°C during 1 hour. The measurements were held in a tubular furnace in oxygen with the method explained in 3.1.3.4. The Arrhenius plot of the LSCO conductivity is given in Figure 35:

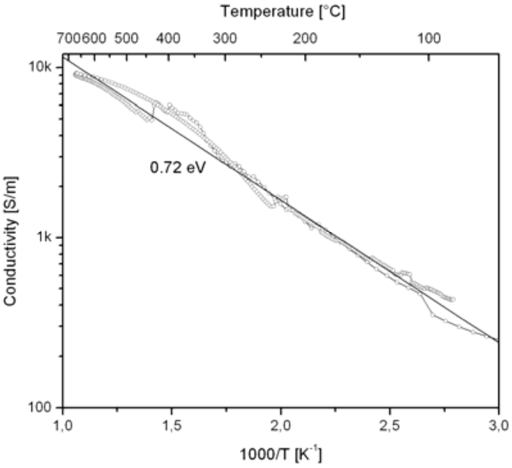

Figure 35: Arrhenius plot of the in-plane conductivity of the LSCO film measured in oxygen.

Reaching 9 x 10^3 S/m at 650°C the conductivity of the LSCO film is higher than expected. The activation energy amounts to 0.72 eV.

3.5. Ni-CGO composite thin films

As explained in Chapter 1, the morphology of the electrode is very important for the efficiency of the cell. The anode should be permeable to the fuel, i.e. porous, and conduct ions and electrons. Thus, a porous film composed of an electronically conduction phase (nickel) and of an ionically conducting one (CGO) is a very good candidate for the anode. For this purpose, porous composite films of nickel and CGO were co-deposited by reactive magnetron sputtering at high pressure by rotating the substrate over the two targets.

3.5.1. Study of the morphology of porous composite nickel-CGO thin films

Nickel-CGO porous composite films were deposited by co-sputtering in the Nordiko tool. The CGO deposition was made from a metallic target as reported previously in paragraph 3.3. The nickel was deposited by using a commercial nickel foil provided by Goodfellow. The films were grown by sequential deposition of the CGO film during the time A and of nickel during the time B or by rotating the substrate over the two targets at a given rotation speed ω_{rot}. During rotation the effective deposition time t is equal for the two targets and depends of ω_{rot} and of the sputtering tool geometry. In our case, the diameter of the substrate holder D is 80 cm and the diameter of the target d is 10 cm, thus:

$$t = \frac{d \times \omega_{rot}}{\pi \times D} = 0.04 \times \omega_{rot} \tag{3.35}$$

These films were deposited on small silicon samples (4 x 1 cm^2).

During the first set of experiments, only the CGO and Ni deposition times were varied in order to obtain the optimal microstructure. In some cases the substrate was rotated over the targets at the speed of 6 rpm. All the parameters for this set of depositions are reported in Table 12:

Table 12: Deposition conditions for composite Ni-CGO films.

Press. [mT]	**Ar flow [sccm]**	**RF power CGO [W]**	**DC power Ni [W]**	**Temperature [°C]**	**Rot. speed [rpm]**	**Time A-B [min]**	**Dist. T-S [mm]**
50	30	100	50	25	6	1-60	100

The different obtained morphologies were studied by SEM cross-section and surface images. All these results are reported in Figure 37 according to the CGO and Ni deposition time. As the nickel deposition rate τ_{Ni} (in nm/min) is higher than the rate of CGO τ_{CGO}, the composition, in volumic percent of CGO c_{CGO} or of Ni c_{Ni}, of the film not only depends on the respective deposition times:

$$c_{CGO} = 1 - c_{Ni} = \tau_{CGO} \times t_{CGO} = 1 - (\tau_{Ni} \times t_{CGO}) \tag{3.36}$$

The rate of deposition of the film τ_{Ni} is equal to:

$$\tau_{film} = \tau_{CGO} \times t_{CGO} + \tau_{Ni} \times t_{Ni} \tag{3.37}$$

And when the substrate is rotating at a speed ω the rate of film deposition is given by:

$$\tau_{film} = 0.04 \times \omega_{rot} \times (\tau_{Ni} + \tau_{CGO}) \tag{3.38}$$

With the parameters given in Table 12, the rate of the CGO deposition was of 1-2 nm/min and the rate of nickel was of 15 nm/min. At the end of this paragraph, it will be shown how it is possible to control the composition of the film by increasing the power applied to the CGO target. Obviously, the pure nickel films were the thickest for a given deposition time. These films grow with a columnar porous microstructure, which appears only after some tens of nanometres. As shown in the simulations of Enomoto and Taguchi [33], the porosity increases with time of deposition for columnar growth. In this model a transient behaviour between a flat growth and columnar growth has been elucidated by introducing two basic parameters:

- The sticking coefficient B of incoming atoms to the growing film

- The coefficient of surface diffusion A of adatoms on the film

When A decreases or B increases the film tend to form a columnar microstructure because the adatoms are almost immobile after they hit the surface and cannot rearrange themselves. To obtain porous films, a high argon pressure of 50 mT and room temperature were used in order to reduce the energy of incident atoms. Thus there is little adatom mobility on the surface of the film and therefore the grains tend to grow in the direction of the available coating flux [34]. This low mobility also favours the creation of voids in place of grain boundaries and, at high deposition rates, this effect is further increased by the grain self-shadowing that tends to disturb the growth [35]. Thus, the size of the pores increases through the thickness of the film even if they are not present at the beginning of the growth as seen in Figure 36.

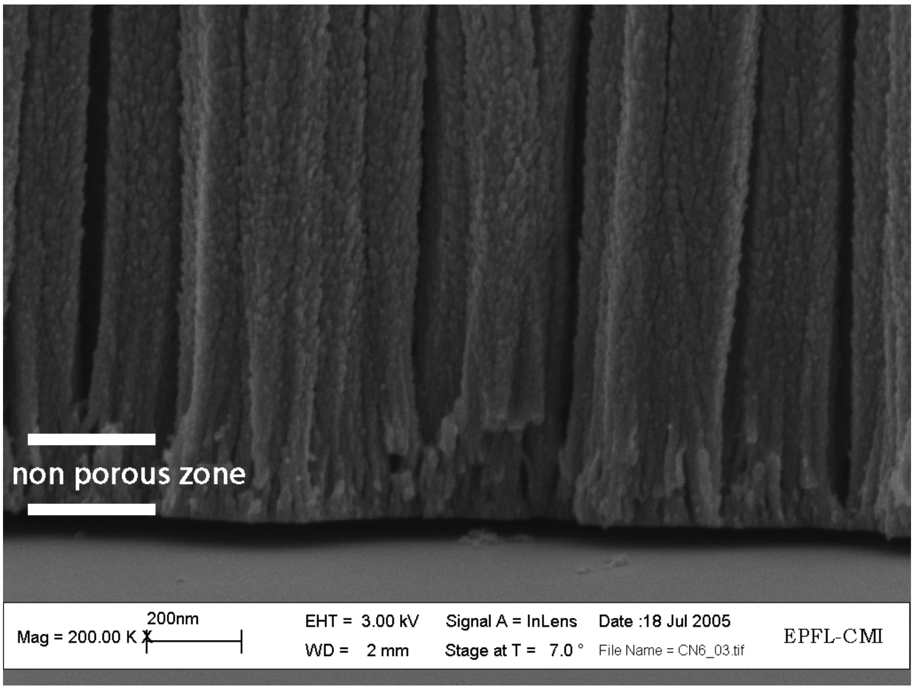

Figure 36: Deposition of pure nickel. At the beginning of the growth a non porous zone is formed. After ~150 nm, the pores appears at grain boundaries and their size increases through the layer.

When the CGO deposition time is sufficient, an intermediate CGO layer is formed between two consecutive nickel layers as seen in Figure 39, Figure 41 and Figure 43. Hence, the nickel columnar growth is stopped and the films show a lamellar structure. Thus the porosity that appears only after several tens of nanometres is reduced as seen in Figure 40 compared to Figure 43. Within these films, the CGO deposition time was sufficient to form a thin continuous ceramic layer on the nickel and to stop the columnar growth. As the rate of CGO deposition is lower, the microstructure is less disturbed and smoother. Consequently the pure CGO film shows a dense columnar microstructure without any porosity as in the Figure 44. Nevertheless, when the nickel and CGO deposition times are sufficient, it is possible to grow a lamellar structure with some porosity as the pores appear in the nickel layer when it is sufficiently thick (Figure 43).

Figure 37 summarizes all the observations made in this chapter. When the nickel deposition time is sufficient over approximately 4 minutes, the films are porous even for high CGO deposition time (top of the graph). When the CGO time is above 2 minutes, the structure is columnar and porous (left of the graph). The lamellar structure appears when the CGO deposition time is sufficient compared to Ni time (bottom right of the graph). A continuous line indicates the zone where the nickel and CGO time are equal. The deposition made at 6 rpm is on the bottom of this line, at this speed the CGO cannot form a continuous layer on the nickel and the microstructure is porous and non lamellar. For long CGO deposition times compared to nickel, the films are dense and non lamellar (bottom right of the graph). The SEM images showing the different type of microstructure are given below.

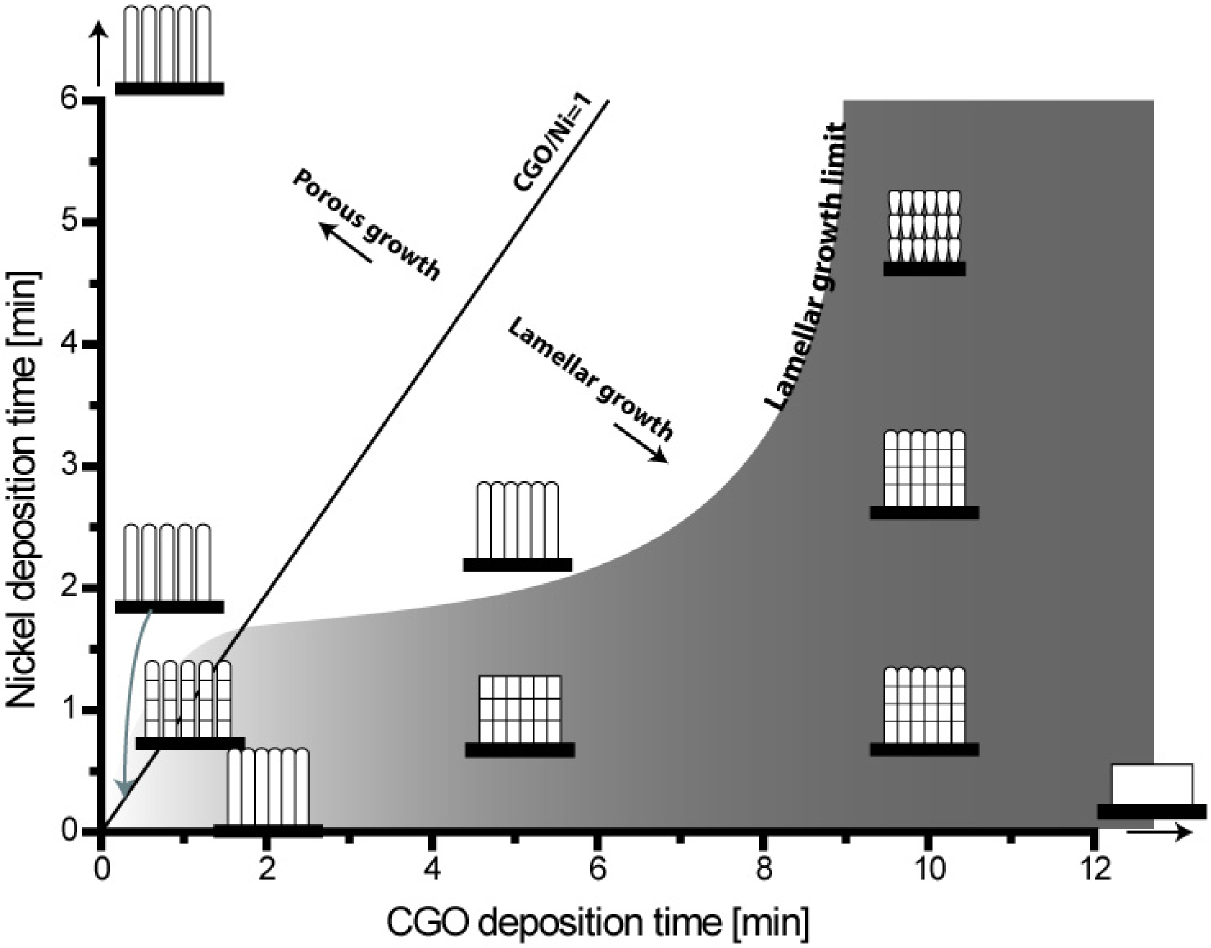

Figure 37: Microstructure of the Ni-CGO composite thin films in function of the CGO and nickel deposition times.

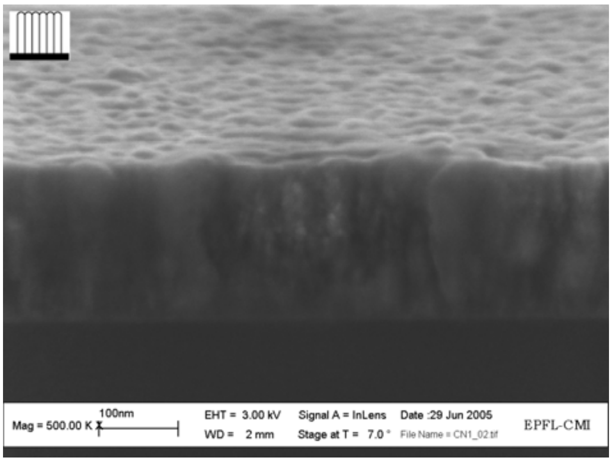

Figure 38: Deposition with 5 min CGO and 2.5 min Ni

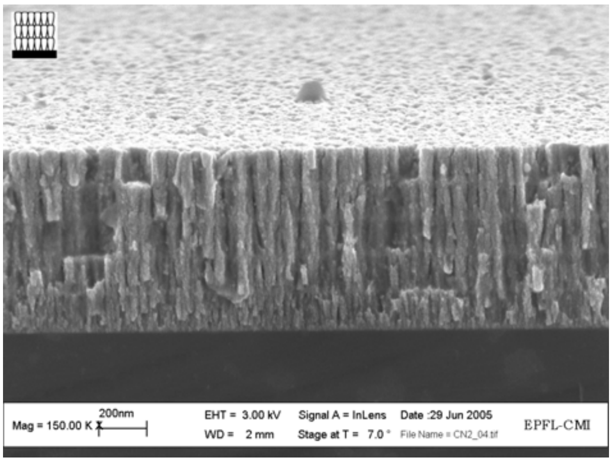

Figure 39: Deposition with 10 min CGO and 5 min Ni

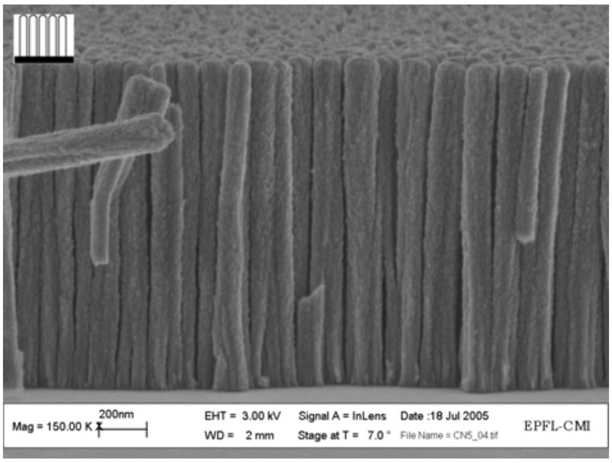

Figure 40: Deposition of pure Ni (60 min)

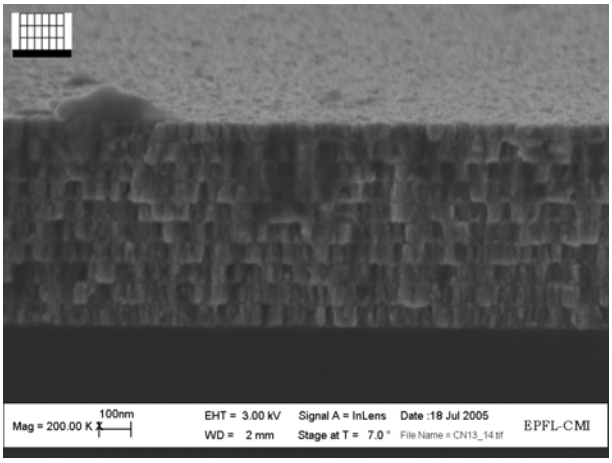

Figure 41: Deposition with 5 min CGO and 1 min Ni

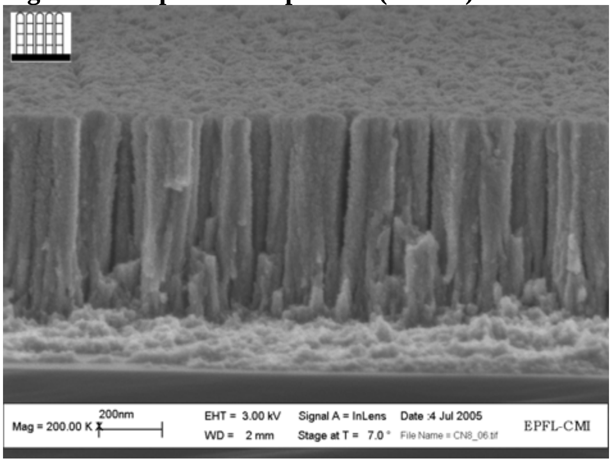

Figure 42: Deposition at rotating speed of 6 rpm

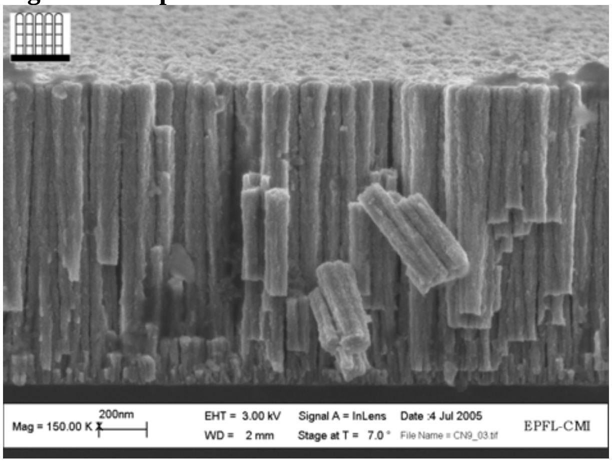

Figure 43: Deposition with 1 min CGO and 1 min Ni

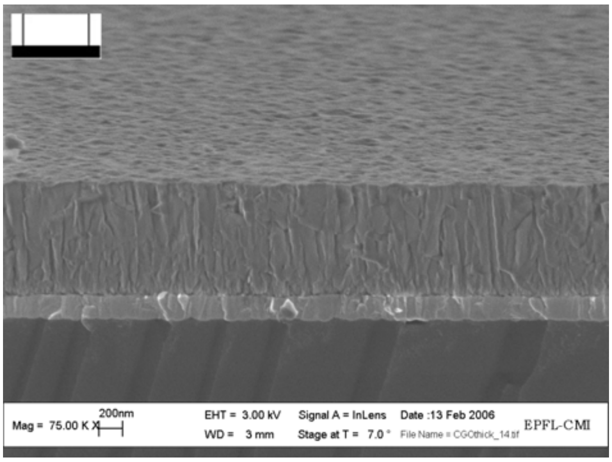

Figure 44: Deposition of pure CGO (60 min.) on Pt.

3.5.2. Study of the composition of porous composite CGO-Ni thin films

The CGO-Ni film composition was investigated by changing the power applied on the two different targets or by covering a part of the CGO target with a Ni foil. The surface covered by the foil is a band passing through the centre of the CGO metallic target and covering 5% or 15% of the target total surface. All the films were sputtered on silicon small samples (4 x 1 cm^2) covered by 1 µm of SiO_2 grown by wet oxidation.

First, the influence of the power applied on the CGO metallic target on the composition was evaluated. These samples were deposited at room temperature with a 200 W RF bias on the nickel target and a pulsed DC bias applied to the CGO metallic target as shown in the Table 13. During the depositions the substrate was rotated over the two targets at a speed of 6 rpm.

Table 13: Deposition conditions for the second set of Ni-CGO composite thin films.

	Press. [mT]	**Ar flow [sccm]**	**O_2 flow [sccm]**	**RF power Ni [W]**	**DC power CG met [W]**	**Temp. [°C]**	**Rot. speed [rpm]**	**Dep. time [min]**	**Dist. T-S [mm]**
A	50	20	20	200	75	25	6	120	100
B	50	20	20	200	100	25	6	120	100
C	50	20	20	200	150	25	6	120	100
D	50	20	20	200	200	25	6	120	100

In this case, the DC bias was applied to the CGO metallic target to improve the rate of deposition of the CGO compared to the rate of Ni. To avoid sparks onto the CGO target the field was applied by pulses using a Spark. This method is often used to deposit aluminium nitride films from a metallic Al target [36, 37].

As shown the %at. of CGO in the films increases with the applied power on the CGO target. Between 100W and 150W the CGO content increases drastically from 6 at% to 60 at%. This regime should be elucidated more carefully as the ideal composition for CGO/Ni anodes is of 30%. Nevertheless, this work proves that the composition can be tuned by adjusting the applied power on the CGO metallic target.

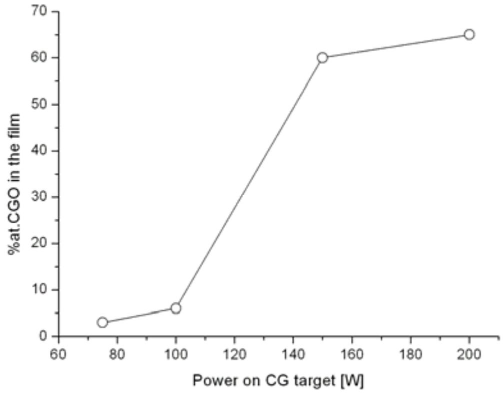

Figure 45: Ni-CGO composite thin film composition (in %at. of CGO) related to the power applied on the CGO metallic target.

In a second time, the composition of the films was investigated by depositing Ni/CGO films from the CGO metallic target partially covered by a thin Ni foil. In this case, the substrate is static and the rate of deposition is better than with the previous rotating method. The film composition and the schematic coverage of the CGO target by the Ni foil are given in Figure 46. To obtain 30 at%. of CGO in the film, the Ni foil should be placed on the border of the CGO metallic target and cover 8% of the total target surface. Theses results also show that the plasma is not homogenous, mainly because of the magnetron, and that the film content thus also depends on the position of the nickel foil. The Ni at%. in the film can be reduced by decreasing the size of the foil or by moving it away from the centre of the target where the sample is placed.

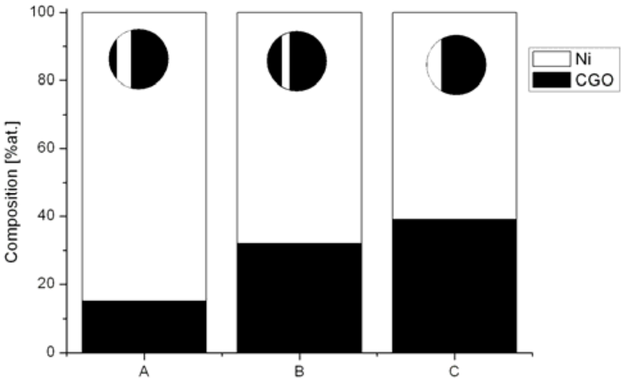

Figure 46: Composition of the Ni-CGO film (in %at.) according to the position and surface of the Ni foil placed onto the CGO metallic target. A) Ni foil at 1.9 cm of the target centre with a thickness of 2 cm, B) foil at 1.9 cm of the target centre with a thickness of 1 cm and C) foil at 4.5 cm of the target centre with a thickness of 1 cm.

3.5.3. Electrical characterization of the Ni-CGO thin films

The Ni-CGO films were deposited on silicon 4 x 1 cm^2 samples covered with a 1 μm thick wet oxide layer with parameter given in Figure 46 (sample B). The thin film contains 30% of CGO and 70° of nickel. The DC conductivity was measured in the furnace in pure argon as explained in 3.1.3.1. Platinum electrodes (100 nm thick) were sputtered in the Nordiko with parameters given in Table 5 at both ends of the sample. The conductivity of Ni-CGO layers was measured in the plane of the film between the two electrodes separated by 1 mm. The platinum wires used for the contact were attached on the Pt electrodes with a commercial Pt paste. Then the paste was sintered at 500°C during 1 hour. Figure 47 shows the Arrehnius plot of the conductivity. As for ionic conductors the conductivity increases with the temperature and has a activation energy of 0.7 eV during heating and 0.5 eV during cooling. In this case, the activation energy is required for the electrons to pass from the nickel conduction band to the one of CGO. The maximal conductivity at 700°C is of 12 x 10^3 S/m. The large conduction during cool down can be possibly ascribed to the reduction of CGO.

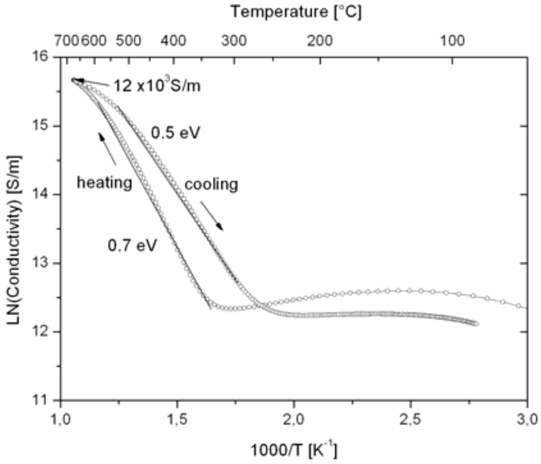

Figure 47: Arrhenius plot of the in-plane conductivity of a Ni-CGO film measured in pure Ar.

3.6. Porous platinum electrodes

3.6.1. Growth conditions and microstructure characterization

Porous platinum films were deposited from a commercial Pt target (4” diameter and 1 mm thickness) from Goodfellow. These films were deposited at high pressure and with the substrate holder rotating at 6 rpm. This set of films is deposited on small silicon samples (4 x 1 cm^2) covered by 1 μm of SiO_2 grown by wet oxidation. The conditions of deposition are reported in Table 14.

Table 14: Deposition conditions for the porous Pt films.

Press. [mT]	Ar flow [sccm]	O_2 flow [sccm]	DC power [W]	Rot. speed [rpm]	Temperature [°C]	Rate [nm/min]	Dist. T-S. [mm]
100	50	0	100	6	25	?	100

As for Ni/CGO composite film the porosity was enhanced by reducing the mobility of the adatoms onto the film surface. The temperature of the substrate was kept to 25°C and the Ar pressure was high (100 mT) to reduce mean free path of ions in the plasma and thus their remaining energy at the surface of the film. With a low impact energy it is possible to avoid backscattering of ions and reduce their mobility on the surface. As explained by Enomoto and Taguchi [33] and already depicted in the paragraph 3.5.1, these parameters favour a columnar and porous microstructure as shown in Figure 48:

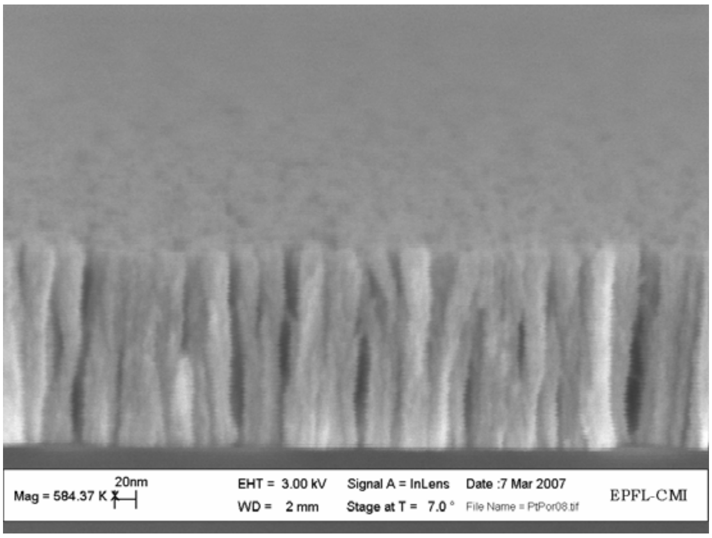

Figure 48: Cross section view of the porous platinum deposited on silicon

3.7. Summary

YSZ thin films were deposited by means of reactive magnetron sputtering onto bare, oxidized, and platinized silicon substrates at 530°C. The films were dense and crack free, and (111)-textured, also on amorphous silicon oxide the films. By applying a bias to the substrate and by decreasing its temperature to 20°C, it was possible to form (200) porous and nanocrystalline YSZ even on the YSZ(111) dense layer. Two and three layer YSZ stacks ((111)/(200) or (111)/(200)/(111)) have been deposited. The columnar grain boundaries of the (111) layer are interrupted at the interface between two consecutive layers. This microstructure is used to avoid electrical leakage due to grain boundary conduction through the electrolyte.

The ionic conductivity across YSZ films was measured as a function of temperature in air. At 500°C the conductivity amounts to 5.5×10^{-3} S/m, and is thus sufficient for SOFC operation. The activation energy was measured as 0.92 eV, a value that is slightly smaller than reported in literature for 8YSZ.

During annealing in air, the mechanical stress of (111) YSZ thin shows very strong anomalies. It was possible to explain these by variable oxygen vacancy concentrations. After deposition at 500°C, during cooling in reduced oxygen pressure, oxygen vacancies are created resulting in a compressive stress. When the films are post-annealed in air up to 700°C, the vacancies are filled by oxygen ions and the volume of the film is reduced. Thus the annealing permits to annihilate the compressive stress due to vacancies. It was found that this process is diffusion limited, thus controlled by the diffusion of oxygen ions into the film and not by oxygen up-take at its surface. The activation energy for the diffusion of 0.6 eV during this process is smaller than the energy derived from ionic conductivity measurements. We propose that the reduction in the process chamber leads to a kind of "free" oxygen vacancies compensated by electron charges, and not by dopant cations, as is the case for the vacancies intentionally stabilized by Y^{+3} doping. The additional, free vacancies are much more mobile than the ones paired with cationic defects. Such a behavior was predicted in the literature. During stress measurement, the concentration of vacancies trapped by Y^{3+} does not change, and thus does not affect the stress. Stress measurements thus allow to assess the free vacancies with their lower activation energy. Conductivity measurements during the first heating cycle revealed an anomaly that could be well ascribed to a space charge effect induced by the free vacancies. Finally, after an annealing in air, the YSZ films have low stress at room temperature, and resist better to thermal cycling.

The ionic conductivity of the CGO has been measured as a function of temperature in air. At 500°C the conductivity is of 0.5 S/m and sufficient for SOFC operation. The activation energy of 1.2 eV is slightly smaller than the literature value. The ability of the Ce ions to be reduced from +IV to +III causes electronic leakage in thin CGO films. For this reason, CGO was replaced by YSZ even though its ionic conduction is lower.

CGO thin films were deposited by means of reactive magnetron sputtering onto different substrates at different temperature (20°C and 430°C) and gas conditions (Ar or Ar and O2). XRD analysis shows that the films are mostly (111) textured on platinum when deposited at high temperature. A loss of Ce during the deposition process has been found by EDAX analysis. To compensate this deficiency, a target with an excess of Ce has been used and provides films with the good stochiometry. The stress behaviour of the CGO films has been studied as a function of temperature. As in YSZ, the as-deposited films contain free oxygen vacancies, but in contrast to YSZ, these ones are trapped near Ce^{3+} defects.

The growth of Ni-CGO films by co-sputtering from a nickel and a CGO target has also been studied. It was possible to obtain columnar porous films with various compositions. These films can be used later as the anode in a μSOFC.

LSC dense cathode and porous platinum electrodes have also been studied for use in μSOFCs.

3.8. References

1. Ohring, M., *Materials science of thin films: Deposition and structure*. 2002, San Diego: Academic Press.
2. Hertz, J.L. and H.L. Tuller, *Electrochemical Characterization of Thin Films for a Micro-Solid Oxide Fuel Cell.* Journal of Electroceramics, 2004. **13**: p. 663-668.
3. Laffez, P., et al., *Growth of La2Mo2O9 films on porous Al 2O3 substrates by radio frequency magnetron sputtering.* Thin Solid Films, 2006. **500**(1-2): p. 27-33.
4. Yoo, Y., *Fabrication and characterization of thin film electrolytes deposited by RF magnetron sputtering for low temperature solid oxide fuel cells.* Journal of Power Sources, 2006. **160**: p. 202-206.
5. Tsai, T. and S.A. Barnett, *Bias sputter deposition of dense yttria-stabilized zirconia films on porous substrates.* Journal of vacuum science and technology A, 1995. **13**: p. 1073-1077.
6. Nagata, A. and H. Okayama, *Characterization of solid oxide fuel cell device having a three-layer film structure grown by RF magnetron sputtering.* Vacuum, 2002. **66**: p. 523-529.
7. LaO, G.J., et al., *Microstructural features of RF-sputtered SOFC anode and electrolyte materials.* Journal of Electroceramics, 2004. **13**: p. 691-695.
8. Hiboux, S. and P. Muralt, *Mixed titania-lead oxide seed layers for PZT growth in Pt(111): a study on nucleation, texture and properties.* Journal of the European Ceramic Society, 2004. **24**: p. 1593-1596.
9. Steele, B.C.H. and A. Heinzel, *Materials for fuel-cell technologies.* Nature, 2001. **414**: p. 345-352.
10. Ruddell, D.E., B.R. Stoner, and J.Y. Thomspon, *Effect of deposition interruption and substrate bias on the structure of sputter-deposited yttria-stabilized zirconia thin films.* Journal of Vacuum science and technology A, 2002. **20**(5): p. 1744-1748.
11. *CRC Handbook of Chemistry and Physics*. 75th ed, ed. D.R. Lide. 1994, London: CRC Press.
12. Ingel, R.P. and D.L. III, *Errors in elastic constant measurments in single crystals.* Journal of the American Ceramic Society, 1988. **71**(4): p. 261-264.
13. Roth, W.L., et al., *Structure of additives in ß''-alumina and zirconia superionic conductors.* Solid State Ionics, 1985. **18-19**: p. 1115-1119.
14. Yamamura, Y., S. Kawasaki, and H. Sakai, *Molecular dynamics analysis of ionic conduction mechanism in yttria-stabilized zirconia.* Solid State Ionics, 1999. **126**: p. 181-189.
15. Cormack, A.N., *Mass transport in anion deficient fluorite oxides.* Materials Science Forum, 1986. **7**: p. 177-186.

16. Atkinson, A., *Chemically-induced stresses in gadolinium-doped ceria solid oxide fuel cell electrolytes.* Solid State Ionics, 1997. **95**: p. 249-258.
17. Lubomirsky, I., *Mechanical properties and defect chemistry.* Solid State Ionics, 2006. **177**: p. 1639-1642.
18. Li, X. and B. Hafskjold, *Molecular dynamics simulations of yttrium-stabilized zirconia.* Journal of Physics: Condensed Matter, 1995. **7**: p. 1255-1271.
19. Quinn, D.J., *Microstrucuture, residual stress and mechanical properties of thin materials for a microfabricated solid oxide fuel cell.* 2006, Massachusetts Institute of Technology: Boston.
20. Ochando, I.M., et al., *Influence of the yttria content on the mechanical properties of Y2O3-ZrO2 thin films prepared by EB-PVD.* Vacuum, 2007. **81**: p. 1457-1461.
21. Greenberg, M., et al., *Elasticity of solids with a large concentration of point defects.* Advanced Functional Materials, 2006. **16**: p. 48-52.
22. Infortuna, A., A.S. Harvey, and L.J. Gauckler, *Microstructures of CGO and YSZ thin films by pulsed laser deposition.* Advanced Functional Materials, 2008. **18**: p. 127-135.
23. Harris, G.B., *Quantitative measurements of preferred orientation in rolled uranium bars.* Philosophy Magazine, 1952. **43**: p. 113-123.
24. Atkinson, A. and T.M.G.M. Ramos, *Chemically-induced stresse in ceramic oxygen ion-conducting membranes.* Solid State Ionics, 2000. **129**: p. 259-269.
25. Wang, S., et al., *Nonstoichiometry of Ce0.8Gd0.2O1.9-x.* Journal of the Electrochemical Society, 1997. **144**: p. 4076-4080.
26. Rupp, J.L.M., A. Infortuna, and L.J. Gauckler, *Thermodynamic stability of gadolinia-doped ceria thin film electrolytes for micro-solid oxide fuel cells.* Journal of the American Ceramic Society, 2007. **90**(6): p. 1792-1797.
27. Sanderson, R.T., *Chemical Periodicity*. Physical and inorganic chemistry textbook series, ed. Reinhold. 1960, New York: Chapman & Hall.
28. Wang, Y., et al., *The effect of oxygen vacancy concentration on the elastic modulus of florite-structured oxides.* Solid State Ionics, 2007. **178**: p. 53-58.
29. Doshi, R., et al., *Development of Solid-Oxide Fuel Cells That Operate at 500°C.* Journal of Electrochemical Society, 1999. **146**(4): p. 1273-1278.
30. Steele, B.C.H., *Appraisal of Ce1-yGdyO2-y/2 electrolytes for IT-SOFC operation at 500°C.* Solid State Ionics, 2000. **129**: p. 95-110.
31. Gauckler, L.J., et al., *Solide Oxide Fuel Cells: Systems and Materials.* Chimia, 2004. **58**(12): p. 837-850.
32. Masumoto, H., S. Hiboux, and P. Muralt, *Preparation of La1-xSrxCoO3 electrodes for ferroelectric thin films by RF magnetron sputtering.* Ferroelectrics, 1999. **225**: p. 335-341.
33. Enomoto, Y. and M. Taguchi, *Modelling of columnar growth continuum ballistic deposition.* Applied Surface Science, 2005. **244**: p. 213-216.

34. Thornton, J.A., *Influence of apparatus geometry and deposition conditions on the structure and topography of thick sputtered coatings.* Journal of vacuum science and technology A, 1974. **11**(4): p. 666-670.

35. Karabacak, T., et al., *Scaling during shadowin growth of isolated nanocolumns.* Physical Review B, 2003. **68**: p. 125408-1-5.

36. Dubois, M.-A. and P. Muralt, *Properties of Aluminium nitride thin films for piezoelectric transducers and microwave filter applications.* Appl. Phys. Lett., 1999. **4**(20): p. 3032-3034.

37. Lanz, R., M.-A. Dubois, and P. Muralt. *Solidly mounted BAW filters for the 6 to 8 GHz range based on AlN thin film*. in *IEEE Ultrason. Symp. Proc.* 2001.

μSOFC fabrication and characterization

4.1. Discussion of the constraints related to the fabrication of µSOFCs

As already discussed in chapter 2, the mechanical stability of the electrolyte is of primary concern. In addition, the electrolyte should be free of gas leaks. In this section, such issues are discussed in relation with the microfabrication and thin films deposition techniques.

4.1.1. The role of the nickel grid

The best possible µSOFC membrane has to satisfy at the same time two conflicting conditions: On the one hand its diameter should be relatively large - i.e. in the mm to cm range - and on the other hand should by rather thin to reduce ionic resistance and operation temperature. Due to the large thermal expansion mismatch between YSZ and silicon of approximately 7 ppm/K, the thickness of a free standing membrane with a surface of 1 mm^2 should reach at least 50 µm [1], or else some support is needed to avoid buckling. [2]. In this work, it was decided to support the membrane with a nickel grid. The choice of nickel was made based on the convenient growth process by electroplating, which allows for a selective deposition within a resist mould, and for obtaining thicker films than by other methods. In addition, it is cheaper and easy to be up-scaled. Another advantage of the nickel is that it has been used for many years as a material for the anode of SOFCs [3]. Finally the thermal expansion coefficient of nickel (13 ppm/K [4]) is much better matched to the one of YSZ (10 ppm/K).

In order to successfully develop a fabrication concept, a hierarchy of important requirements needs to be established. A very stringent condition can be derived for the deposition of the electrolyte layer. This one is not only very thin, but should also be free of cracks and pores. As a consequence, this layer must be deposited on a flat and pore free surface, especially if physical deposition techniques are used (sputtering, PLD, evaporation). CVD techniques may accept somewhat less strict conditions. In any case, a polished wafer surface is a very good starting point for the deposition of the electrolyte layer. This approach implies, however, that the supporting structure must be mounted on top of the electrolyte layer (which is contrast to earlier work and patents [1-9]). Alternatively, one could apply a chemical-mechanical polishing step after moulding a reinforcement structure into a substrate, and then deposit the electrolyte layer. This procedure is not only more expensive, it would also restrict the temperature of the oxygen anneal after electrolyte deposition in case nickel is used as supporting structure. For these reasons we thus pursued the approach according to the criteria:

1) Profit from smooth wafer to deposit dense and crack free electrolyte layer
2) Apply nickel grid after all high temperature oxygen anneals are done

This approach resulted in the design as given in Figure 1. Nevertheless, one compromise needed to be done: Since we wanted to have the cathode contact on the same side as the anode contact, a patterned cathode needs to be deposited before the electrolyte layer. Hence at least at one side of the membrane, there is a step where the continuous cathode contact layer ends (to the left in Figure 1). As further explained in the following, there are additional variants:

1) The cathode contact layer may also form a mesh as current collector below the electrolyte (as in Figure 1).
2) A thermal oxide layer is introduced between silicon and cathode to avoid conduction through the silicon.
3) A continuous mixed conducting cathode layer is introduced below the electrolyte layer.

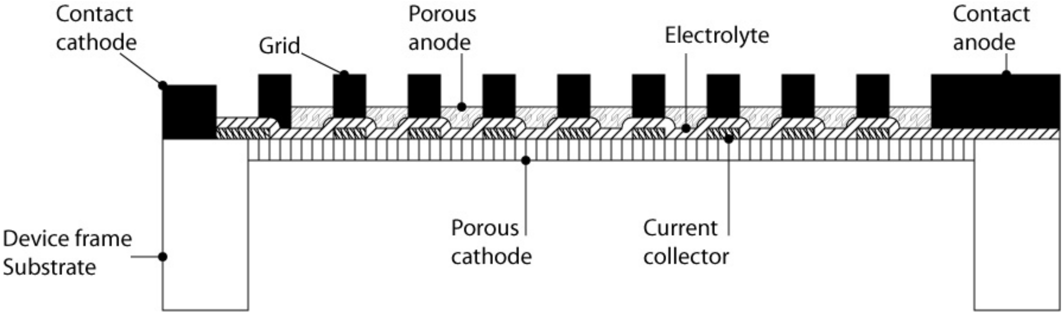

Figure 1: Cross section scheme of the μSOFC.

The porous electrodes are deposited at the end of the process after the membranes have been released. In this case the advantage of having a very large membrane aperture is clear. Albeit the hole in the Si is 380 μm deep, large aperture permits to sputter the porous cathode directly on the electrolyte from the backside.

To measure the voltage of the cell, electrical contacts are required. For they are made of metals, it was decided to place them on the anode side, where no oxidation takes place. This construction requires a via in the PEN to reach the cathode contacts. Since the electrolyte was difficult to etch and since the large dimensions of the cell do not require a critical alignment of the cathode contact, the electrolyte was deposited through a shadow mask covering the contact cathode area.

First grids were designed with a hexagonal pattern. The side dimension of the hexagon was 50 μm long, the diameter was 100 μm and the grid's linewidth was of 5 μm. After the releasing of the membrane by Si dry etching, the electrolyte usually shows some strain at the border of the silicon hole, as can be seen in Figure 2:

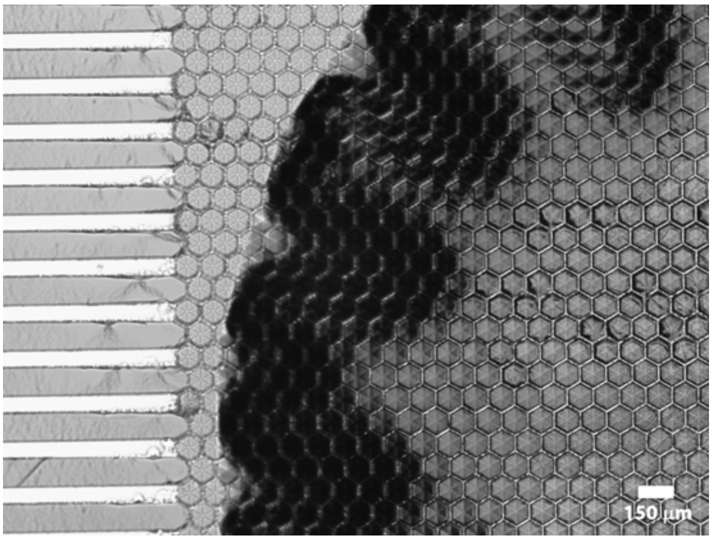

Figure 2: View of the strain near the border of a membrane supported by an hexagonal Ni grid.

As seen in Figure 3, the hexagonal nickel grid can support all the layers comprised in the PEN stack. The grid also adapts its shape to the strain at the border of the silicon hole. Albeit the nickel grid is very ductile, the large strains near the border of the silicon hole created some cracks in the electrolyte in less than 5% of the grid cells.

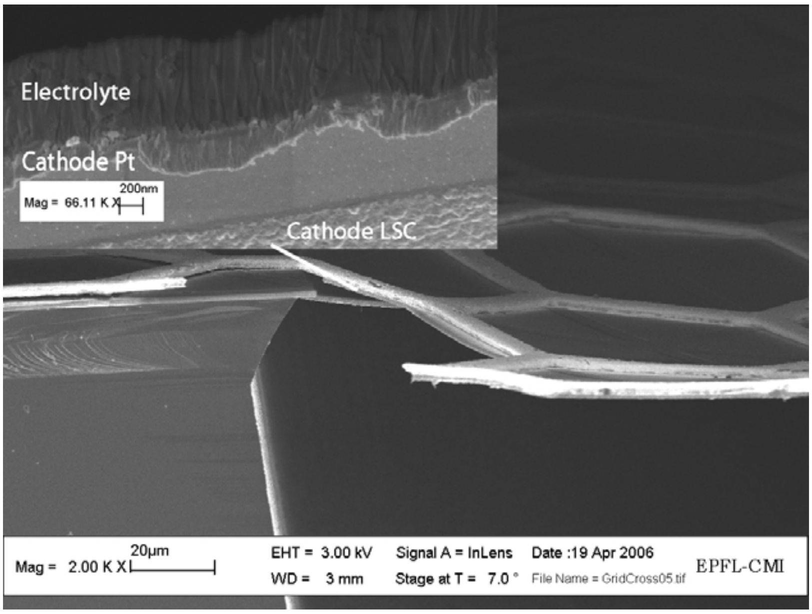

Figure 3: SEM cross view of the nickel supporting the electrolyte, a Pt current collector and a LSC cathode (top left).

To minimize this effect, a spiderweb pattern was chosen in accordance to the central symmetry of the silicon hole. The cell dimensions are critical to prevent formation of cracks due to the thermal stress. The grid is made of concentric circles of increasing diameter. The circle radius is increased in steps of 50 µm as shown in Figure 4. The number of radial intersections is increased with the diameter of the circles in order to keep the size of the outer arc of the cell below 90 µm. An outer ring made of nickel covers the border of the silicon hole, thus avoiding the buckling of the electrolyte at this place. This ring is 200 μm wide. For a 500 nm thick membrane the maximal aperture should be of 15 μm according to the equation 2.3. But this calculation applied to flat membranes and the nickel grid steps increase the maximal aperture by a factor 150 [10]. Thus, a maximal aperture of 90 μm is relatively conservative.

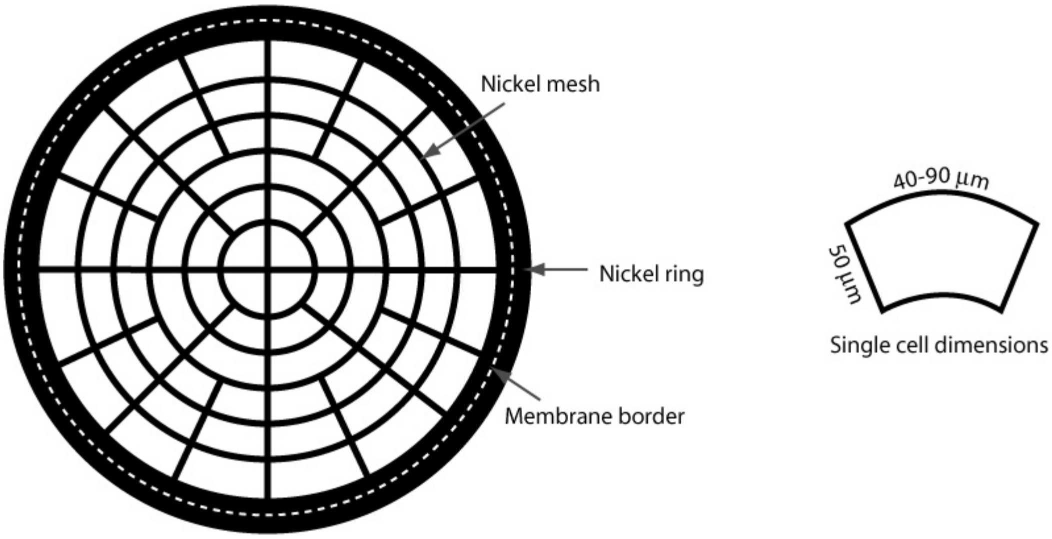

Figure 4: Schematic view of the spider web nickel grid.

Optical profilometry analysis shows that the thickness of the grid is relatively constant on the scale of a cell as seen in Figure 5, but variations of 30% are observed across the wafer. This difference is due to the non-uniform the electrical current distribution over the wafer and can be corrected by a more careful study of the platinum wire design.

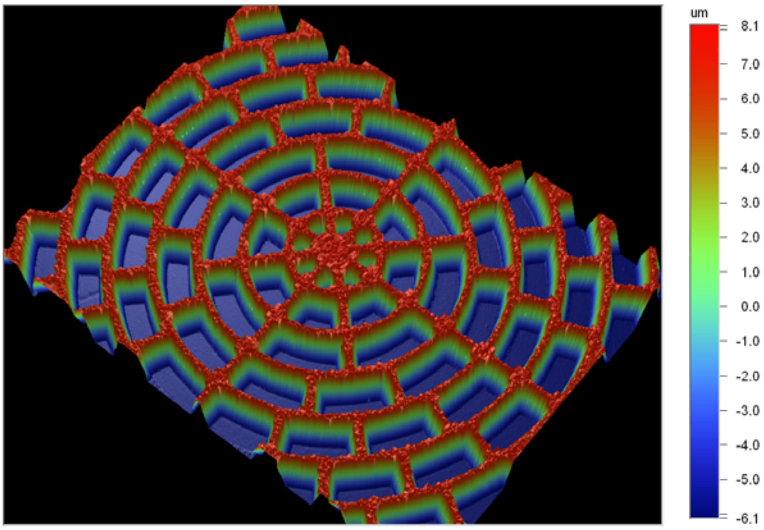

Figure 5: Profile of the large spiderweb nickel grid

A cross section of the nickel grid supporting the electrolyte has been obtained by cutting the sample with a focused ion beam (Nova 600 Nanolab from FEI). Figure 6 obtained with gallium ions, shows the trapezoidal shape of the nickel grid section. This particular shape is due to the photoresist (S1818 from Shipley) mould that yields inclined walls. The electrolyte surface covered by the nickel is smaller than the mean section of the grid, thus the structure is stronger than if its walls were vertical. The only disadvantage of this shape is that, during the deposition of a porous anode, some parts of the electrolyte will not be covered and thus the total TPB will be slightly reduced. Some artefacts due to the redeposition of the etched material are seen on the nickel grid sides and on the electrolyte. The ion milling also renders the nickel surface rougher as seen on the upper surface of the grid. The contrast obtained with the ion beam shows the structure of the nickel grains. At the beginning of the growth a mushy zone with smaller grains is formed. Then the grains grow and form columns that are oriented along the radii of the grid section.

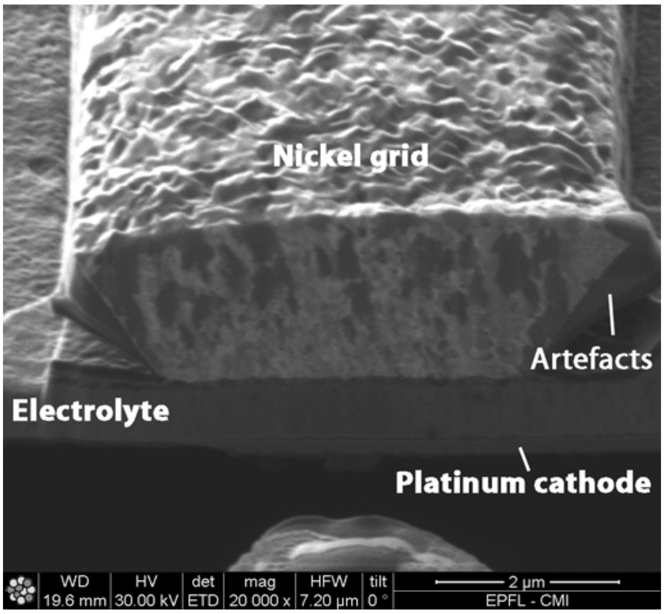

Figure 6: Image of the nickel grid cross section obtained with the Ga ions, after cut of the sample with FIB.

4.1.2. Influence of the electrode microstructure on the electrolyte resistance

The power of the cell is mainly dependant on the ohmic losses occurring in the electrolyte and in the electrodes as seen in paragraph 1.4.4. In the simplest case, the resistance of the electrolyte R_{ode} is proportional to the ratio of its thickness h and its ionic conductivity σ_{ion}. In this case, it is considered that the surface of the electrolyte is homogeneously active and this assumption is generally true for thick electrolytes. In the case of thin films, the microstructure of the electrodes has a very important effect on the electrolyte resistance. The density of triple phase line and the capacity of the electrodes to conduct oxygen ions can improve the conductivity. At 500°C, the diffusion length in YSZ is limited to the regions where ions can diffuse from the cathode to the anode. If the particles of the electrode have a diameter d and are separated by a distance b larger than the diffusion length, the active surface of the electrode is reduced and its resistance increases. Figure 7 shows the diffusion path through the electrolyte for different particle type and distribution:

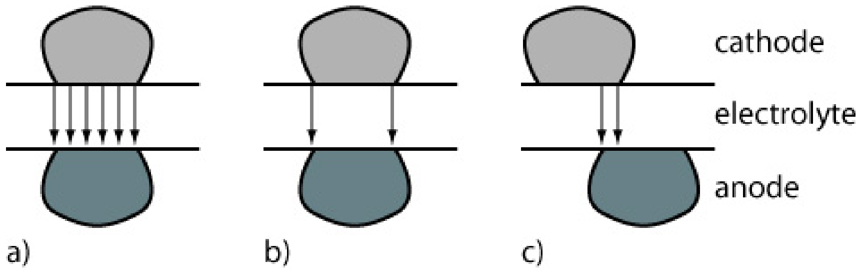

Figure 7: Diffusion path trough the electrolyte for different types of electrodes. a) both electrodes are ionic conductors and well aligned, b) electrodes only conducts electrons and c) electrodes conduct ions but are not well aligned.

This situation can be modeled simply by the following equation given by Fleig [11]:

$$R_{ode} = \frac{h}{\sigma_{ion}} + \frac{b}{\sigma_{ion}} \left(\frac{\frac{b}{d} - 1}{\frac{d}{b} + 1} \right) \tag{4.1}$$

This model is only valid for particles that are homogenously sized and distributed over the whole membrane. The simulated curves in Figure 8 show that the fineness of the microstructure is only important for a given thickness of the electrolyte h_{crit}:

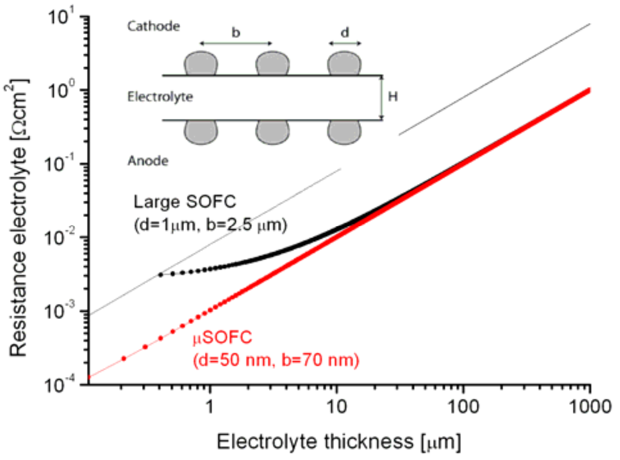

Figure 8: Resistance of the electrolyte versus thickness for different electrode morphologies.

Thus for µSOFCs with electrolyte thickness under 500 nm, it is important to work with fine-grained electrodes to avoid resistive losses. With thick electrolytes such as in large SOFCs, there is no advantage of having a very fine microstructure as the resistance only depends on h and is proportional to h/σ_{ion}. For small values of h the resistance reaches a threshold equal to:

$$\lim_{h \to 0} R_{ode} = \frac{b^2(b-d)}{d(b+d)\sigma_{ion}} = \frac{h_{crit}}{\sigma_{ion}} \tag{4.2}$$

This limit gives the value of *h* at which the behavior of the resistance starts to depend on the microstructure of the electrode:

$$h_{crit} = \frac{b^2(b-d)}{d(b+d)} \tag{4.3}$$

For thin film electrolyte with (h = 500nm), the resistance of the electrolyte starts to deviate from the linear law when $b=2d=750$ nm. Thus in 500 nm thick electrolytes, grain size of electrode in the range of hundreds of nanometer are very favorable. On the contrary, for thick self-supported electrolytes SOFC (h > 150 µm [12]), a fine particle size is not required. In the case of µSOFC, h is in the micrometer range thus the parameters b and d can affect the resistance very much and in this case it is better to have a particle size in the nanometer range. The coverage of the electrolyte also plays an important role. As shown in Figure 9, the electrolyte resistance, for an electrolyte thickness of 500 nm and a distance of 150 nm between the particles, decreases drastically when the coverage increase from 15 % to 40 % (i.e. when d goes from $0.15\ b$ to $0.4\ b$):

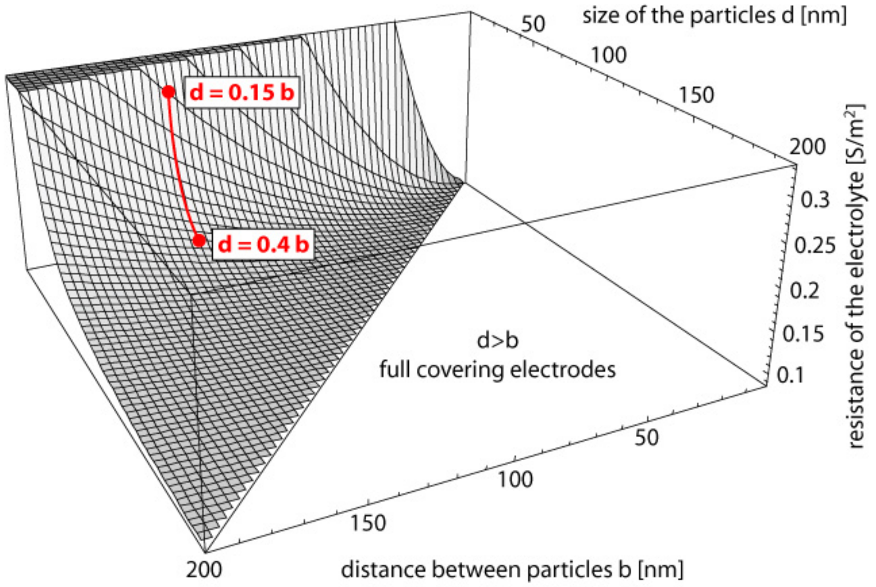

Figure 9: Electrolyte resistance for an electrolyte thickness of 500 nm versus the microstructure of the electrode characterized by the distance between the particles *b* and their size *d*.

For the µSOFCs fabricated during this work, porous platinum electrodes as described in the paragraph 3.6, were used to enhance the TPB length and thus reduce the cell resistance. These platinum electrodes have a mean grain size d_{pt} of 20 nm and the grains are spaced by b_{pt} 25 nm. By using the equation (4.2), it can be calculated that with these electrode microstructure and by assuming a conductivity σ_{ion} of 5.5 x 10^{-3} S/m, the total resistance only increases by 6% of the value that can be obtained with full covering mixed conducting electrodes. With a coarser microstructure (e.g. b = 1 µm and d =1.5 µm), the resistance would be increased by 250 %.

4.2. Process flow for the fabrication of the µSOFCs

4.2.1. Overview of the process flow

The process flow comprises 4 photolithographic masks and 2 shadow masks used during the deposition of the electrolyte and of the porous anode. The process includes 4 photolithography steps, the deposition of 5 different layers by sputtering and one by electroplating and 4 etching steps. All these steps will be described briefly in this paragraph with illustrations and parameters. A more detailed description of all these technical steps can be found in the literature for example in [13]. A schematic overview of the process flow is given in Figure 10 and Figure 11. In this summary, basics steps such has photolithography and photoresist removal are ignored and film deposition and patterning are combined in the same image. After the process flow overview, the different µSOFCs designed and developed in this work are reviewed with critical dimensions and characteristics. And finally each step is shortly described and its important parameters are summarized.

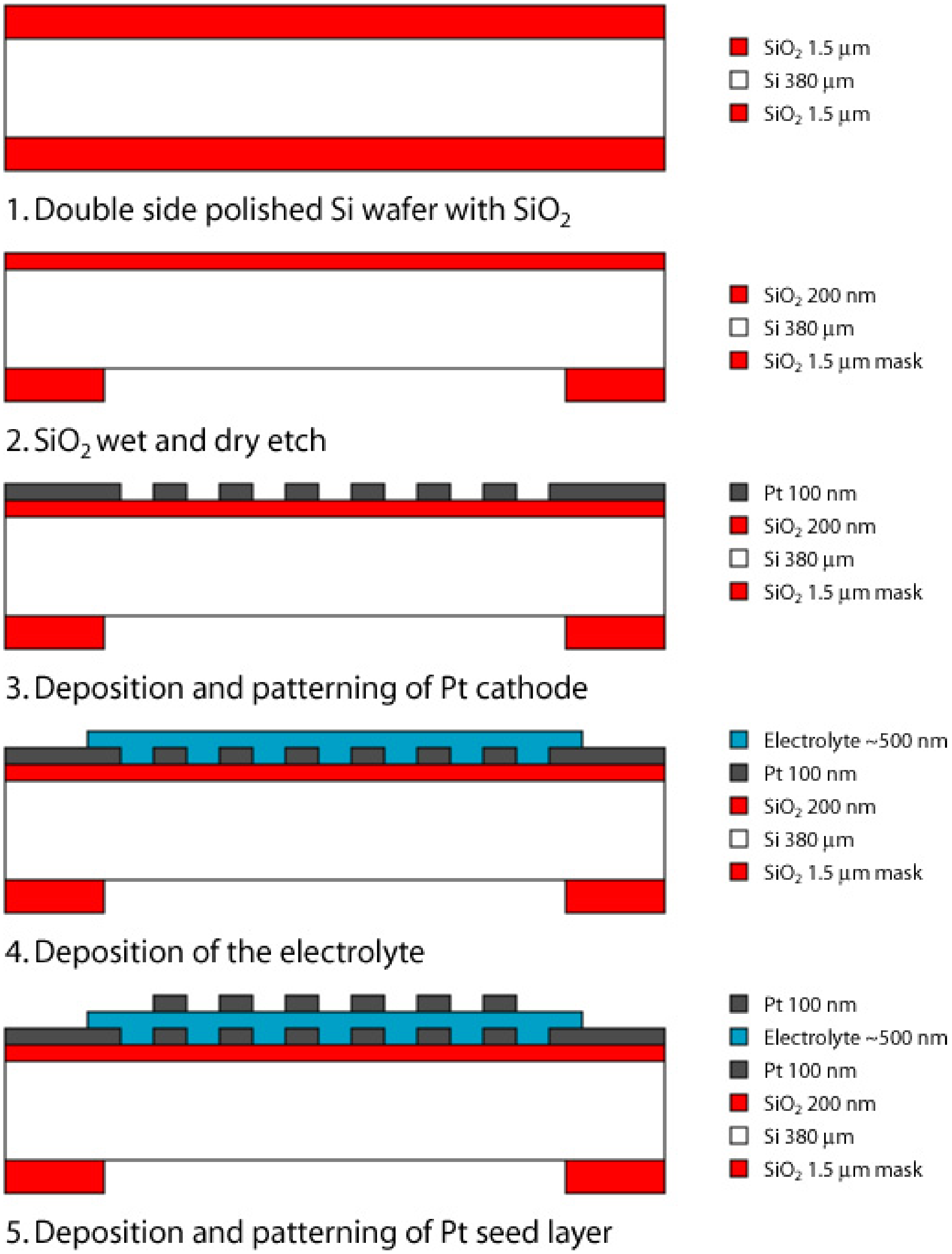

Figure 10: Schematic view of the process flow for the fabrication of μSOFCs.

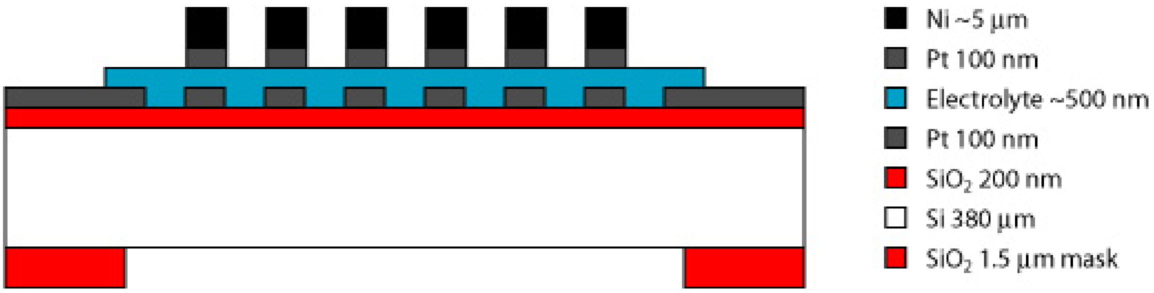

6. Deposition of the Ni grid

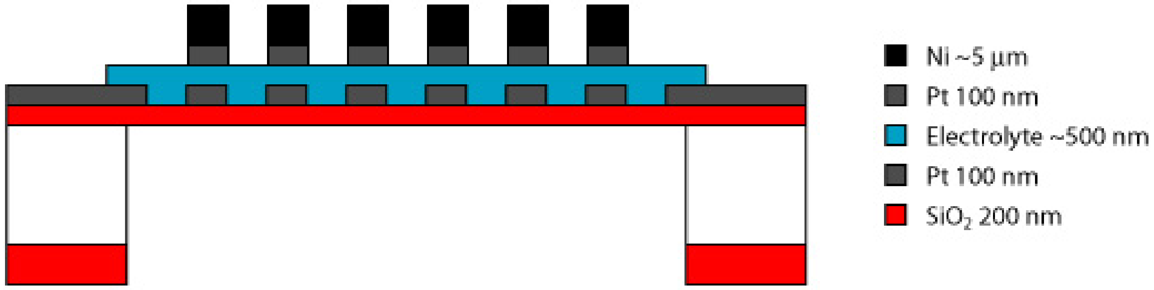

7. Dry etch of the Si wafer

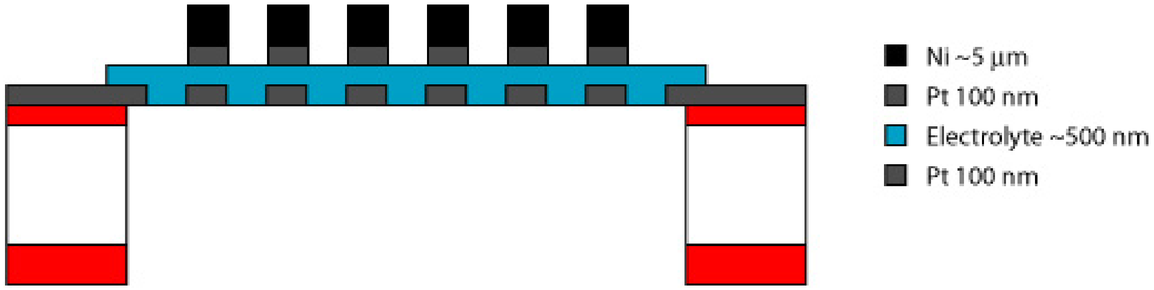

8. Dry etch of the SiO_2

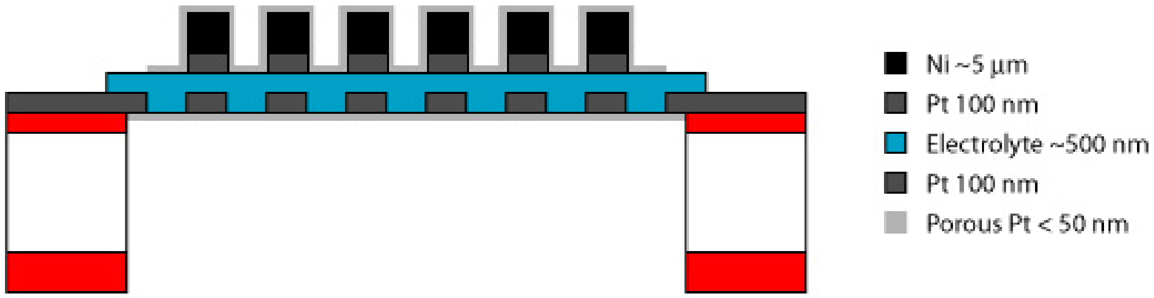

9. Deposition of the porous Pt anode and cathode

Figure 11: Schematic view of the process flow for the fabrication of µSOFCs(continued).

4.2.2. μSOFCs design

The different parts contained in the μSOFC will be briefly described as well as their respective functions. All these components can be found in the cross section scheme of the cell on Figure 1.

1. The device is supported by a silicon wafer 380 μm thick. 6 cells and their connections are disposed on one wafer. At the end of the process the PEN membranes are released by removal of the silicon wafer underneath them.
2. The electrolyte is made of YSZ or CGO and serves as ionic conductor for oxygen ions from the cathode to the anode of the cell. It should be as thin as possible to reduce the resistance but also crack and pinhole free to prevent gas mixing and electronic short cut. In this work, the thickness of the electrolyte is comprised between 500 and 700 nm.
3. The contacts for the cathode are made of a 100 nm thick layer of platinum. It serves as connections for the experimental setup and is linked to the current collector on the cathode side.
4. The current collector on the cathode side is a grid made of platinum (100 nm thick). It collects the electrons created by the reduction of the oxygen ions.
5. The contacts for the anode have the same role as on the cathode side. They are made of nickel and are connected to the nickel grid.
6. The nickel grid serves as support for the thin PEN membrane and as current collector on the anode side.
7. The porous anode and cathode are made of platinum with a thickness of less than 50 nm. They must be permeable to gas and form a percolated network to conduct electrons to the nickel grid. They increase the cell efficiency by increasing the triple phase line length. In some versions, a dense and thin LSC layer has been used in place as cathode.

All the cells fabricated during this work have a cross section comparable to Figure 1. Variations of the size and of the nickel grid pattern lead to four different μSOFC designs:

1. Large cell of 5 mm diameter with a spider web Ni grid
2. Small cell of 0.5 mm diameter with a spider web Ni grid
3. Array of 7 x 7 small cells of 0.5 mm diameter with a spider web Ni grid
4. Large cell of 5 mm diameter with a hexagonal Ni grid

The schematic views of these different cells are given in Figure 12.

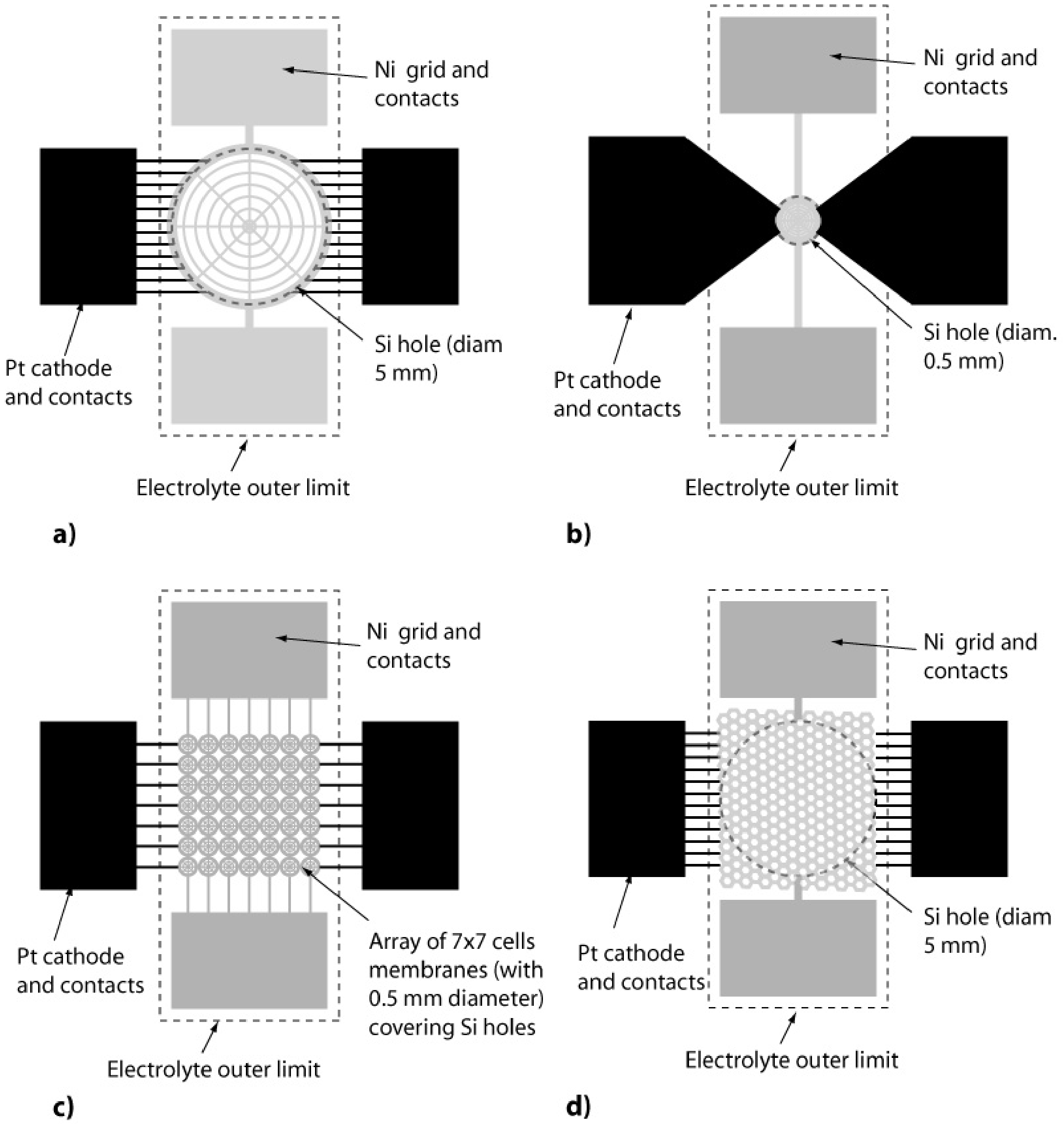

Figure 12: Design of the 4 differents types of µSOFC: a) Large cell with spiderweb grid, b) Small cell with spiderweb grid, c) Array of 49 small cells with spider web grid, d) Large cell with hexagonal grid.

Each design has 4 contacts: 2 for the anode, on the top and on the bottom of the cell, and 2 for the cathode on the left and on the right. The platinum wires are pasted on the contacts for cell measurements. Thus, the contacts cover a large surface (2.5 x 5 mm^2) and are connected to the cell by lines of platinum for the cathode and by the nickel gird for the anode. With the spiderweb grid, the cathode has he same pattern as the nickel grid and they are superimposed. With hexagonal grid, the cathode has the same hexagonal shape as the Ni grid, with the addition of the diagonals of the hexagons as seen in Figure 13:

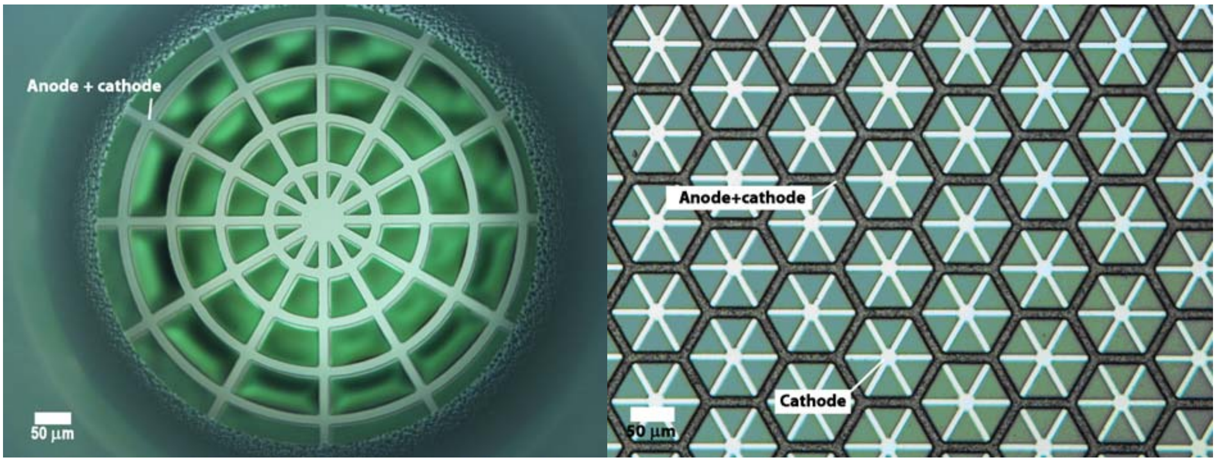

Figure 13: Pictures of the cell with spider web and hexagonal patterns. The places were the cathode and anodes are superimposed are indicated.

In the case of the small spiderweb cells, the cathode contacts have a different shape to minimize the resistance in the thin Pt film (100 nm). In this case, the wires are replaced by a large surface as seen in Figure 12 b. The anode contacts are with the Ni grid and thus they have the same thickness of approximately 5 µm. To prevent peel off due to the stress accumulation over a large area, they also have the form of a grid. This grid has a square pattern with a linewidth of 10 µm and spacing of 20 µm.

To avoid the etch of the electrolyte, it is deposited through a hard mask. This mask is made of a thin stainless steel foil with a thickness 0.3 mm. This mask has 6 apertures with dimensions of 5 mm x 10 mm corresponding to the 6 devices mounted on the wafer. As seen in Figure 12, the electrolyte is thus patterned and covers a region comprising the Si hole and the position of the two anode contacts that will be deposited later onto it. The contacts of the cathode remain uncovered and accessible for electrical measurement.

The 4 designs are mainly differentiated by the size and shape of the Ni grid. Some cells have a diameter of 5 mm and are covered by a hexagonal or a spider web grid. Smaller cells, with a diameter of 0.5 mm, have been fabricated to minimize the influence of the electrolyte film quality on the cells performances. Arrays of 7 x 7 small 0.5 mm cells have also been fabricated. This design was expected to be a solution in the case of the large 5 mm cells were not supporting the ramping to 500°C.

4.2.3. Wafer preparation

Double side polished (100)-oriented silicon wafers with a thickness of 380 µm are used for this process. They are covered by 1.5 µm of amorphous SiO_2 grown by wet oxidation which will later serve as mask for the silicon dry etching.

4.2.4. Patterning of the SiO_2 mask

The goal of this step is to pattern the back side of the wafer to obtain a 1.5 μm thick SiO_2 mask that will serve during the Si dry etch. On the front side, the SiO_2 is thinned down to 200 nm to prevent electrical leakage in the Si wafer during μSOFC operation.

For this purpose, a photoresist layer (S1818 from Shipley) is spun (Rite Track) on the wafer back side, exposed through a photolithographic mask #1 (MA6 aligner from Karl Suess) and developed (in MD351 from Shipley, with Rite Track) to obtain a 3.5 μm thick mask. The other parameters for photolithography are collected in Table 1:

Table 1: Parameters for photolithography.

Thickness [μm]	Spin [rpm]	Bake [°C]/[s]	Exposition [s]/[mW/cm^2]	Development [s]	Post bake [°C]/[s]
3.5	3500	115/120	16/10	45	115/60

The silicon oxide then is wet etched in a buffered solution of hydrofluoric acid (BHF) to thin down the SiO_2 layer to 200 nm on both sides. Further parameters are given in Table 2:

Table 2: Parameters for SiO_2 wet etch

Thickness [μm]	Solution	Time [min]	Rate [nm/min]	Temperature [°C]
3.5-0.2	NH_4F(40%):HF(50%), 7:1	17	77	25

Finally, the remaining 200 nm of SiO_2 on the back side are removed by dry etch in Alcatel 601E. The parameters are given in the Table 3:

Table 3: Parameters for SiO_2 dry etch

Thickness [nm]	Power [W]	Biais [W]	Gas	Time [s]	Rate [nm/min]	Temperature [°C]
~200	1800	90	C_4F_8 200 sccm	~45	340	25

Finally, the photoresist is removed in a chemical solution and then by using an oxygen plasma (Tepla).

4.2.5. Deposition of the platinum cathode

The platinum cathode was deposited onto the 200 nm of silicon oxide remaining on the front side of the wafer. A thin titanium layer serves as adhesion layer. Both layers were deposited in a multi-chamber sputtering tool (Spider from Pfeiffer). The important parameters for this process are given in the Table 4:

Table 4: Deposition parameters for the titanium/platinum layers

Layer	**Thickness [nm]**	**DC power [W]**	**Argon flow [sccm]**	**Time [s]**	**Rate [nm/min]**	**Temperature [°C]**
Titanium	5	1000	15	10	120	300
Platinum	100 (50)	1000	15	22	270	300

This layer serves as a primary cathode and also as current collector from the centre of the cell to the contact. The Pt thickness was reduced to 50 nm for the last devices.

4.2.6. Patterning of the platinum cathode

The platinum cathode is patterned by mean of dry etching and with using of photoresist mask. The photolithography is done with the parameters given in Table 1 and by using the mask #2. The Ti/Pt film is etched by using chlorine chemistry (dry etcher from STS) and important parameters can be found in the Table 5:

Table 5: Parameters for Ti/Pt dry etch

Thickness [nm]	**DC power [W]**	**Gas flows [sccm]**	**Time [s]**	**Rate [nm/min]**	**Selectivity with PR [°C]**
100-0	1000	Cl_2, 15/Ar, 10	360	~35	1/8

This platinum layer has the same spiderweb or hexagonal pattern as the nickel grid. More information about its design can be found in the paragraph 4.1.1. After the process, the photoresist is removed as in paragraph 4.2.4.

4.2.7. Deposition of the electrolyte

The electrolyte can be in a form of a CGO layer, YSZ layer or multilayer of YSZ (2 or 3). The parameters for these depositions and the films microstructure and properties are given in chapter 3.

The electrolyte is sputtered through a hard mask made of stainless steel to keep an access for the cathode contacts.

4.2.8. Deposition of the platinum seed layer for the nickel grid

The platinum seed layer was deposited onto the electrolyte on the front side of the wafer. A thin titanium layer serves as adhesion layer. Both layers were deposited in a multi-chamber sputtering tool (Spider from Pfeiffer). The important parameters for this process are given in the Table 4. This layer serves as electrical connections to the border of the wafer where the electrical potential for electroplating is applied. The nickel grid will grow on the parts of this layer that are not covered by the photoresist mould.

4.2.9. Patterning of the platinum seed layer

The platinum cathode is patterned by means of dry etching and with using of photoresist mask. The photolithography is done with the parameters given in Table 1 and by using the mask #3. The Ti/Pt film is etched by using chlorine chemistry (dry etcher from STS) and important parameters can be found in the Table 5.

4.2.10. Deposition of the nickel grid by electroplating

The nickel grid is deposited in a photoresist mould from a commercial nickel speed bath with the following composition: nickel sulfamate 600g/l, nickel chloride 10g/l, boric acid 40 g/l and additives (Commercial Ni-speed bath). The mould is made in photoresist with the mask #4 and parameters of Table 1. The mask #4 is the negative of mask #3, as the Pt seed layer is used as electrical conductor to deposit the grid.

Table 6: Parameters for the Ni electroplating

Thickness [μm]	**DC current [mA]**	**Current density [mW/cm^2]**	**Time [min]**	**Rate [nm/min]**	**Temperature [°C]**
~5	50	~30	15	35	45

The residual stress in the nickel grid is very important for the sustainability of the cell. The layers made with a commercial Ni-speed bath normally have a compressive state of stress [14]. The stress was measured as a function of the temperature of the bath (30 to 60°C) and the current density (5 to 50 mA/cm^2). The measurements were made on metallic foil covered on one side by a zinc layer and on the other side by an isolating polymer layer. The bending of the bimorph indicates the stress value in arbitrary units. As shown in Figure 14, the compressive stress is reduced by decreasing the temperature and increasing the current density. Thus to obtain a near zero state of stress, the free standing grids were deposited at 45°C and 30 mA/cm^2. The effect of the latter parameters on the films roughness has not been elucidated as they are not interesting for this application.

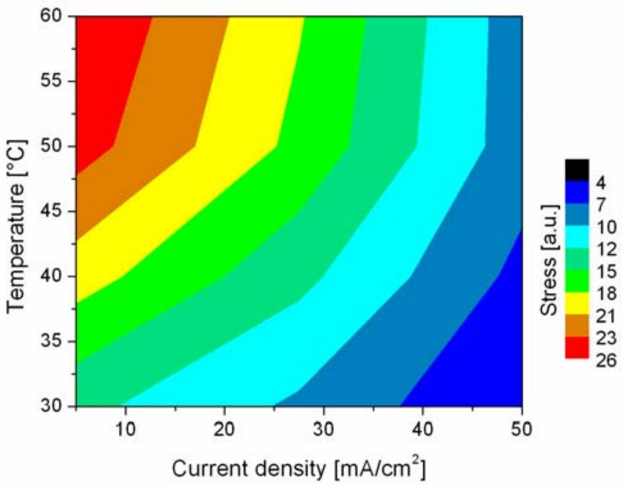

Figure 14: Measured map of the compressive residual stress in deposited Ni films as a function of the temperature and of the current density.

4.2.11. Membrane releasing by silicon deep etching

The deep reactive etching of the silicon wafer releases the thin μSOFC membrane by plasma (Alcatel 601E). Thus, the control of this process, especially the duration, is critical. The Bosch process with sequential pulses of CF_6 and C_4F_8 gas permits to obtain very deep cavities with a very good aspect ratio [15]. The high selectivity of this process with SiO_2, has two advantages:

1. The oxide is a very good mask. The equivalent thickness of photoresist required to etch the same thickness of Si is of 4 μm, but the photoresist is less homogeneous and can stick to the substrate holder.
2. The remaining 200 nm of silicon oxide are a very good etch stop. As the process is not fully homogeneous in the bottom of the hole it permits to fully remove the Si everywhere without attacking the electrolyte.

The parameters used for this process are given in Table 7:

Table 7: Parameters for the dry reactive etching of the silicon with the Bosch process

Thickness [µm]	Power [W]	Substrate bias [W]	Gas pulses	Time [min]	Rate [µm/min]	Selectivity with SiO_2	Temperature [°C]
~380	1800	90	C_4F_8/SF_6 8/300 sccm	45-50	7-10	~400	25

After the removal of the Si, the 200 nm of SiO_2 are dry etched in the same tool. The parameters used for this process are given in Table 8.

Table 8: Parameters for the dry reactive etching of the silicon oxide

Thickness [nm]	Power [W]	Biais [W]	Gas	Time [s]	Rate [nm/min]	Temperature [°C]
~200	1800	90	C_4F_8 200 sccm	~45	340	25

After this step the wafer is cut in 6 parts of 2.5 x 2.5 cm^2, each of them containing one µSOFC.

4.2.12. Deposition of the porous Pt electrodes

The porous platinum electrodes are deposited with the Nordiko sputtering tool with the parameters given in paragraph 3.6.1. The cathode is deposited through the Si hole on the backside of the wafer. The anode is deposited on the nickel grid. A shutter mask made of a thin (0.3 mm) steel foil is used to cover the cathode contacts and prevent electrical shortcut between the anode and the cathode.

4.3. Characterization of the µSOFCs

4.3.1. Encountered fabrication difficulties

The quality of the YSZ sputtered electrolyte has always been a problem leading to electrical leakage in the cells. In contrast to CGO, sputter deposition of YSZ was much more prone to produce particles that were leading to pinholes in the film. Proof was that smaller capacitors were much more reliable than large ones. This can be possibly explained by a stronger charging of YSZ covered shields anodes, leading to higher arcing risks. A further reason might be a too high water pressure in the sputter chamber. Its base pressure was only of 5 x 10^{-6} mbar and it also serves to deposit a large variety of materials including lead zirconate titanate. With an up to date industrial sputtering tool dedicated to YSZ, the film quality could certainly be improved.

The adhesion of the nickel grid was strongly dependent on the quality of the platinum seed layer and of the electroplating bath quality. Some stress studies have demonstrated that the Ni-speed bath described in paragraph 4.2.10 was developed to obtain film under compressive stress [14]. This is an advantage for metallic coatings but not for free standing structures. It would be preferable to use another type of bath leading to a tensile stress. As it was not possible for clean room compatibility reasons, we decided to adapt the deposition parameters with the existing bath in order to reduce the compressive stress in the electroplated films. The platinum seed layer has to be deposited on a titanium thin adhesion layer of approximately 3 nm. To ensure thermal stability the deposition temperature should be close to the operation temperature of the cell. In the Spider sputtering tool, the maximal deposition temperature is of 350°C. The quality of the layer can then be improved with an annealing. The chemical stability of the Ti layer can be enhanced by adding a TiO_2 layer onto it to prevent Ti diffusion in the platinum. Albeit, as far as we know, the diffusion of Ti has never been a problem for our devices, this TiO_2 layer can be easily implemented.

When releasing the membrane by deep reactive silicon etching the 200 nm SiO_2 layer serves as etch stop. Albeit the selectivity of the process is very good, membranes can be fully released before starting the SiO_2 etch. As the etching rate is dependent on membrane size and not homogenous over the surface of the wafer, several inspections with optical microscope are required during the last five minutes of the process. Then as the silicon oxide and the YSZ membrane are transparent it is difficult to control the removal of the SiO_2 layer. Experience has shown that the YSZ is very resistant to the C_4F_8 gas so we prone to over etch the oxide layer.

4.3.2. Mechanical and thermal resistance of the µSOFCs

The µSOFC with a diameter of 5 mm and supported by a spiderweb nickel grid have been successfully fabricated as seen in Figure 15:

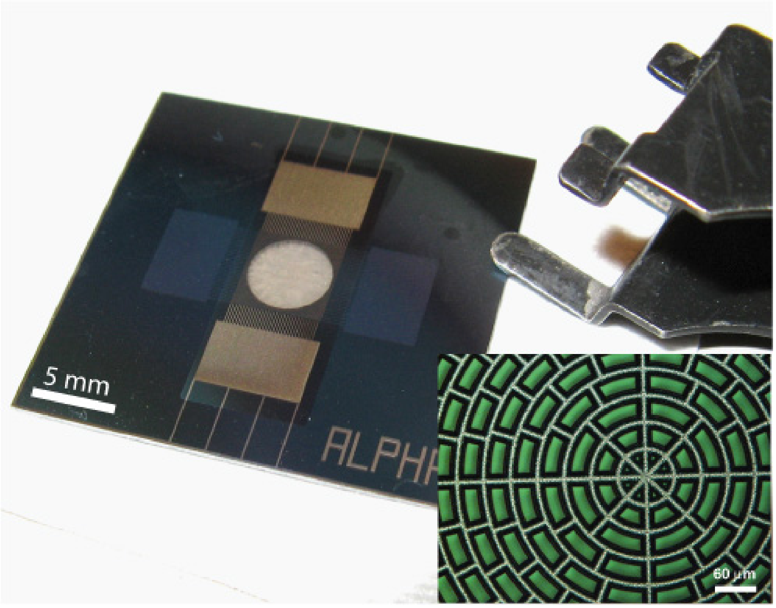

Figure 15: Spiderweb μSOFC with a diameter of 5 mm.

This type of cell can resist several thermal cycles up to 550°C, under operation condition with a flow of oxygen (10 sccm) on the anode and a mix of hydrogen (10 sccm) and argon (10 sccm) on the cathode. Inspections with the help of an optical microscope have proven that the electrolyte was not cracked. The two main reasons for this mechanical and thermal stability are:

1. The support of the nickel grid
2. The relatively low stress change with temperature (+/- 100 MPa up to 500°C) of the YSZ after annealing as explained in the paragraph 3.2.3.

After this annealing treatment even small YSZ membranes of 0.5 mm diameter that are not supported by a nickel grid can survive silicon deep etching. On the contrary, CGO membranes with a diameter of 0.6 mm were already cracking at 350°C and already subject to large strain even at room temperature Figure 16. Apart from the electrical leakage, this bad mechanical stability was another reason to exclude CGO.

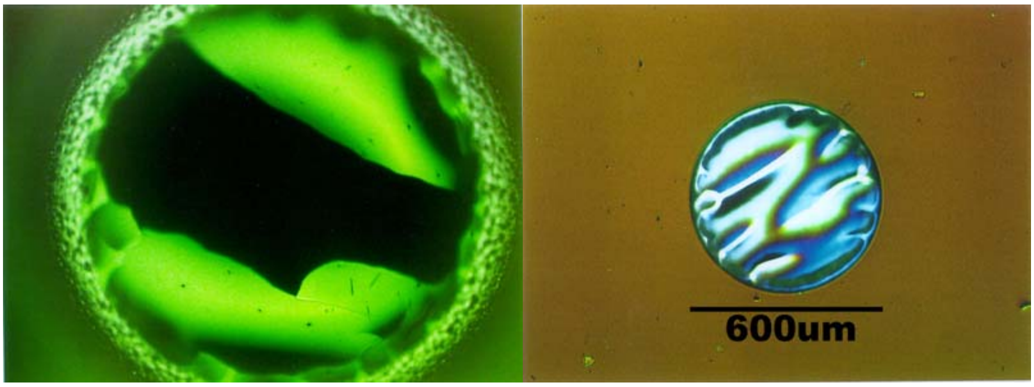

Figure 16: 600 μm diameter CGO membranes with a thickness of 500 nm after heating to 350°C (left) and after silicon removal at 25°C (right)

4.3.3. Detection of leaking cell during the process flow

In this paragraph, we show a method to control the quality of the electrolyte film before the end of the process flow. Two types of defects can lower the OVC:

1. Pinholes leading to metallic shorts: They show large leakage currents even at room temperature. Such pinholes are much rarer on smaller devices. Bad devices with pinholes can be removed from further process before Ni grid plating and membrane liberation.
2. Thermally activated grain boundary diffusion of electrons: This effect can only be observed at high temperature and thus only detected at the end of the fabrication process.

Measurements of the capacity *C* and losses $tan\delta$ of the YSZ films at room temperature have been carried out. The capacity *C* can be written in complex form as:

$$C = C'(1 - i\tan\delta) \quad (4.4)$$

The total parallel resistance R_p of the film capacity *C'* can be expressed by the dielectric losses $1/\omega C' tan\delta$ (linearly decreasing with frequency) and the leakage R_l (constant with frequency).

$$R_p = \frac{R_l}{1 + R_l \omega C' \tan\delta} \quad (4.5)$$

If R_p is plotted against the frequency $f\ (2\pi\omega)$ for films deposited on platinum (as in 3.2.4), R_p linearly decreases with the frequency showing only dielectric losses (Figure 17). For bad devices, R_p is constant with f indicating an electronic leakage through the film and thus the cells present a very low OCV. For better devices, R_p is constant at low frequencies and then decreases linearly with *f*. In this case, the cell OCV reaches 200 to 280 mV. As we use the same deposition parameters for YSZ on Pt test samples and on devices, we suspect that leakage in the films is due to the micro-cracks induced by the patterned cathode mesh on which YSZ is grown.

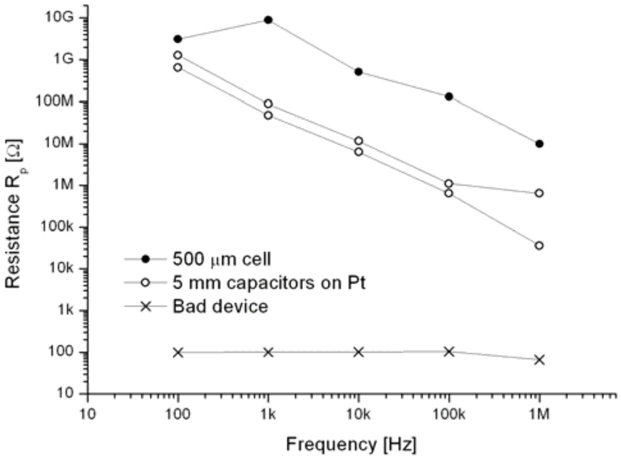

Figure 17: Resistance of the devices and of cylindrical YSZ capacitors with the frequency

By this simple capacity measurement it is possible to eliminate bad devices before the end of the process flow. Nevertheless, this method is not sufficient to insure the quality of the μSOFCs as these measurements are done at room temperature. It is also impossible to put a wafer in a furnace or to fix platinum wires onto it before the end of the process flow as clean room work requires a minimum of contamination and dust.

4.3.4. μSOFC voltage and power measurement

4.3.4.1. Experimental setup

The μSOFC voltage and power output are tested in a furnace capable of heating up to 1200°C (B150 from Nabertherm). 4 platinum wires with a diameter of 0.5 mm (from Goodfellow) are flattened by using an hydraulic press and then stuck to the sample. Each of the wire is glued by using an alumina cement (from Zircar). Pt paste (Heraeus LPA 88/11 S) is applied between the contact and the wire to improve the conductivity. Then the sample is pressed between two pieces of alumina with a ceramic tissue (from Goodfellow). Two quartz pipes are mechanically clamped on both sides of the samples to provide the oxygen for the cathode and the fuel for the anode Figure 19. The flows of argon, oxygen and hydrogen are controlled with 3 flowmeters (MKS 1179) and a flow controller (MKS 647B). Most of the experiments were performed under pure oxygen at the cathode and a mix of argon and hydrogen at the anode. A Pt/PtRh thermocouple is placed in the quartz tube on the anode side near the sample holder and another one is placed in the furnace near the sample holder.

The open circuit voltage of the cell was measured with a digital multimeter (Hewlett Packard 34401A) placed in parallel with the cell.

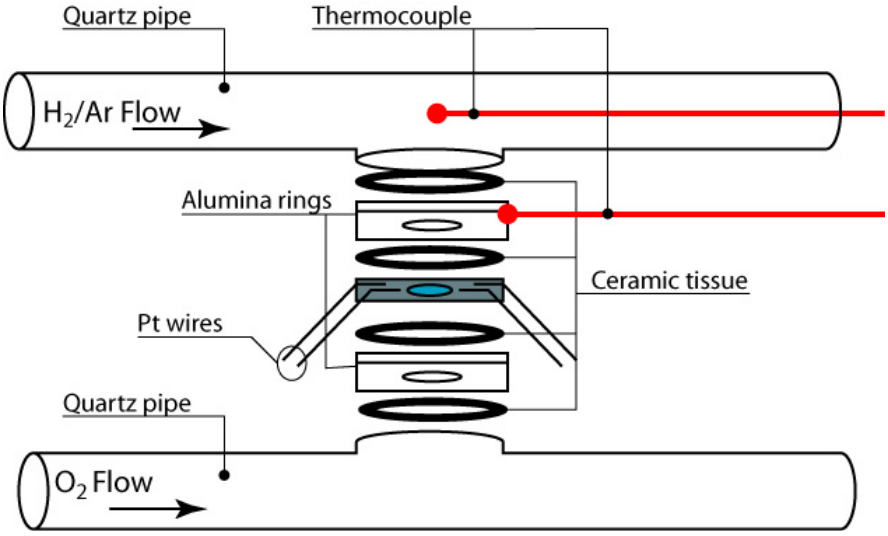

Figure 18: Schematic view of the fuel cell measurement setup

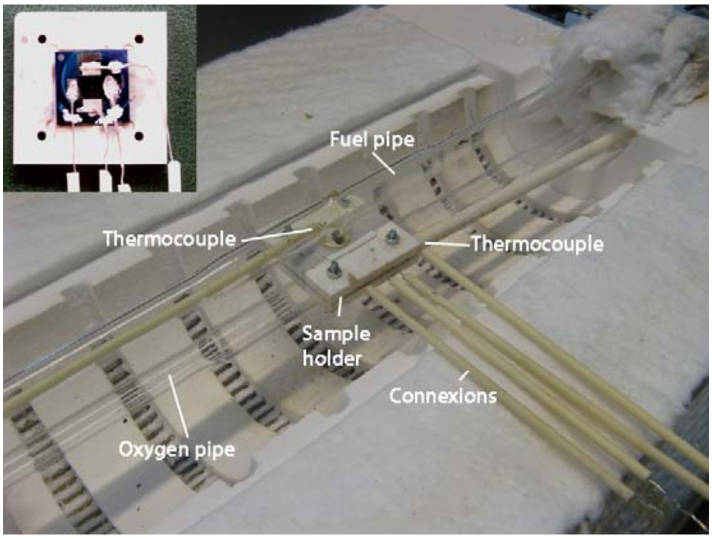

Figure 19: View of the experimental setup in the furnace and of the electrical connections onto the µSOFC (top left).

The current versus voltage curves (I-V curves) are measured by using the electrical montage of Figure 20:

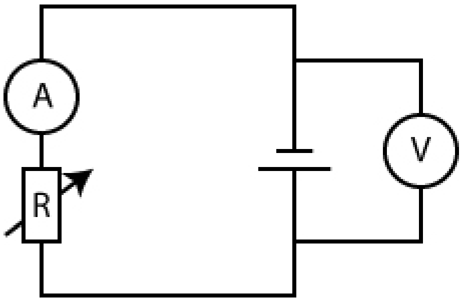

Figure 20: Scheme of the electrical montage for I-V curves measurements.

A digital multimeter (Hewlett Packard 34401A) was placed in parallel with the cell to measure the voltage. A variable resistance (1 Ω-10 MΩ) was used as a load and placed in series with the cell and an electrometer (Keithley 617) that was measuring the current. The different points of the curves were obtained by changing progressively decreasing the resistance of the load.

4.3.4.2. Open circuit voltage

Open circuit voltage was measured on several fuel cells with different types of electrolytes and electrodes. The maximal OCV that was obtained at 500°C and is of 850 mV for a small spider web cell (diameter 0.5 mm) with an electrolyte composed of two YSZ layers respectively (111) and (200) oriented and porous platinum electrodes (~20 nm thick). The anode was exposed to pure hydrogen (6 sccm) and the cathode to pure oxygen (6 sccm). For comparison, the OCVs of all the cells tested during this work are summarized in Figure 21:

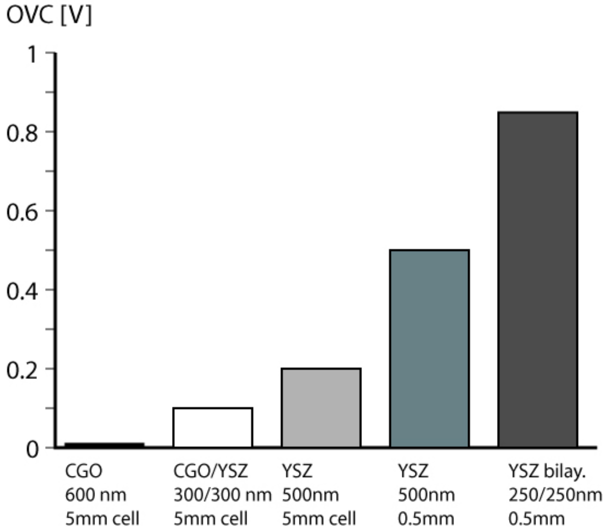

Figure 21: OCV of the different types of fuel cell fabricated.

This summary clearly show that the OCV increases when the cell has a bilayer electrolyte and that it was not possible to obtain a voltage when the electrolyte was only composed of CGO. We suppose that the thin layer of CGO was reduced by hydrogen and becomes electronically conducting.

The OCV of the cell that reaches 850 mV in H_2, was first measured under a pure flow of argon at the anode (6 sccm) and a flow of oxygen (6 sccm) at the cathode during ramping up from 20°C to 420°C. A maximal voltage of 120 mV is obtained at 390°C in this case (Figure 22):

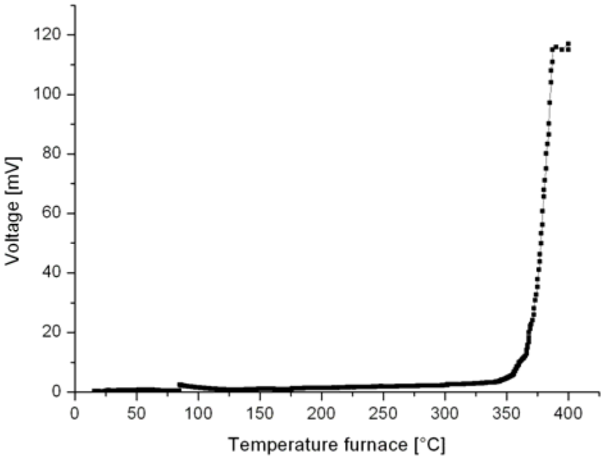

Figure 22: Voltage versus the temperature of the furnace. The anode is exposed to pure argon (6 sccm) and the cathode to pure oxygen (6 sccm). The electrolyte was composed of a YSZ bilayer (111)/(200) (250 nm/250 nm)

As explained in the first chapter, the OCV of the cell can be related to the oxygen pressures at the cathode $p_c(O_2)$ and at the anode $p_a(O_2)$:

$$OCV = \frac{RT}{nF}\ln\frac{p_c(O_2)}{p_a(O_2)} \tag{4.6}$$

Thus it is possible to calculate $p_a(O_2)$ by assuming that $p_c(O_2)$=1 atm. In this case the pressure is of $1\text{x}10^{-4}$ atm. This value can be reached in pure argon [16]. This curve also shows that in absence of hydrogen a low electronic leakage is obtained.

4.3.4.3. I-V curves

I-V curves of the best cell were obtained as explained in the paragraph 4.3.4.1. As seen in the Figure 23, the maximal power density at 500°C was of 19 µW/cm^2 and is a thousand times lower than expected. Nevertheless, the I-V behaviour of the cell looks normal and we suppose that a high internal resistance due to the design of the cathode current collector is responsible for this low power.

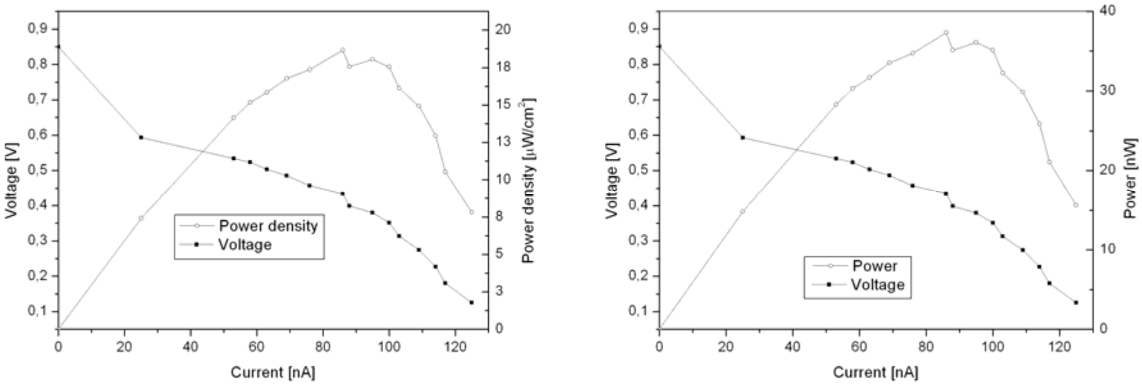

Figure 23: I-V curves with the cell power (left) and power density (right)

It was possible to estimate the value of the internal resistance due to the design. The platinum line between the cell and the cathode contact was 4 mm long, 100 nm thick and 5 µm wide as seen in Figure 24.

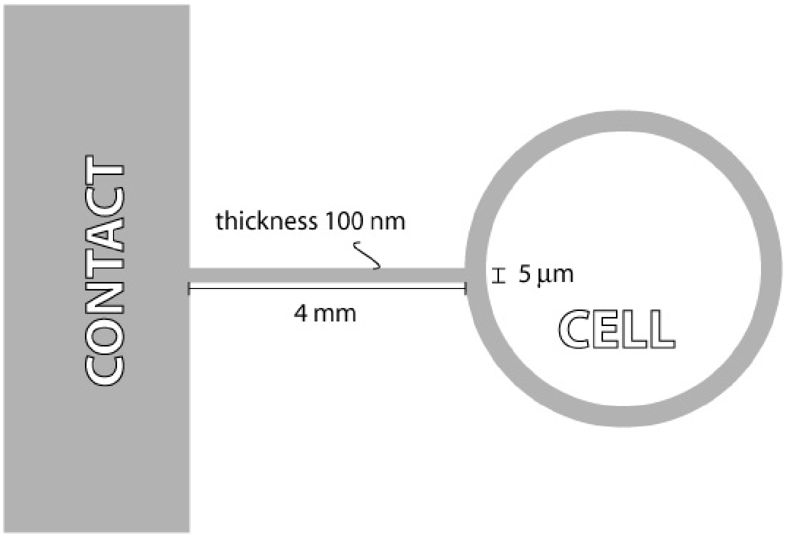

Figure 24: Schematic view and dimensions of the platinum contact line between the cell and the cathode contact.

At 500°C the resistivity of the platinum is of 28.7 x 10^{-8} Ωm [17]. Thus, the cell has a resistance of 2.3 kΩ that lowers its output current. This internal resistance is higher than the resistance of the electrolyte (diameter 0.5 mm, thickness 500 nm and YSZ conductivity 5.5 x 10^{-3} S/m) that is in the range of 400 to 500 Ω. This design problem has been solved increasing the size of this connection as seen in Figure

12 b. Unfortunately all the cells fabricated with design contain a three layer YSZ electrolyte, with a total thickness of 700 nm, that show cracks at 500°C as seen in Figure 25.

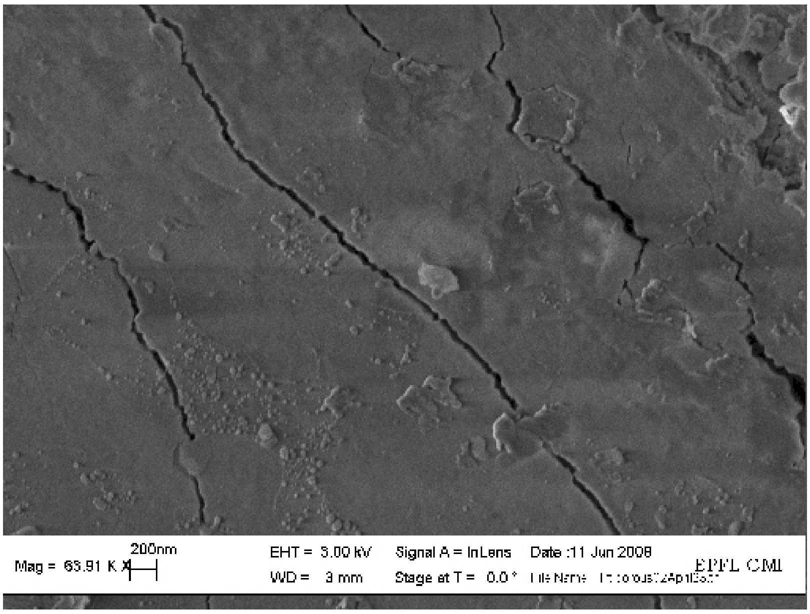

Figure 25: Cracks in YSZ three layers membrane after 1 hour under SOFC operation conditions.

The combination of a two layer electrolyte with the new design will lead to better power output.

4.4. Summary

An innovative concept for µSOFCs based on silicon microfabrication has been proposed, developed and tested. The thin and brittle electrolyte membrane is supported by a nickel grid grown by electroplating on a platinum seed layer. The dimensions of the grid cells have been designed to prevent buckling or cracking of the membrane during temperature cycling up to 600°C. The mechanical stability of the grid and its adhesion to the electrolyte are good up to 600°C during several cycles. Thus membranes with a diameter of 5 mm, a thickness of less than 1 µm that are supported by a nickel grid resist thermal cycles from room temperature to 600°C. Apart from these large 5 mm cells, smaller cells with various grid designs have also been fabricated. The advantage of the smaller cell with a diameter of 0.5 mm is to limit the probability of having a defect through the electrolyte that can cause severe performances drops. Prior to membrane release, the PEN elements were qualified by impedance spectroscopy. In addition, YSZ electrolytes in a form of a multi layer have also been used to avoid electrical leakage through the cell along grain boundaries or pinholes.

A cell with a bilayer YSZ electrolyte, with a total thickness of 500 nm, has been fabricated. To enhance the TPB length, platinum porous layers (20 nm thick) with a fine microstructure were deposited on both electrodes. The grain size of this layer is in the range of 10 to 30 nanometers. Calculations have proven that the microstructure of the electrodes only lowers the cell resistance if the grains are finer than the electrolyte thickness. With such electrode microstructures, calculations show that the total resistance only increases by 6% of the value that can be obtained with full covering mixed conducting electrodes.

The functionality of the fuel cell has been demonstrated by the measurement of an OCV of 850 mV with the anode exposed to a reducing atmosphere (pure H_2) and the cathode exposed to pure oxygen gas at 500°C. I-V curves of the best cell were obtained. The maximal power density at 500°C was of 19 $\mu W/cm^2$ and is a thousand times lower than expected. The reason for this low power has been elucidated and is due to the high resistance (2.3 $k\Omega$) of the platinum connections between the cell and the cathode. Newly designed cells to correct this defect have been tested. Unfortunately, the chosen three-layer electrolyte was less stable than the two-layer one and cracked during fuel cell operation

4.5. References

1. Schaevitz, S.B., A. Franz, and R.W. Barton, Stressed thin-film membrane islands. 2005: USA.
2. Jankowski, A.F., et al. Micro-Fabricated Thin-Film Fuel Cells for Portable Power Requirements. in Proceedings of the Materials Research Symposium. 2002.
3. Jankowski, A.F., et al., Testing of solid-oxide fuel cells for micro to macro power generation. Electrochemical Society Proceedings, 1997. 99(19): p. 932-937.
4. Srikar, V.T., et al., Structural design considerations for micromachined solide-oxide fuel cells. Journal of Power Sources, 2004. 125: p. 62-69.
5. Funimori, S., Cell plate structure for solid electrolyte fuel cell, solid electrolyte fuel cell and related manufacturing method. 2002: Europe.
6. Kushibiki, K., Single cell for fuel cell and solid oxide fuel cell. 2003: USA.
7. Sarkar, P. and H. Rho, Crack-resistant anode-supported fuel cell. 2004: US.
8. Miller, M.A. and C.M. Wall, Three-electrode fuel cell. 2003: US.
9. Jankowski, A.F., J.D. Morse, and R. Barksdale, Method for fabrication of electrodes. 2004: US.
10. Tang, Y., et al., Design consideration of micro thin film solid-oxide fuel cells. Journal of Micromechanics and Microengineering, 2005. 15(9): p. S185-S192.
11. Fleig, J., H.L. Tuller, and J. Maier, Electrodes and electrolytes in micro-SOFCs: a discussion of geometrical constraints. Solid State Ionics, 2004. 174: p. 261-270.
12. Steele, B.C.H. and A. Heinzel, Materials for fuel-cell technologies. Nature, 2001. 414: p. 345-352.
13. Madou, M.J., Fundamentals of microfabrication. 2002, Boca Raton FL: CRC Press.
14. Canning handbook on electroplating. 1978, Birmingham: W. Canning Limited.
15. Bharwaj, J. and H. Ashraf. Advanced silicon etching using high density plasmas. in SPIE 2639. 1995.
16. Voisard, C., Conductivity, dielectric and piezoelectric properties of SrBi4Ti4O15, in Ceramics Laboratory. 2000, Swiss Federal Institute of Technology: Lausanne.
17. CRC Handbook of Chemistry and Physics. 75th ed, ed. D.R. Lide. 1994, London: CRC Press.

Conclusion and outlooks

Micro solid oxide fuel cells are promising devices for extending considerably the autonomy and energy efficiency of portable power supplies. Although proposed for the first time 18 years ago, it is only during the last few years that development and research efforts have been undertaken. This work is part of this effort. Its goal was to use thin film and silicon microfabrication technologies to fabricate SOFCs with a volume of cubic centimetres. This work was mainly divided into two parts. The first one was related to the deposition of the thin films composing the PEN by reactive magnetron sputtering and to the characterization of these materials. The second deals with the fabrication and the performance evaluation of this micro-fabricated solid oxide fuel cell device mounted on a silicon wafer.

One of the key issues in µSOFCs is the lowering of the operation temperature. This is firstly required for the application in a small device that should not be too hot for a safe use. Secondly, it means also to enter in a new temperature range for solid ionic materials, since most of the knowledge was related to high-temperature applications above 900 °C. Thirdly, a lower temperature is also a key enabler to bring micro technology and thin films into the game. Large SOFC power generators still suffer from insufficient robustness against aging. The high operation temperatures are indeed very demanding with regard to materials stability. The considerable lowering of operation temperature in combination with a miniaturization of the device may relaxes aging issues because all the degradation mechanisms are based on thermally activated processes. The fourth issue is a key challenge: the maximally allowed PEN membrane thickness is less than a micrometer in order to avoid too high internal resistances. This imposes very stringent conditions on electrolyte density and mechanical stability. In this work, both of these issues are studied.

We have proposed to integrate a nickel grid as mechanical support for the fragile PEN membrane as an innovative solution to obtain large active surfaces of some square millimetres. This grid also has the function of anode current collector. Our concept is more than a simple down scaling of the existing SOFC technology, it is a new approach based on silicon microfabrication techniques and thin film sputtering. We showed that the integration of a μSOFC on a silicon wafer is possible and that it opens a solution for batch processing and thus cost efficiency. As to processes, we demonstrated that the sputtering method is very versatile and capable of depositing thin films with various morphologies and compositions and with sufficiently high conductivity, thus useful for PEN fabrication. It was for example possible to deposit a porous platinum electrode on a dense YSZ electrolyte. The materials choice turned out to be more limited than originally expected. We learned that for the thin layers, as required for the electrolytes, only materials with an extrinsic type of oxygen vacancy stabilization do work. Multivalent ions such as Ce in CGO tend to form free electrons to compensate for oxygen vacancies. We showed that CGO was unable to produce an OCV when it was the only electrolyte layer. This is most probably due to the exposure to reducing conditions at the anode side, leading to a too high concentration of free electrons reaching the cathode through the few 100 nm thick electrolyte layer. Finally, the only electrolyte material that so far showed good OCV's was YSZ, in which the vacancy concentration is balanced by the Y dopant concentration, and none of the cations changes valency. The first YSZ membranes showed small OCV's of the order to 200 mV. A substantial improvement was achieved by using double layers interrupting grain boundaries crossing the entire film thickness, leading finally to an OCV of 850 mV.

In the final version, YSZ thin films were deposited by means of reactive magnetron sputtering onto oxidized silicon substrates at 530°C. The films are (111) oriented, with a dense and crack free columnar microstructure. A second type of microstructure was achieved with the help of RF bias applied at room temperature. These conditions resulted in a nanocrystalline film of preferential (200) texture, exhibiting a porosity of about 25 %. This film could be grown also on dense YSZ(111) films and was used to interrupt grain growth of the latter. Two and three YSZ layers stacks ((111)/(200) or (111)/(200)/(111)) were investigated.

The ionic conductivity of the YSZ was studied as a function of temperature in air. The achieved 5.5 x 10^{-3} S/m at 500°C are sufficiently high for SOFC operation, and compatible with an electrolyte thickness of 500 nm. The activation energy for ionic conduction was measured as 0.92 eV. As-deposited films showed some problems with respect to mechanical stress and conduction. An annealing in oxygen at 700 °C was needed to obtain films with reproducible conductivity and low stress.

A detailed analysis of mechanical stress as a function of temperature, carried out in air to allow for oxygen exchange, lead to the conclusion that the YSZ films are partially reduced after deposition, and contain 2 to 4 % more oxygen vacancies than defined by the Y content. Their concentration was mostly given by the equilibrium with the partial oxygen concentration during cool down within the chamber. It was possible to derive the concentration directly from the final stress, knowing the mass action laws for reduction, and the strain per oxygen vacancy. The anomalous hysteretic stress vs. temperature behaviour could be explained by oxygen vacancy loss, or in other words, the refilling of the excess vacancies. A anneal of one hour in air at 700°C was found to be sufficient for removing these excess vacancies, and in addition to reduce the large compressive stress to practically zero. A model was developed explaining the observed stress change in terms of diffusion processes. The activation energy for the excess vacancy diffusion was determined as 0.6 eV. This is much less than the 1.07 eV reported for the vacancies trapped by the Y^{3+} point defect. Obviously, vacancies that are not paired with cationic defects need less thermal activation. This was predicted in the literature based on model calculations, even postulating a smaller activation energy. However, charge compensating electrons were not accounted for in this work. Our study shows that stress measurements are useful to analyze changing defect concentrations, and their diffusion processes. Most interestingly, the excess vacancies lead also to an anomaly in the conductivity, when the films were heated up for the first time.

The CGO thin films were deposited by means of reactive magnetron sputtering onto different substrates at different temperature (20°C and 430°C) and gas conditions (Ar or Ar and O_2). XRD analysis shows that the films are mostly (111) textured on platinum when deposited at high temperature. The target had to be enriched with Ce to compensate for Ce loss during sputtering. The stress behaviour of the CGO films has been studied as a function of temperature. As in YSZ, the as-deposited films contain free oxygen vacancies, but in contrast to YSZ, these ones are trapped near Ce^{3+} defects, and this show much larger diffusion activation energy of 1.2 eV. The ionic conductivity of the CGO has been measured as a function of temperature in air. At 500°C, the conductivity amounts to 0.5 S/m and is sufficient for SOFC operation. The activation energy is slightly smaller than the literature values. The ability of the Ce ions to be reduced from +IV to +III causes electronic leakage in thin CGO films used as electrolyte in μSOFCs. As mentioned above, CGO was found to be too leaky for achieving any OCV.

This work included as well electrode thin films. Dense LSCO cathodes, porous platinum and porous Ni-CGO composite anodes were developed and investigated. The growth of Ni-CGO films by co-sputtering from a nickel and a CGO target was studied as anode material. It was possible to obtain columnar porous films with various compositions. LSC dense cathode and porous platinum electrodes were studied for use as cathode material. To enhance the TPB length, platinum porous layers (20 nm thick) with a fine microstructure were deposited on both electrodes. The grain size of this layer is in the range of 10 to 30 nanometres. Calculations show that pore and grain size of the electrode must be smaller than the electrolyte thickness in order to profit plainly from the TPB enhancement. With the realized microstructure, we expect a resistance that is only 6% larger than the one of an ideal, dense, mixed conducting cathode layer.

An innovative concept for µSOFCs based on silicon microfabrication has been proposed, developed and investigated. The thin and brittle electrolyte membrane is supported by a nickel grid grown by electroplating on a platinum seed layer. The dimensions of the grid cells have been designed to prevent buckling or cracking of the membrane during temperature cycling up to 600°C. The mechanical stability of the grid and its adhesion to the electrolyte were found to be good up to 600°C during several cycles. Even membranes of 5 mm diameter resisted to thermal cycles from room temperature to 600°C. Apart from these large 5 mm cells, smaller cells with various grid designs have been fabricated. For the final devices, smaller cells of 0.5 mm diameter were fabricated to limit the probability of pinholes in the electrolyte.

The best cell so far fabricated in this work contained a 500 nm thick bilayer YSZ electrolyte. The functionality of the fuel cell has been demonstrated by the measurement of an OCV of 850 mV with the anode exposed to a reducing atmosphere (pure H_2) and the cathode exposed to pure oxygen gas at 500°C. The maximal power density at 500°C was determined as 19 $\mu W/cm^2$. Although this looks very disappointing, the result is nevertheless encouraging as a high series resistance of 2.3 kΩ in the cathode connection line was identified as main reason for current limitation. Newly designed cells should be free of this problem.

The perspectives for µSOFCs are encouraging. Since the beginning of this thesis, literature reported that solid oxide fuel cells can operate even at low temperatures (400°C to 600°C) and they are capable of power density outputs up to 400 mW/cm^2. All of these demonstrators are fuelled with hydrogen. The next step to hydrocarbons (i.e. butane) is not yet demonstrated. No one made a test with carbon monoxide. In this work cells tested with CO never showed an OCV. The next step is to fabricate a complete system with a viable PEN, a gas tank, a reformer and a start-up system. The group of Prof. Poulikakos (ETH Zürich) from the ONEBAT project has proven that reforming of the methane of butane is possible at 500°C and that such a reformer can be implemented in a µSOFC system. Some solutions for thermal insulation have also been demonstrated in the frame of the ONEBAT project. For the moment, the major disadvantage of large SOFC systems is the long start up time. In portable applications, such as laptops or power tools, is less the time but the question how to do it. The heating of the PEN by burning the fuel can be a good solution but also opens safety questions. The use of ohmic heating systems requires electrical energy. A solution can be a hybrid SOFC/Li-ion system that can store a part of the energy produced by the cell and use it to restart it afterwards. Finally, the safety of the gas tank should be studied even if the cell is fuelled by methane and includes a reformer. In the case of hydrogen storage encouraging technology already permits to fabricate safe SOFC powered cars, but the question of the size reduction is still open.

There are indeed still many open questions. The micro-fabricated solid oxide fuel cell is in a very early stage and it is not yet foreseeable when it will reach the market. It is difficult to predict whether a good price vs. performance ratio will be obtained. A large effort of a large company or consortium is needed to develop a viable product. Hopefully, the growing interest in clean energy will liberate resources to finance higher efforts in µSOFC development.

Annexes

A.1. Pulsed laser deposition

Pulsed laser deposition (PLD) has been largely limited to laboratory investigations of small areas thin films [1]. PLD has the capability of producing stochiometric multicomponent films [2]. In the PLD chamber, a target of the material to be deposited is irradiated with a pulsed laser beam of wavelength comprised between 200 and 400 nm. The target is usually a small disk of ceramic prepared by sintering of powders. It should be dense to avoid droplet ejection and have small grain to enhance the film stochiometry. The absorbed beam energy is converted into thermal, chemical and mechanical energy causing ablation of the target's surface. The created plume contains neutral atoms, molecules, ions, electrons, atoms cluster and even molten droplets. The laser beam enters the chamber trough a UV transparent window after being focalised on the target by a lens. The plume is highly directional and perpendicular to the target. The geometry of the chamber is very important as the laser beam should be focalised on the target and the substrate should be directly in the plume. The target is rotating to slow down its degradation. The substrate is heated to a temperature up to 1000°C to improve the film cristalinity. Oxygen and nitrogen gases are often introduced in the chamber to promote film adhesion or maintain stoichiometry. The working pressure is usually of hundreds of militorrs. The main parameters for PLD are: the gas pressure in the chamber, the gas composition, the substrate temperature, the laser fluence (thousands of mJ/cm^2) and its frequency (10-50 Hz).

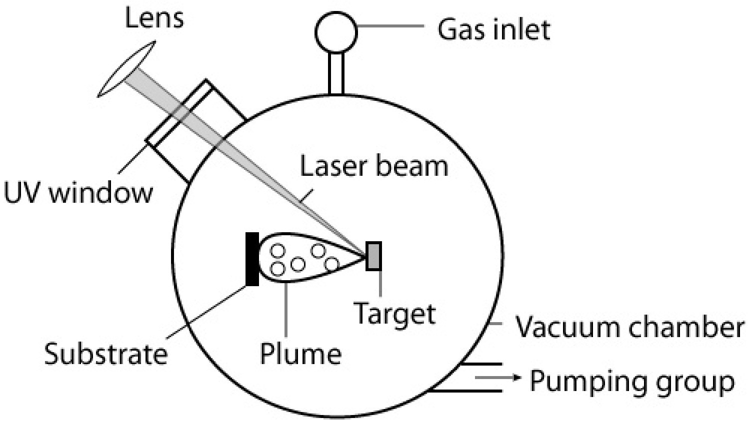

Figure 1: Schematic representation of a pulsed laser deposition system

PLD has been widely used to deposit cathodes such as lanthanum perovskites [3-6]. Most of the PLD films are dense and ideal for YSZ [7] or CGO electrolytes [8, 9]. Nevertheless, it is also possible to deposit porous electrodes by this method [10].

A.2. Chemical vapour deposition

The chemical vapour deposition CVD is a very versatile method that can produce pure, dense and homogenous films, monolayers, multicomponent films and even 3D structures such as carbon nanotubes. It has been used for several applications including coating, semiconductors and optoelectronics [11]. In CVD, the species to be deposited onto the substrate are not ejected from a target. A reactive gas is introduced in the chamber and transports the precursors of the desired materials onto the substrate. The gas directly decomposes onto the substrate or reacts with some other gases to form a film. The different gases are mixed together before entering the reaction chamber where the substrate is located. A set of reactions activated by the heating occurs when the reactive mixture flows along the substrate. In plasma enhanced chemical vapour deposition PECVD a plasma discharge is used to activate the reactions. Some other methods including light assisted decomposition and flame pyrolisis also exist [1]. CVD does not require high vacuum but processing under low pressure helps to reach high film purity. The major drawback of CVD is the difficulty to form multicomponent stochiometric films because the precursors have different vaporisation rates.

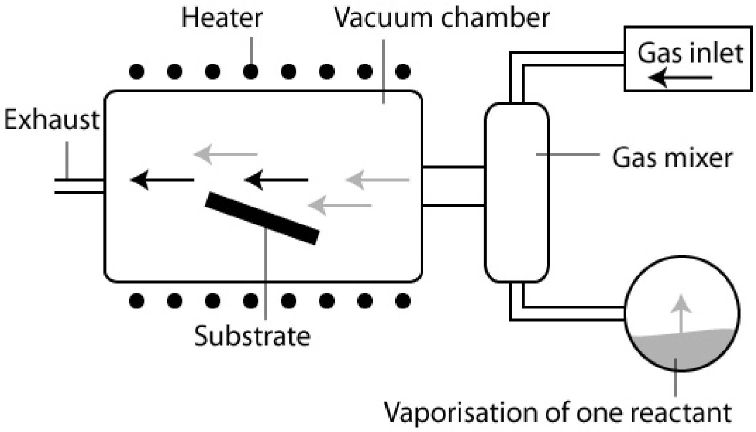

Figure 2: Schematic representation of a chemical vapour deposition system

CVD dense films are very useful for electrolytes such as YSZ [12, 13] and it has the desirable ability to of depositing dense film on porous electrodes [14] or to prepare YSZ-NiO porous anode cermets [15]. Another advantage of CVD is its capacity to deposit thicker film than sputtering and pulsed laser deposition methods [16].

A.3. Liquid-precursor based techniques

Wet-chemical solutions are used to produce thin films for coatings or microelectronics. The solution is applied on the substrate by spraying, painting, spinning or dipping. Some of these methods require subsequent baking to evaporate the solvent. In this paragraph, only the spray deposition and the sol-gel methods will be explained. Wet deposition techniques require less infrastructure than vacuum based ones and are therefore less expansive.

A.3.1. Spray deposition

In all this kind of methods, a wet chemical solution of the desired product is atomized to generate a fine aerosol and then sprayed onto a substrate. As in CVD, the droplets evaporate or decompose onto the surface of the heated substrate, usually laying on a hot plate [16-18]. This method was formerly used to produce small particles of ceramic powders.

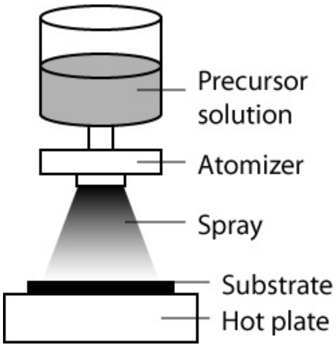

Figure 3: Schematic view of a generic spray deposition system

Several improvements have been realized and allow obtaining better films properties. By applying an electrical potential to the surface of the conducting solution it is possible to control the size distribution of droplets. Electrostatic spray deposition (ESB) produces very porous and regular structure and is widely use for SOFCs [19].

The sprayed solution can be burnt into a flame or in a plasma [20] to sinter particles before they reach the substrate. The flame spray deposition method to produce electrolytes or cathodes [21].

Pressurized gas is also used to atomize the precursor solution. This method permits to deposit PEN component such as YSZ and CGO electrolytes [22].

A.3.2. Sol-gel techniques

Sol-gel precursor solution is spun onto the substrate and then heated on a hot plate to evaporate the solvent. The thickness of the film is proportional to the number of deposition steps and can reach up to 10 μm. After some steps, the film is annealed in a furnace to crystallize the desired phase. In some ceramic layers, gradients of concentration appear in the thickness of the film this problem is solved by using solutions with different concentrations. Sol-gel is an easy and cheap method but it should be automatized to improve the production rate. In the field of SOFCs, sol-gel film have been used for all the PEN elements [23, 24].

A.4. Rotation of the stiffness tensors

This paragraph is mainly adapted from the book of Nye [25]. The Hook's law states that the deformation ε_{kl} is proportional to the stress S_{ij}. The proportion factor is a fourth-rank tensor called the stiffness c_{ijkl}.

$$S_{ij} = c_{ijkl}\varepsilon_{kl}$$

The symmetry of the strain and stress tensors permits to write c in a form of a 6 x 6 matrix. In this case, S and ε are 6 components vectors. The relation between the tensor of stiffness c_{ijkl} and the simplified matrix c_{mn} is:

$$c_{ijkl} = c_{mn}$$

With $i,j,k,l = 1,2,3$ and $m,n=1,2,3,4,5,6$

Note that the relation between the compliance s_{ijkl} tensor and its simplified matrix form is more complicated, as it includes 2 and 4 factors for some components [25].

In the case of a cubic symmetry, the c_{ij} matrix has only three different non zero components (c_{11}, c_{12} and c_{44}):

$$\begin{pmatrix} S_1 \\ S_2 \\ S_3 \\ S_4 \\ S_5 \\ S_6 \end{pmatrix} = \begin{pmatrix} c_{11} & c_{12} & c_{12} & 0 & 0 & 0 \\ . & c_{11} & c_{12} & 0 & 0 & 0 \\ . & . & c_{11} & 0 & 0 & 0 \\ . & . & . & c_{44} & 0 & 0 \\ . & . & . & . & c_{44} & 0 \\ . & . & . & . & . & c_{44} \end{pmatrix} \begin{pmatrix} \varepsilon_1 \\ \varepsilon_2 \\ \varepsilon_3 \\ \varepsilon_4 \\ \varepsilon_5 \\ \varepsilon_6 \end{pmatrix}$$

As our YSZ films are (111) textured, we need to rotate the compliance tensor to obtain the value of c in the plane of the film. The new (001) axis will be oriented as the former (111) direction. The full rotation matrix a_{ij} is given below:

$$a_{ij} = \begin{pmatrix} 1/\sqrt{2} & 1/\sqrt{6} & 1/\sqrt{3} \\ -1/\sqrt{2} & 1/\sqrt{6} & 1/\sqrt{3} \\ 0 & -2/\sqrt{6} & 1/\sqrt{3} \end{pmatrix}$$

Every single component of the new tensor *c'_{ijkl}* of stiffness can be calculated by using this relation and by obeying Einstein's notation:

$$c'_{ijkl} = a_{im} a_{jn} a_{ko} a_{lp} c_{mnop}$$

This relation can only be applied to the tensor and not to the simplified matrix. With the real values of the constant in the old referential ($c_{11} = 410\ GPa$, $c_{12} = 110\ GPa$ and $c_{44} = 60\ GPa$), we calculate the c'_{mn} simplified matrix:

$$c'_{mn} = \begin{pmatrix} 320 & 140 & 170 & 42 & 0 & 0 \\ . & 320 & 170 & -42 & 0 & 0 \\ . & . & 290 & 0 & 0 & 0 \\ . & . & . & 120 & 0 & 0 \\ . & . & . & . & 120 & 42 \\ . & . & . & . & . & 90 \end{pmatrix} \times 10^{9}\, Pa$$

By inverting the matrix c'_{mn} we obtain the compliance of the film s'_{mn}:

$$s'_{mn} = \begin{pmatrix} 5.25 & -1.41 & -2.25 & -2.36 & 0 & 0 \\ . & 5.25 & -2.25 & 2.36 & 0 & 0 \\ . & . & 6.08 & 0 & 0 & 0 \\ . & . & . & 1 & 0 & 0 \\ . & . & . & . & 1 & -4.71 \\ . & . & . & . & . & 1.33 \end{pmatrix} \times 10^{-11}\, Pa^{-1}$$

In the plane of the film the compliance coefficients are respectively s'_{11} and s'_{22}. As the grains are (111) textured but randomly oriented in the plane of the substrate, the stiffness of the film is the mean value of s'_{11} and s'_{22}. In this case, these two coefficients are equals and the film in-plane stiffness constant Y_{film} is simply:

$$Y_{film} = 1/s'_{22} = 192 GPa$$

Finally by definition the Poisson's ratio of the film ν_{film} is:

$$\nu_{film} = -\frac{s_{12}}{s_{11}} = 0.28$$

A.5. References

1. Ohring, M., *Materials science of thin films: Deposition and structure*. 2002, San Diego: Academic Press.
2. Dieleman, J., E.v.d. Riet, and J.C.S. Kools, *Japanese Journal of Applied Physics.* 1, 1992. **31**(1964-1971).
3. Prestat, M., J.-F. Koenig, and L.J. Gauckler, *Oxygen reduction at thin dense La0.52Sr0.48Co 0.18Fe0.82O3-d electrodes: Part I: Reaction model and faradaic impedance.* Journal of Electroceramics, 2007. **18**(1-2): p. 87-101.
4. Baumann, F.S., et al., *Impedance spectroscopic study on well-defined (La,Sr)(Co,Fe)*$O_{3-\delta}$ *model electrodes.* Solid State Ionics, 2006. **177**(11-12): p. 1071-1081.
5. Bieberle-Hütter, A. and H.L. Tuller, *Fabrication and structural characterization of interdigitated thinfilm La1-xSrxCoO3(LSCO) electrodes.* Journal of Electroceramics, 2006. **16**(2): p. 151-157.
6. Chen, X., et al., *Thin-film heterostructure solide oxide fuel cells.* Applied Physics Letters, 2004. **84**(14): p. 2700-2702.
7. Bieberle-Hütter, A., et al., *A micro-solid oxide fuel cell system as battery replacement.* Journal of Power Sources, 2008. **177**(123-130).
8. Rupp, J.L.M., A. Infortuna, and L.J. Gauckler, *Microstrain and self-limited grain growth in nanocrystalline ceria ceramics.* Acta Materialia, 2006. **54**: p. 1721-1730.
9. Chen, L., et al., *High temperature electrical conductivity of epitaxial Gd-doped CeO2 thin films.* Solid State Ionics, 2004. **175**: p. 103-106.
10. Chen, X., et al., *Pulsed laser deposition of conducting porous La-Sr-Co-O films.* Thin Solid Films, 1999. **342**(1-2): p. 61-66.
11. Choy, K.L., *Chemical vapour deposition of coatings.* Progress in Materials Science, 2003. **48**: p. 57-170.
12. Will, J., et al., *Fabrication of thin electrolytes for second-generation solide oxide fuel cells.* Solid State Ionics, 2000. **131**: p. 79-96.
13. Bernay, C., et al., *Yttria-doped zirconia thin films deposited by atomic layer deposition ALD: a tructural, morphological and electrical characterisation.* Journal of Physic and Chemistry of Solids, 2003. **64**: p. 1761-1770.
14. Garcia, G., et al., *Pulsed Injection MOCVD of YSZ Thin Films onto Dense and Porous Substrates.* Chemical Vapor Deposition, 2003. **9**(5): p. 279-284.
15. Ogumi, Z., et al., *Novel Method for Preparing Nickel/YSZ Cermet by a Vapor-Phase Process.* Journal of the American Ceramic Society, 1995. **78**(3): p. 593-598.

16. Beckel, D., et al., *Thin films for micro solid oxide fuel cells.* Journal of Power Sources, 2007. **173**: p. 325-345.
17. Shao, Z., C. Kwak, and S.M. Haile, *Anode-supported thin-film fuel cells operated in a single chamber configuration 2T-I-12.* Solid State Ionics, 2004. **175**: p. 39-46.
18. Beckel, D., et al., *Spray pyrolisis of* $La_{0.6}Sr_{0.4}Co_{0.2}Fe_{0.8}O_{3-\delta}$ *thin film cathodes.* Journal of Electroceramics, 2006. **16**: p. 221-228.
19. Chen, C.H., et al., *Electrostatic sol-spray deposition of nanostructured ceramic thin films.* Journal of Aerosol Science, 1999. **30**(7): p. 959-967.
20. Schiller, G., et al., *Development of Solid Oxide Fuel Cells by Applying DC and RF Plasma Deposition Technologies.* Fuel Cells, 2004. **4**(1-2): p. 56-61.
21. Liu, Y. and M. Liu, *Porous Electrodes for Low-Temperature Solid Oxide Fuel Cells Fabricated by a Combustion Spray Process.* Journal of the American Ceramic Society, 2004. **87**(11): p. 2139-2142.
22. Bohac, P. and L.J. Gauckler, *Chemical spray deposition of YSZ and GCO solid electrolyte films.* Solid State Ionics, 1999. **119**: p. 317-321.
23. Metha, K., R. Xu, and A.V. Virkar, *Two-Layer Fuel Cell Electrolyte Structure by Sol-Gel Processing.* Journal of Sol-Gel Science and Technology, 1998. **11**: p. 203-207.
24. Vo, N.X.P., et al., *Fabrication of an anode-supported SOFC with a sol-gel coating method for a mixed-gas fuel cell.* Key Engineering Materials, 2005. **277-279**(1): p. 455-462.
25. Nye, J.F., Physical Properties of Crystals. Oxford Science Publications. 1985, Oxford: Clarendon Press.

Publications, symposia and patent

1. Rey-Mermet, S., R. Lanz, and P. Muralt, AlN thin film resonators operating at 8 GHz used as sensors for organic films. Proceedings - IEEE Ultrasonics symposium 2, 2005(Art. no. 1603079): p. 1253-1257.

2. Martin, F., et al., Shear mode coupling and tilted grain growth of AlN thin films in BAW resonators. Proceedings - IEEE Ultrasonics symposium 1, 2005(Art. no. 1602862): p. 333-336.

3. Rey-Mermet, S., R. Lanz, and P. Muralt, Bulk acoustic wave resonator operating at 8 GHz for gravimetric sensing of organic films. Sensors and Actuators B, 2006. 114: p. 681-686.

4. Rey-Mermet, S., P. Muralt, and J. Baborowski, Metallic supporting grid or thin electrolyte membrane in solid oxide fuel cells. 2006: PCT/EP2006/069688.

5. Martin, F., et al., Shear mode coupling and tilted grain growth of AlN thin films in BAW resonators. IEEE Transactions on Ultrasonics Ferroelectrics and Frequency Control, 2006. 53: p. 1339-1343.

6. Prestat, M., et al., Oxygen reduction at thin dense LSCF electrodes: Part II. Journal of Electroceramics, 2007. 18: p. 111-120.

7. Rey-Mermet, S. and P. Muralt. Materials and design study for micromachined solid oxide fuel cells membranes. in Materials Research Society Symposium Proceedings. 2007. Boston.

8. Rey-Mermet, S. and P. Muralt. Microfabricated solid oxide fuel cells membranes, International Conference on Electroceramics, 2007, in Arusha (Tanzania)

9. Rey-Mermet, S. and P. Muralt. Solid oxide fuel cells membranes supported by nickel grid anode, 16th International Conference on Solid State Ionics, 2007, in Shanghai

10. Bieberle-Hütter, A., et al., A micro-solid oxide fuel cell system as battery replacement. Journal of Power Sources, 2008. 177(123-130).

11. Rey-Mermet, S. and P. Muralt, Solid oxide fuel cell membranes supported by nickel grid anode. Solid State Ionics, 2008.

12. Rey-Mermet, S. and P. Muralt, Study of stress behaviour with temperature in oxygen ions conductors, Materials Research Society Spring Meeting, San Francisco, 2008.

Curriculum vitae

Samuel Rey-Mermet
Born April 20th 1977
Swiss citizen

Education

Oct. 2004-present:	PhD Thesis at the Ceramics Laboratory Swiss Federal Institute of Technology in Lausanne: *Micro-fabricated solid oxide fuel cells* (Project CTI OneBat).
Oct. 1998-March 2003:	Msc in Materials Science at the Swiss Federal Institute of Technology in Lausanne
Sept. 1992-June 1997:	Maturité fédérale scientifique in Collège de l'Abbaye in Saint-Maurice (Switzerland)

Professional experience

Oct. 2004-present:	Research assistant at the Ceramics Laboratory at the Swiss Federal Institute of Technology in Lausanne Responsible for the security at the Ceramics Laboratory Patent: *Metallic supporting grid or thin electrolyte membrane in solid oxide fuel cells.* 2006: PCT/EP2006/069688.
Summer 2002	Industrial internship at the Alcan Casting and Technology Center Alcan in Chippis (Switzerland)
Summer 1997	Industrial internship at the Nestlé Research Center at Epalinges (Switzerland)